EXPERIMENTAL AND NUMERICAL INVESTIGATIONS ON THE FLUID CONTRIBUTION TO THE TENSILE-COMPRESSIVE MECHANICAL BEHAVIOR OF THE BOVINE PERIODONTAL LIGAMENT

PAR

Marzio BERGOMI

ingénieur en microtechnique diplômé EPF
de nationalité suisse et originaire de Coldrerio (TI)

ÉCOLE POLYTECHNIQUE
FÉDÉRALE DE LAUSANNE

Suisse
2008

A Vale, Chris e Juan

Remerciements

Je voudrais tout d'abord remercier mon directeur de thèse Prof. John Botsis pour m'avoir donné l'opportunité d'accomplir ce travail au sein du laboratoire de mécanique appliquée et analyse de fiabilité (LMAF) à l'École Polytechnique Fédérale de Lausanne (EPFL) mais surtout pour sa présence, constante tout au long de ces quatre années.

Je remercie tous les membres du *PDL Group* avec qui on a eu d'innombrables discussions: l'équipe de l'université de Genève: Prof. Urs Belser, Dr. Anselm Wiskott, Mrs. Giovanna Vaglio, M. Serge Bovier et M. Léonard Brazzola; le Dr. Dieter Bosshardt de l'univerité de Berne; le Dr. Tatsuya Shibata, de l'université Tsurumi, à Tokyo; enfin, les Dr. Aïssa Mellal et Dr. Joël Cugnoni, du LMAF, pour leurs grandes compétences et leur immense disponibilité.

Un grand merci à tous les collègues du labo, anciens et actuels et aux mécaniciens de l'atelier: M. Marc Jeanneret, M. Nicolas Favre et M. Stéphane Haldner, toujours très disponibles et riches en conseils précieux pour le développement du dispositif de test.

Mille merci à toutes les personnes que j'ai pu rencontrer lors des nombreuses collaborations, liées ou pas au sujet de cette thèse. J'ai eu la chance d'avoir eu à que faire à des personnes exquises avec lesquelles je garde toujours de très bons contacts.

Je remercie de tout mon cœur toute l'équipe des labos du couloir d'à coté, et spécialement les deux *trop* grands et le musicien *ultime*. Merci, merci, merci.

Merci enfin à l'équipe qui encadre l'accompagement scolaire au centre socioculturel de la Bourdonnette, ainsi qu'à tout(e)s les *petit(e)s monstres* qui ont ravivé, et animeront encore je l'espère, nos débuts de semaine.

Merci encore et toujours
à ma famille,
à mes amis les plus chers.

Abstract

Orthodontic treatments are all based on the experimental evidence that teeth can be forced to move in the dental arch by means of applied mechanical forces. Since it allows for prediction of dental mobility, the mechanical characterization of the tissues involved in this process is of paramount importance. In fact, as technologies and strategies in treating pathological situations become increasingly more advanced, better knowledge of dental mobility allows for the optimization of these tools and thus, minimization of the costs of the interventions.

Among the tissues that made up the *periodontium*, the functional unit comprising the bone of the jaw, the periodontal ligament (PDL, a soft connective tissue which binds the teeth to the jaw) and the cementum of the teeth, the PDL is commonly considered to play the major role in dental movements. To obtain insights on its mechanical behavior, specimens of PDL, containing also bone and cementum parts, are extracted and tested with adequate loading profiles. However, due to morphology and size, the excision of such specimens is often delicate and represents one of the main challenge in the experimental characterization of the PDL. Furthermore, for the investigation to be pertinent, it is necessary to test the *in-vitro* specimens in an environment recreating at best physiological conditions.

In this study, the characterization of the mechanical behavior of the periodontium was based on *histo-morphological investigation*, on *mechanical testing* of excised specimens containing the three tissues and on *numerical modeling*.

Micro-structural aspects of the periodontium were assessed by morphometric analysis of histological sections. Since it plays a central role in the tooth supporting mechanism, the vascular system was characterized by assessing densities and sizes of blood vessels present in the PDL. Also, the roughness of the interfaces between PDL and bone and between PDL and cementum was quantified via their fractal dimensions.

To approach as much as possible an *in-vivo*–like situation for the mechanical testing of *in-vitro* specimens, physiological conditions were reconstructed at best in a closed environment created in a custom-made *pressure chamber* filled with physiological solution. Cylindrical specimens, with diameter of approximatively 6mm, were obtained from mandibular first molars of freshly slaughtered bovines. A thorough experimental determination of the contribution of the fluid phase, comprised in the periodontium, to the overall response of the tissues was carried out by imposing sinusoidal tensile-compressive loading profiles (simulating mastication) to specimens subjected to different environmental conditions.

A numerical model was then developed to reproduce and analyze the observed phenomena.

Eventually, the mechanical response to multiaxial loading was investigated by simultaneously applying axial displacement and lateral hydrostatic confinement to specimens which were wrapped in a thin rubbery membrane.

The morphometrical investigation enhanced the high *heterogeneity* and *porosity* of the tissues involved. In fact, no general pattern could be established for the structural description of the periodontium. Moreover, the presence of large blood vessels in the PDL suggested that

the vascular system should somehow be taken into consideration when describing the mechanical behavior of this ligament.

The mechanical testing proved the response of the bone-PDL-cementum functional system to be characterized by the interactions between a *porous solid skeleton*, forming the structural matrix of the tissues, and a *fluid content* flowing through it during cyclic tensile-compressive loading profiles. In fact, the solid matrix *alone* (i.e., emptied of its fluid content) clearly showed an *hyperelastic* behavior (both for tensile and compressive loading), so that the highly *time-dependent hysteric* behavior shown during compressive loadings of fully fluid-saturated specimens was mainly attributed to the fluid phase.

The numerical model, based on a *multiphase mixture* formulation, allowing thus for the description of the interactions between a porous compressible hyperelastic matrix (described by an Ogden's strain energy potential) and the fluid filling its pores, well reproduced the mechanical response of the periodontium subjected to cyclic tensile-compressive loadings. The model enhanced also the significant *exchange of fluid* taking place between the PDL and the bone part of the specimens, proving thus the importance of considering the fluid phase in the mechanical description of the periodontium. Loading rate dependences of the compressive response were also partially captured by such a model.

The experimental response to a multiaxial loading showed eventually the dependence of the axial stress on the joined action of level of lateral confinement (hydrostatic pressure) *and* extent of fluid saturation of the solid matrix.

Resumé

Les traitements orthodontiques se basent tous sur l'évidence expérimentale que les dents peuvent être déplacées dans la cavité orale grâce à l'application de forces mécaniques. La caractérisation du comportement mécanique des tissus impliqués est donc fondamentale, puisqu'elle permet de prédire ce phénomène qu'est la mobilité dentaire. En effet, l'avancement de l'état des techniques et des stratégies proposées pour le traitement de situations pathologiques requiert une profonde connaissance des phénomènes qui règlent cette mobilité. De plus, ce savoir permettrait une minimisation des coûts d'intervention.

Parmi les tissus constituant le *périodonte*, l'unité fonctionnelle comprenant l'os de la mâchoire, le ligament parodontal (PDL ou desmodonte, tissu mou reliant les dents à la mâchoire) et le cément de la dent, le PDL est considéré jouer un rôle décisif en biomécanique dentaire. L'analyse de son comportement mécanique passe souvent par l'extraction d'échantillons, comprenant aussi des parties d'os et de cément, qui sont par la suite testés avec des profils de charges adéquats. Cependant, compte-tenu de sa morphologie et de sa taille, l'extraction de tels spécimens est souvent délicate et représente un des défis majeurs dans la caractérisation expérimentale du PDL. De plus, pour une étude rigoureuse, il est nécessaire de tester ces échantillons *in-vitro* dans un

environnement recréant au mieux des conditions physiologiques.

Dans cette étude, la caractérisation du comportement mécanique du périodonte a été basée sur des *analyses histo-morphologiques*, sur des *tests mécaniques* effectués sur des échantillons contenant les trois tissus et sur des *modèles numériques*.

Les aspects micro-structuraux du périodonte ont été évalués par analyse morphométrique de sections histologiques. Étant donné qu'il joue un rôle central dans le mécanisme de support dentaire, le système vasculaire a été caractérisé par l'évaluation des densités et des dimensions des vaisseaux sanguins présents dans le PDL. De même, la rugosité des interfaces entre PDL et os et entre PDL et cément a été quantifiée par leur dimension fractale.

Pour approcher les conditions *in-vivo* lors d'essais mécaniques d'échantillons *in-vitro*, l'état physiologique a été reconstitué au mieux dans un environnement clos, créé à l'aide d'une *chambre à pression*, spécialement conçue pour les besoins de l'étude, et remplie avec une solution physiologique. Des échantillons cylindriques de diamètre approximatif de 6mm ont étés extraits des premières molaires mandibulaires de bovins fraîchement abattus. Une détermination expérimentale minutieuse de la contribution de la phase liquide, contenue dans le périodonte, à la réponse totale des tissus a été effectuée en imposant des profils de charges sinusoïdaux en traction-compression (simulant la mastication) à des échantillons soumis à différentes conditions environnementales. Un modèle numérique a été ensuite développé pour reproduire et analyser les phénomènes observés. Finalement, la réponse mécanique à un chargement multiaxial a été étudiée en appliquant simultanément un déplacement axial et un confinement hydrostatique latéral à des échantillons enrobés dans une fine membrane.

Les analyses morphométriques ont mis en évidence le caractère *hétérogène* et *poreux* des tissus étudiés. En effet, aucune généralité a pu être établie pour la description de la structure du périodonte. De plus, la présence de gros vaisseaux sanguins dans le PDL suggère que le

système vasculaire doit impérativement être pris en considération pour une interprétation correcte du comportement mécanique de ce ligament.

Les essais mécaniques ont démontré que la réponse du système os-PDL-cément était caractérisée par une forte interaction entre un *squelette solide et poreux*, formant la matrice structurelle des tissus, et une *phase liquide* s'écoulant à travers cette matrice pendant les chargements cycliques en traction-compression. En effet, la matrice solide *seule* (testée donc en absence de phase liquide) à montré un comportement *hyperélastique* (pour des chargements soit en traction soit en compression) de sorte que le comportement *histéretique* observé lors de chargements compressifs d'échantillons complètement saturés a pu être principalement attribué à la phase liquide.

Le modèle numérique, basé sur une formulation de type *mélange multiphasique* permettant la description des interactions entre une matrice hyperélastique, poreuse et compressible (décrite par un potentiel d'énergie de déformation du type Ogden) et le liquide circulant entre ses pores, était bien adapté pour reproduire la réponse mécanique du périodonte soumis à un chargement cyclique. Le modèle a, entre autres, mis en évidence un *échange significatif de liquide* ayant lieu entre le PDL et la partie osseuse des échantillons, prouvant ainsi à quel niveau il était important de considérer la phase liquide lors de la description du comportement mécanique du périodonte. De même, la dépendance de la réponse en compression au taux de chargement a pu être partiellement expliquée par un tel modèle.

Pour conclure, la réponse à un chargement multiaxial a révélé comment l'action conjointe du niveau de confinement latéral (pression hydrostatique) *et* de l'étendue de la saturation en liquide de la matrice solide affectent l'état de contrainte axiale.

Mots clés: Ligament parodontal (desmodonte), milieu poreux, tension-compression, contribution du fluide, modèle à éléments finis, chargemet multiaxial.

Contents

List of Tables

List of Figures

List of Symbols

Roman

a_0	parameter for viscosity
$\mathbf{a}_{f,s}$	fluid or solid acceleration
A	area
b	breadth
$\mathbf{B}$	body force density per reference unit volume
$\mathcal{B}$	material body
$\mathbf{c}$	left Green-Cauchy deformation tensor
C_{K-C}	Kozeny-Carman constant
$\mathbf{C}$	right Green-Cauchy deformation tensor
d	diameter
$d(t)$	displacement
D	fractal dimension
$\bar{e}$	void ratio
E	Young's modulus

$E_{c,t}$	compressive or tensile energy loss
$\mathbf{E}$	Green-Lagrange deformation tensor
$F(\cdot)$	load, function of $\cdot$
$\mathbf{F}$	deformation gradient tensor
$\mathbf{F^b}$	body forces
$\mathbf{F^c}$	contact forces
$\mathbf{g}$	gravity vector
h	height
$H_{c,t}$	compressive or tensile hysteresis
i	number of cycles
$I_i(\cdot)$	principal invariants of $\cdot$
J	Jacobian
k	absolute permeability
k_0	parameter for viscosity, initial permeability
k_s	hydraulic conductivity
$\mathbf{k}$	permeability tensor
K	constant for a line's morphology
$K_{f,s}$	fluid or solid bulk modulus
l	length
L	real length of a line
$L(\epsilon)$	measured length of a line
M	material constant
n	porosity
n_0	parameter for viscosity
N	order of the strain energy potential

N	normal vector to the surface dA
p	hydrostatic pressure
P	actual mass density in material desctiption
P_0	initial mass density
P	first Piola-Kirchhoff stress tensor
q	fluid flux
q	eulerian fluid flow
Q	fluid discharge
s_i	i^{th} set of parameters
S_0	specific area per unit volume of matrix particles
S	second Piola-Kirchhoff stress tensor
t	time, thickness
$T(\cdot)$	nominal stress
T	stress vector
u	spatial displacement vector
U	internal energy density
v	volume in spatial description
V	volume in material description
V, V_f, V_s	total volume, fluid volume, solid volume
V	material velocity
w_0	PDL's width
$\mathcal{W}, \widehat{\mathcal{W}}, W$	strain energy potentials
x	spatial position vector
X	material position vector

Greek

$\alpha,\ \alpha_i$	material parameters
$\alpha_{tl,tu,cl}$	Fung's degrees of non-linearity
β_i	material parameters
γ_w	specific weight of wetting fluid
$\delta_{c,t}$	compressive or tensile phase lag
ϵ	strain or measuring gauge length
η	viscosity
λ	stretch ratio
λ_i	principal stretch ratios
$\mu,\ \mu_0$	initial shear modulus
μ_i	material parameters
$\nu,\ \nu_i$	Poisson's ratios
Π_0	part of the body $\mathcal{B}$
ρ	total density
$\rho^{f,s}$	solid or fluid partial density
$\rho_{f,s}$	solid or fluid true density
ρ	actual mass density
$\boldsymbol{\sigma}$	Cauchy stress tensor, total stress
$\boldsymbol{\sigma}'$	effective stress
$\boldsymbol{\sigma}^{f,s}$	fluid or solid partial stress
$\phi^{f,s}$	fluid or solid volume fraction
χ	motion (or deformation) function
$\Omega,\ \Omega_0$	three dimensional domain
$\partial\Omega$	boundary of Ω
∇	material gradient operator
$D(\cdot)/Dt$	material time derivative

List of Abbreviations

B	Alveolar Bone
BV	Blood Vessels
C	Cementum
CFs	Collagen Fibers
D	Dentin
ECM	Extra Cellular Matrix
FE	Finite Element
fb	Fibroblast
normal profile	Loading profile for mechanical tests (page 83)
PDL	Periodontal Ligament
QLV	Quasi-Linear Viscoelasticity
r.a.	Remodeling Activity
r.c.	Resorption Cavities
ROI	Region Of Interest
sh	Sharpey's Fibers
SLC	Submersible Load Cell

Chapter 1

Introduction and Motivations

If one way be better than another, that you may be sure is Natures way.

Aristotle, 384 BC - 322 BC

1.1   Biomechanics

Bio-mechaincs is the branch of physics concerned with motion and equilibrium (*-mechaincs*) applied to living systems (*Bio-*). A comprehensive definition for this discipline has been formulated by Fung in its fundamental book *Biomechanics* [50]:

≪*Biomechanics seeks to understand the mechanics of living systems. It is a modern subject with ancient roots and cover a very wide territory [...]. The motivation for research in this area comes from the realization that biology can no more be understood without biomechanics [...]. For an organism, biomechanics helps us to understand its normal function, predicts changes due to alterations, and propose methods of artificial intervention. Thus diagnosis, surgery and prosthesis are closely associated to biomechanics.*≫

As mentioned by Fung, the interest in understanding how living systems work is ancient and can be led back to the greek Aristotle (384-322 B.C.) and his works *On the Parts of Animals* and *On the Movement of Animals*, in which he described animal bodies as mechanical systems.

1
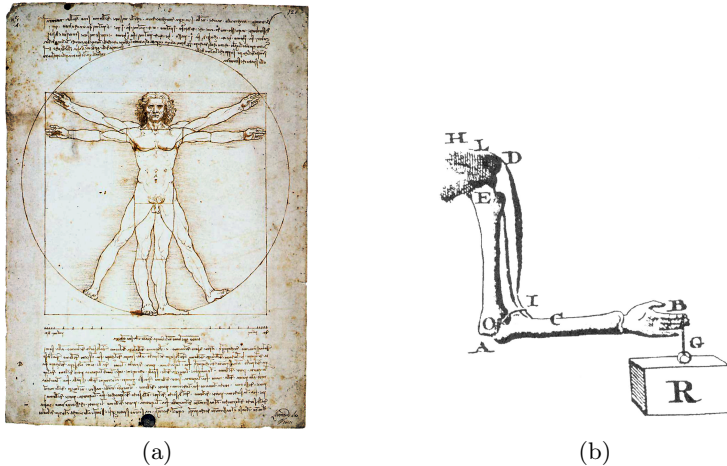
Figure 1.1: Biomechanics: (a) Leonardo da Vinci's Vitruvian man exemplify the blend of art and science by illustrating the proportion of the human body; (b) Giovanni Borelli's study of arm's mechanics.

Later on, other great scientists established the basics for this field; Leonardo da Vinci (1452-1519) studied muscle forces and joints functions basing himself on observation (the great painter is considered as one of the father of anatomy, figure 1.1a) and experimentation, in particular trying to mimic, by **designing** artificial mechanisms, the nature's way of doing things; Galileo Galilei (1564-1642), who, by **analyzing** the results obtained from his original experimental methodology, has been the first to guess that bones are hollow; Giovanni A. Borelli (1608-1679), generally considered as the first modern biomechanician, who tried to explain animals' body motion through mechanical principles (figure 1.1b); and Hermann von Helmholtz (1821-1894) who was the first bioengineer inventing several instruments to study the mechanical behavior of human organs. Clearly, then, as stated by Humphrey and Dalenge [62], «biomechanics focuses on both **design** and **analysis**, each of which is fundamental to engineering».

1.2 Dental biomechanics

If one gently tries to wiggle one of its teeth, for instance the upper left incisor, one perhaps feels it slightly moving. Question may arise whether this is a *physiological* or a *pathological* situation.

This movement is a normal condition and is caused by the presence of a soft, tiny membrane, called *periodontal ligament* (PDL), interposed between the roots of each tooth and the bone of the jaw. Contrarily perhaps to what people commonly think, the teeth are not just rigidly connected to the jaw, but held to their sockets by this ligament, thus allowed to move. But then, what is it there for? How does it contribute to the mechanics of the masticatory system?

Dental biomechanics try to answer to this kind of questions. It is one of the several disciplines up which the large field of biomechanics naturally split during its development. Its main objective is to supply tools helping dentists and maxillofacial surgeons in planing their interventions more rationally, increasing thus the chances of success. ≪*Understanding tooth displacement under functional loads is becoming more important, as new solutions in dental restorations, prosthodontics and orthodontic treatments become increasingly more advanced*≫ [123].

Dental mobility is then the keyword; prediction of the displacements knowing the applied forces and vice versa. This comes to describe the laws ruling the mechanical behavior of the materials involved. A metallic dental implant, for instance, can generate some residual stresses once screwed into the jaw bone. But how far these residual stresses are sensed? And since it is known that prolonged loading profiles may induce bone remodeling (i.e. bone growth or resorption, depending whether the stress is higher or lower compared to a physiological situation), how the surrounding tissues will be affected?

Constitutive laws describing at best the real mechanical behavior, together with accurate numerical simulations, will help to answer these questions.

1.3 The periodontium

≪*Periodontium literally means "around the tooth"… and designates the physiological unit comprising the gingiva, the periodontal membrane and the alveolar process, viewing these as a functional system which receives the impact of mechanical function of the teeth… it is used to designate the functional structures that are directly involved in resisting forces applied to the teeth.*≫ S.P. Ramfjord, [119].

The *periodontium* (see figure 1.2) is thus a sort of articulation composed by two antagonist bony parts, the **cementum** on the tooth side and the **alveolar bone** on the jaw side, and by a layer in between these two hard tissues, the **periodontal ligament** (**PDL**), making the connections and allowing for relative displacements of the tooth with respect to the bone. The **gingiva**, the soft tissue which overlies the bone and forms a protective collar around the tooth, is also considered part of the periodontium.

The periodontium, however, is not a *common* articulation like the knee, the hip or the shoulder; in these articulations, called **diarthroses**, the range of movement is large, cartilage covers the extremity of the bones and a ligamentous capsule envelops the whole joint. In these kind of joints cartilage is the tissue responsible for shock cushioning and friction minimization.

The PDL is neither a **synarthrosis**, or immovable articulation. This kind of articulation do not have any articular cavity and provide no movement. Their principal function is to provide stability, and to absorb energy in case of trauma. An example of a synarthrosis is the cranium.

Amphiarthroses are those kind of articulation with no articular cavity, connecting bone to bone by ligamentous or cartilagenous tissue and allowing for limited motion. The anchoring of teeth to the mandible by the PDL, called a gomphosis, or the intervertebral disks are examples of this kind of articulation.

Figure 1.3 presents an histological cross-section of the periodon-
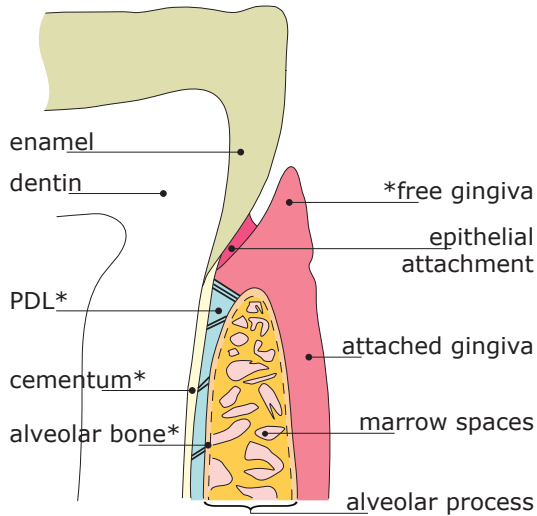
Figure 1.2: Schematic drawing of the tooth anatomy (vertical cross section) and terminology for the different tissues. The cementum, the PDL, the alveolar bone and the gingiva (marked with *) made up the periodontium unit.

tium structure, where alveolar bone (b), periodontal ligament (PDL), cementum (c) and dentin (d), with their respective features, are clearly distinguishable.

In the following sections (1.3.1 and 1.3.2) a summary of relevant informations, from an anatomical and/or morphological point of view, for this study on the periodontium is reported. Keeping in mind that this investigation was dealing with a functional system, a description of all of the tissues involved in the mechanical response (i.e., alveolar bone, PDL and cementum), is given.

1.3.1 Periodontal ligament

The **periodontal** (*perio*, from the latin *to surround*, and *dontal*, meaning *tooth*) **ligament** (from *ligare*, meaning *to attach*) is the soft tissue
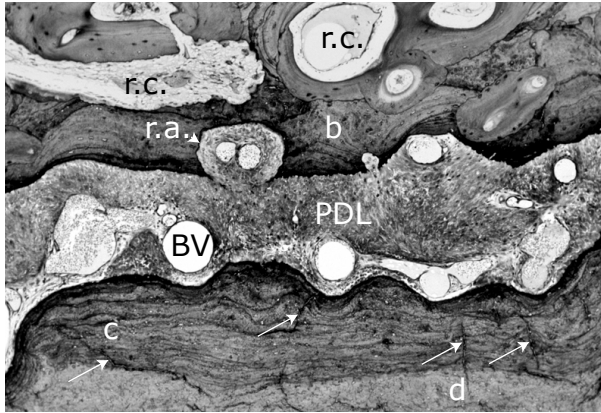
Figure 1.3: Histological section of the periodontium: the alveolar bone (b), on the top of the figure, shows some remodeling activity (r.a.) and resorption cavities (r.c.); the periodontal ligament (PDL) is the mid-layer in the figure. It presents a dense, spaghetti-like collagen fiber mesh with fibroblast cells (darker dots within the PDL) and an important vascular system (BV); the cementum (c) and dentin (d) are the bottom layers. Cementum shows a lamellated (horizontal in the picture) structure, perpendicularly crossed by tubules (arrows) which enters into the dentin.

which wraps the roots of the teeth and holds them to the surrounding bone.

In general terms, a *ligament* is a short band of tough, flexible, fibrous tissue which connects bone to bone (in opposition to tendons, connecting bone to muscle) to form an articulation. Its principal role is to ensure passive stability of the articulation. More specifically, the periodontal ligament (PDL) bonds two different hard tissues; the cementum of the teeth and the bone of the jaw. In this, and many other aspects, the PDL results, as pointed out by Beertsen *et al.* [8] to be ≪a *unique, multifunctional connective tissue*≫. Among its functionalities, in fact, Beertsen *et al.* enumerated the following:

1. *bonding* of the teeth to the surrounding alveolar bone;

2. *cushioning* and *distributing* the shocks due to physiological or

pathological loadings to the contiguous alveolar bone;

3. allowing for *dental mobility*. The direction, frequency, duration and magnitude of the applied forces determine in part the extent and rapidity of bone remodeling.

4. providing for *sensory input* the masticatory system;

5. *nourishing* of the surrounding tissues though the vascular system.

From a mechanical standpoint, points 1 to 3 are the most relevant. Teeth mobility, in particular, is a peculiar functionality of the PDL that others common ligaments do not show. It is exploited in the field of orthodontics to adjust a possible pathological spatial distribution of the teeth within the oral cavity. In fact, it has been verified [58] that, when forces are applied to teeth or osteointegrated implants with no surrounding PDL, the rate and extent of bone remodeling is very limited.

Thus, the presence of the PDL, together with the application of some external forces, allows for teeth to move within their bony support. The connections between these elements still nowadays not well understood. Nevertheless, the biological structure of the PDL (rich in cells responsible for tissue generation, see below) can give some insights on the mechanisms underlying teeth mobility.

The following is the description of the principal components which made up ligaments in general (see [32, 50] for a more comprehensive description of ligament composition) and PDL in particular:

- **Ground substance**

  The *ground substance*, or *extracellular matrix* (ECM) is all the material building up a tissue, except for the cells. In connective tissues such as tendons, ligaments, cartilage, or bones, the majority of the tissue consists in ECM. It is made of a network of *interfibrillar matrix* material (**collagen** or **elastin**, see below) containing *proteoglycans* and other proteins. Proteoglycans are

proteins connected with and surrounding the interfibrillar matrix. In general, bone, tendon and ligament tissues present a minor quantity of proteoglycans than cartilage, where they dominate the mechanical behavior. In fact, the function of this protein is to regulate the amount of water in the tissue (lubrication).

The ECM is manufactured by specialized **cells** (see further) that generate the different types of connective tissue. In the case of ligaments, *fibroblasts* are the cells responsible for collagen and elastin synthesis.

- **Collagen fibers**.
  Collagen fibers (CFs) are the main component of the ECM (see figure 1.4). They are fibrous proteins which are synthesized within cells but do not contribute to cellular functioning, since they only perform a *structural* role in the ECM.

  There are 5 distinguishable types of fibrous collagen; I, II, III, V and XI (type I is the main type present in tendons and ligaments). They represent a third of the total body proteins and occur in almost all tissues. Tendons contains the highest percentage (75 to 85%), while *only* 50 to 70% of the PDL is made of CFs [33,89].

  Collagen are organized into structured patterns; single *collagen molecules* (size of 1nm) are grouped to form *collagen fibrils* (100 nm), which are the unit constituting the CFs. A bundle of CFs made up a *fascicle*.

  CFs provide strength and confer form, while allow for flexibility and movement; they are the major structural component of tissues, carrying tension in soft tissues and providing a platform for mineralization for hard tissues, mostly subjected to compression.

- **Elastin fibers**
  Elastin is a non-collagenous fibrous protein also secreted into the ECM. With some exception (e.g., ligamentum nuchae and ligamenta flava), elastin is present in very small amounts in tendons
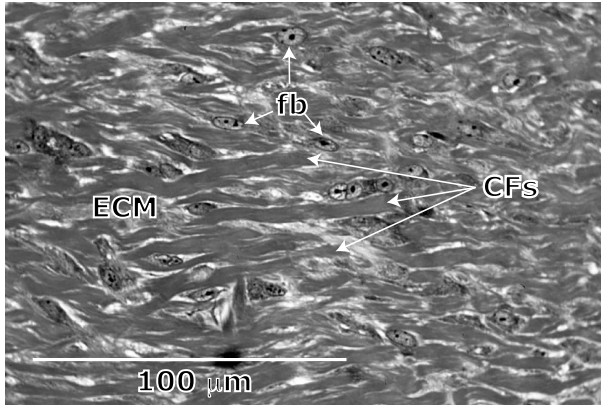
Figure 1.4: Histological section of the PDL: the collagen fibers (CFs) compose the vast majority the extracellular matrix (ECM). Fibroblast (fb) can be seen within the fiber bundles (from Sanctuary, [123]).

and ligaments. It allows tissues to elastically deform without damage. No studies to date report the existence of elastin in humans, rats, monkeys or mice PDL [134].

- **Vascular system**
  Compared to other fibrous connective tissues, the PDL *vasculature* (i.e., the *blood vessels* (BV)) results to be highly developed [48] (see also figure 1.3). It has been suggested [85, 94, 106, 113], therefore, that the vascular system of the PDL plays an important role in shock absorption during mastication impacts. BV volume is evaluated to occupy from 4 to 47% [17, 132] of the PDL space.

  The PDL receives its blood supply from three sources [42, 51]: (i) *cervically* (from the top) from vessels of the gingiva, (ii) *laterally* from vessels passing through the alveolar bone (known as perforating arteries), and (iii) *apically* (from the bottom) from branches of the vessels supplying the pulp of the tooth.

- **Nerve fibers**
  Nerves generally wrap groups of CFs (fascicles, see above). It has been established [158] that the sensory system within the PDL plays a role in monitoring bite force discrimination.

- **Cells**
  The cells contained in the PDL are responsible for the ECM genesis; *fibroblasts* (fb, see figure 1.4), embedded in the ECM and parallel oriented with respect to the surrounding CFs, synthesize CFs and elastin. They are interconnected by numerous junctions, thus able to coordinate their action. Peculiar to the PDL *fibroblasts* is the presence of an enzyme responsible for mineralization processes [8]. It is not clear, however, why the entire periodontal ligament does not mineralize during normal functioning.

  Cells responsible for cementum and bone deposition were also found within the PDL [11, 28]. *Cementoblasts* and *osteoblasts* cells are located close to the surface of the cementum and of the alveolar bone, respectively.

The PDL appears to be more complex than other ligaments; its shape, size and morphology represent major challenges for an accurate description. In fact, ligaments generally have a well defined geometry with an easily identifiable direction of the fibrous (i.e., collagen and elastin) structure. Physiological stimuli are generally only tensile loadings along the tissue's fibers orientation. In the case of the PDL, collagen fibers have a much more wavy pattern, and no well defined preferential direction can be identified.

In sum, as Edwall *et al.* clearly stated in [44], ≪*The PDL undoubtely has unique functions among the connective tissue in the mammalian body. Its ability to tolerate high intermittent pressures during mastication, as well as more continuous pressures — for instance during orthodontic treatment — combined with its ability to detect small tactile stimuli is impressive. The vasculature in the PDL is adapted*

to these conditions, and it plays a central role in the functions of the ligament.≫

1.3.2 Cementum and alveolar bone

Both of these tissues are hard mineralized tissues. They represent the boundaries within which the PDL is confined.

Cementum is the calcified tissue that completely covers the roots of the teeth, which are made of dentin. Its structure presents a lamellated pattern (parallel to the interface with the PDL, see figure 1.3) and provides for the attachment of the PDL collagen fibers (see figure 1.5a). In humans, cementum is found to be of about 50μm thin close to the cemento-enamel junction (refer to figure 1.2), whereas at the apex (i.e., the tip of the roots) it may reach 300μm in thickness [119]. Generally, its interface with the PDL appears smooth, if compared with the bone surface.

Cementum deposition on dentin surface is initiated by the presence of cells called *cementoblasts*, which are responsible for cementum growth via the synthesis and the mineralization of the organic matrix. Calcified collagen fibers are embedded in the cementum layers quite perpendicularly to its surface and forms the so called *Sharpey's fibers* (see figure 1.5a).

Narrow channels, called *dentinal tubules* (see figure 1.3), cross cementum and dentin layers and connect the pulp of the teeth to the PDL and to the oral cavity. Teeth hypersensitivity to cold and/or hot foodstuff has been proved to be related to these tubules [100, 169]. Cementum is a relatively compact tissue, since no vascularization can generally be found in it, and its only porosity is due to the dentinal tubules. Values for porosity are rarely found in the literature; Qin *et al.* [115] proposed a 5% porosity.

The functionality of the cementum is to transmit occlusal forces to the periodontal ligament and to resist pressure against the root surface.
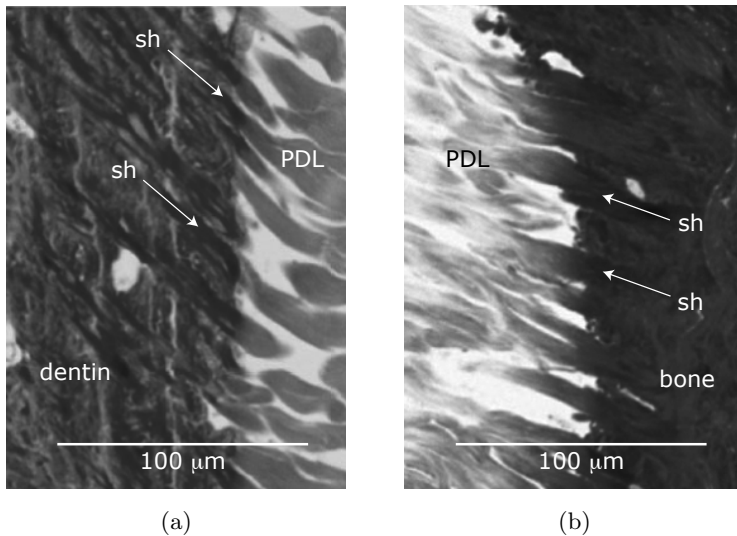
Figure 1.5: Macerated thin sections showing calcified *Sharpey's fibers* (sh) inserting into cementum (a) and bone (b) (from Sanctuary, [123]).

Alveolar bone (see figure 1.2) is the bone which forms the sockets accommodating the teeth. Like any other bone in the human body, alveolar bone grows and declines throughout life. It is rich in *osteoblasts*, the cells responsible for bone formation, which create bone, and in *osteoclasts*, the cells responsible of bone resorbtion, which destroy it, especially if some mechanical stress is exercised on the bone [122]. In fact, a portion of bone under compressive force shows a high level of osteoclasts concentration, resulting in bone resorption. Contrarily, an area of bone under tensile stresses presents a high number of osteoblasts, resulting in bone formation.

The alveolar bone is a plate of compact bone, the thickness of which depends on the positioning of the teeth, as well as on functional needs; the plate becomes thicker with increasing and thinner with decreasing functional loadings [52]. The ability of bone to modify its structure to specific loadings is known as *Wolff's law* [162].

Numerous holes (the *Harvesian canals*, [119]), allowing for the nerves and the blood vessels to reach the PDL from the marrow spaces (see figure 1.2), perforate the alveolar bone plate [51]. These holes, together with the *resorbtion cavities*, resulting from bone remodeling processes (see figure 1.3), are the evidence of the porous nature of this tissue. As in the case of cementum, values for this specific material property are difficult to find. Nevertheless, quantities assessed for cortical bone from femur [9, 153], mandible [149] and other compact bones [31], ranging between 8 and 12%, and can be taken as representative of alveolar bone porosity, since these tissues are considered to be of the same nature.

Alveolar bone is principally made of collagen, mainly structured in calcified *Sharpey's fibers* (see figure 1.5b), which are continuous with the PDL collagen fibers and represent the anchoring apparatus of the PDL to the bone. *Sharpey's fibers* can extend over a great distance in the alveolar bone, exceeding sometimes the width of the ligament itself [8]. For mechanical *in vitro* testing of the periodontium, it is thus important that the excised specimen presents enough bone to ensure that the ligament still posses its integral anchoring system.

At the macroscopic scale, the bone surface often appears quite rough and jagged (see figure 1.3), testifying a certain proficiency in the remodeling activity.

From a functional point of view, alveolar bone supports the teeth and bears the stresses arising form the forces applied to them.

1.4 Review of experimental techniques

Interest in mechanical testing on dentition began in the 17$^{\text{th}}$ century, when Fauchard [155] first published a description and an illustration of an orthodontic apparatus, generating forces by the use of ligatures binding the teeth to a rigid arch, and aiming to move teeth within the bone of the jaw. Since then, more and more refined experimental setups, with the help of histo-morphological investigations, tried to shed light on why, by applying forces to them, teeth can move into their bony

sockets.

The types of tests found in the literature can be catalogued into two main groups: the **Whole tooth** (see section 1.4.2) movement characterization (see figure 1.6a), roughly representing one third of published experimental papers, and the direct **Periodontal specimen** (section 1.4.3) characterization (figure 1.6b), representing the remaining two thirds.

1.4.1   Typical mechanical response of soft tissues

Before focusing on the PDL, a description of the mechanical response of soft tissues in general is worthwhile. Figure 1.7 shows the typical response to a tensile test of soft tissues (e.g., ligaments, tendons, arteries, skin). Initially the tissue shows very little resistance to elongation, resulting in a very flat response called *zero* region. A non-linear increase of the load with further increasing displacement, called *toe* region, appears afterwards. Follow *linear* and subsequent *rupture* regions.

The shapes of the various stages of this curve can be qualitatively interpreted by the histological analysis of the tissue's structure. During the *zero* region the collagen fibers of the tissue are coiled and do not carry any load. The extracellular matrix surrounding the fibers undergo shearing during this stage [37]. Further elongation provokes progressive uncoiling and engagement of the collagen fibers in load bearing, resulting in the non-linear *toe* region. In the *linear* part, all of the fibers are in a stretched state and well aligned along the loading direction. With further elongation, progressive rupture of the fibers occurs, until complete fracture of the tissue.

The displacements (or strains) during these processes are generally large with respect to the thickness of the ligament.

1.4.2   Whole tooth

For this kind of test, a whole tooth surrounded with intact jaw bone, either *in-vivo* or *ex-vivo* (i.e., an intact excised block containing the en-

Whole tooth

(a)

PDL specimens

shear specimen   uniaxial specimen

(b)
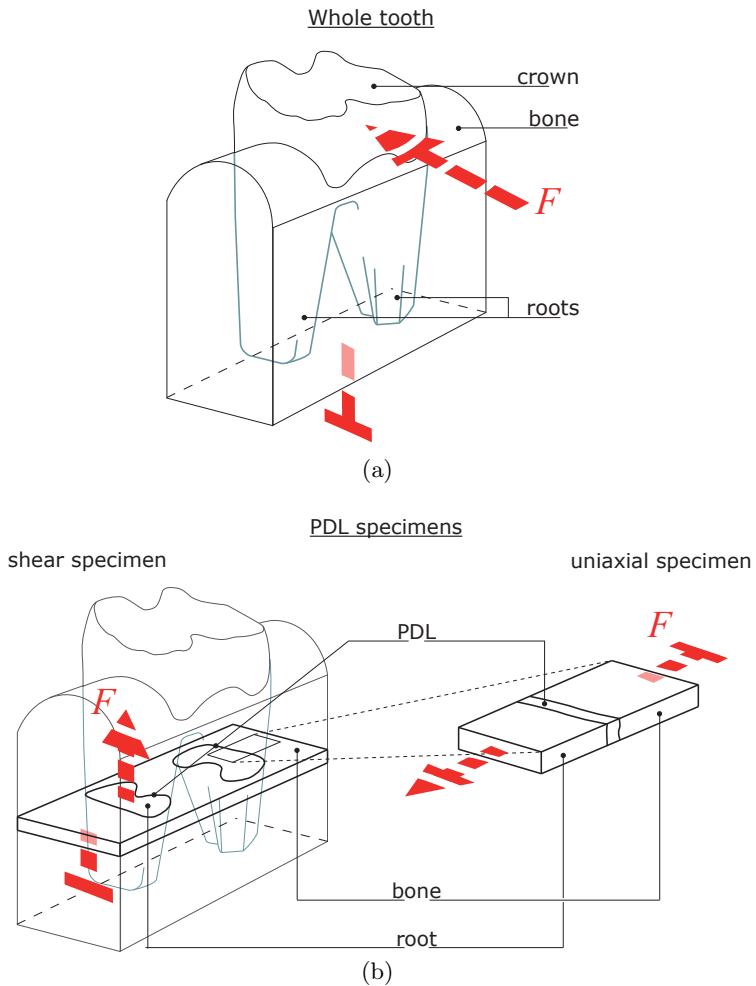
Figure 1.6: Schematic illustrating a whole tooth test (a), a shear test on a *shear specimen* (left) and a uniaxial test on a *uniaxial specimen* (right) (b). A load F is applied to the tooth part of the specimen, while the bone part is held fix. The resulting displacement is recorded via an appropriate transducer.
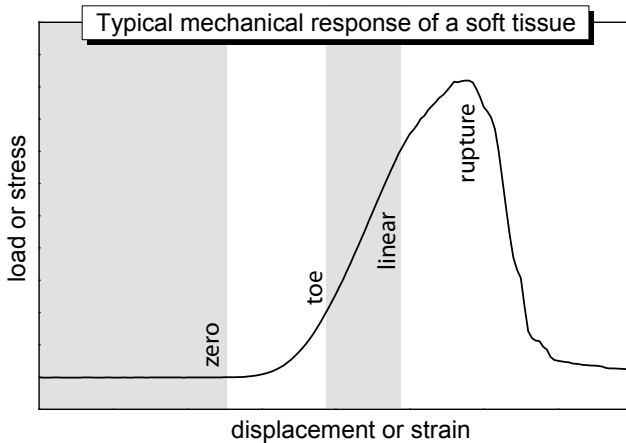
Figure 1.7: Typical mechanical response of soft tissues. Four zones are usually clearly distinguishable: the zero, the toe, the linear and the rupture regions.

tire tooth and surrounding bone, as shown in figure 1.6a), is subjected to loading (force or displacement controlled) while the response (displacement or force) is recorded. The main advantages of this technique reside in that the periodontium is kept intact and, that in the case of *in-vivo* testing, all the possible bio-chemical processes (e.g., blood supply, bone remodeling), occurring during tooth loading, are still going on. These tests provide valuable information on the global tooth response to physiological or orthodontic stimuli. The major drawbacks are, however, the very complex three-dimensional geometry of the specimen and the delicate intra-oral experimental testing conditions. The measured response is thus the average behavior of the whole articulation. Recorded data are furthermore of difficult interpretation, due to the often unknown morphology of the tested specimen.

Among the first studies performed on entire teeth, the one by Parfitt [99] recorded the physiological mobility of individual teeth in the axial

direction. Similar loading profiles where also proposed by Picton and Wills [102] on living monkey subjects. The early work by Daly *et al.* [33] is the only experimental study having proposed *in-vivo* torsional loadings on human teeth. Pull-out (tooth extraction) tests are described in the works by Chiba *et al.* [24, 26] in the case of rat incisors. The vast majority of the studies [3,38,67,112,143,148,168], however, proposes the application of a lateral load, often on (human, rat and dog) incisors and directed inwards the mouth. Summarizing, these works enhanced the non-linear elastic, hysteretic, history-dependent and anisotropic (see section 1.5 and figure 1.8 for the definition of these terms) mechanical features presented by the tooth supporting apparatus.

Few works [70, 98, 160] were also focussed on the fluid contribution to dental support mechanisms. Phenomena like PDL fluid movements during cyclic loading and interstitial fluid pressure changes during traumatic occlusional loading were observed, suggesting that interstitial fluid plays an important role in dental biomechanics.

1.4.3 Periodontal specimens

This approach aims the direct measurement of the PDL properties via excision of small periodontal specimens (see figure 1.6b) containing bone, PDL and cementum-dentin portions. Two specimen geometries are generally tested: the **shear specimen** and the **uniaxial specimen**. The assets of this category of specimens are that they provides for better control of the geometry and allow for more accurate identification of material parameters; the specimens are subjected to simple and well defined loading configurations, allowing thus for a more reliable interpretation of the results. Among the drawbacks of this technique are the time-consuming specimen preparation, their usually small size and fragility and the loss of *in-vivo* conditions, resulting in possible artifacts affecting the biomechanical response of the tissue.

Shear specimens

Transverse sections, i.e., slices of bone containing (one or more) root portions held to the bone by the PDL, are cut normally to the tooth vertical axis. The main purpose is to apply extrusive (towards the crown) and/or intrusive (towards the root tip) loadings, thus simulating the physiological chewing stimulus. To this end, in general, the bony part of the transverse section is held fix, while the tooth part is pushed out with a flat rod. For this type of specimens, the calculation of stresses and strains, however, becomes a complex task depending on the extent of the irregularity of the root shape.

Ralph [118] was the first to perform tests on such a specimen geometry. As lately observed by Mandel *et al.* [82], the shear response of the PDL showed to be non-linear and hysteretic during loading-unloading processes. Chiba and Komatsu, with coauthors [25, 27, 71–75], carried out a wide experimental study based on this type of specimens. Material parameters dependencies on site of extraction, rate of loading, fiber orientation and age of the subjects were investigated with rat incisor specimens. Briefly, the data showed the mechanical shear response of the PDL to depend on location along the root, to be viscous and age dependent. This last observation was however contradicted by Yamane [164]. Experiments by Toms *et al.* [146] on human tissue resulted in age-, location- and load-direction-dependent PDL properties. The latter dependency, indicating an anisotropic behavior of the PDL, was however not confirmed in a recent study by Sanctuary *et al.* [124] on bovine teeth. This study is, up to date, the only study where shearing of the same specimen was performed in both extrusive and intrusive directions. The discrepancy between the two works then, is probably the consequence of the different protocols followed for the assessment of the undeformed initial state of the tooth part with respect to the bone.

Uniaxial specimens

Bar-shaped specimens are often cut from the previously described transverse sections. Containing bone, PDL and cementum-dentin layers as shown in figure 1.6b (on the right) the uniaxial specimens are suitable specimens as far as (i) tensile and/or compressive tests, (ii) accurate load-deformation to stress-strain conversion and (iii) visual observation of the test are concerned.

A first work based on this type of specimens was done by Atkinson and Ralph [6] by using extracted human teeth presenting bone fragments that were still attached to the PDL. Elasticity of the soft tissue was observed but nothing was said about the non-linearity of the tensile response. Loading rate independency was also proved. The rupture mechanisms of the PDL were also observed in this work; the presence of PDL after rupture on both bone and cementum surfaces proved that the ligament failed in its bulk and that its fibers were still anchored to the hard tissues. This was confirmed by Ralph [117] who furthermore recorded the the PDL rupture occur in a step-like manner. Dorow *et al.* [38] observed viscoelastic and preconditioning (refer to section 1.5 for definitions) phenomena for tensile loading-unloading response of pig specimens. Durkee [42] and Pini *et al.* [105, 106] reported tensile and compressive loading responses for the same specimen. Human and bovine tissue was used, respectively. Whereas the tensile behavior did not show any relevant difference with what reported in previous works (e.g., non-linear elasticity, viscosity, strain rate insensitivity, preconditioning), the compressive response showed a very different behavior, characterized by a heavy dissipative process. Further investigation on this peculiarity was pursued in the works by Sanctuary *et al.* [125] and Shibata *et al.* [130], still on bovine teeth. High dissipative processes were confirmed for loading-unloading compressive displacements and assessed to be independent on specimen location. The absorbing capacity of the PDL is therefore not affected in spite of the high biological variability (i.e., morphological differences) observed between specimens.

1.5 Review of theoretical frameworks

Some of the most common theoretical frameworks chosen for the modeling of the periodontium are presented in this section.

Since the PDL is considered to play the central role in dental mobility (see section 1.3), most of the past works, summarized in section 1.5.1, were focussed on its description, often paying less (or not at all) attention to the surrounding hard tissues (described in section 1.5.2).

1.5.1 Periodontal ligament

Studies on the mechanical behavior of the PDL are numerous and investigate the many different aspects that this tissue presents. After early, very simplistic theoretical frameworks which modeled the PDL as a incompressible, homogeneous, isotropic and linear elastic material undergoing to small strains [137, 138], major advances in the theoretical development of finite strain and non-linear visco-elasticity, together with the introduction of the theory of porous media in the domain of soft tissue biomechanics, allowed, in the past decade, the approaching of a more realistic description of the mechanical behavior of this very particular ligament.

Figure 1.8 presents some characteristic features of the mechanical behavior of the PDL when tested in different loading conditions:

1. **Non-linear stress-strain relationship**

   When pulled in tension, the PDL shows a sigmoidal stress-strain relationship (see, for instance figure 1.8a, curve 10^2). This response is typical for soft tissues and is generally charged to the uncrimping with progressive pulling of the *spaghetti*-like collagen mesh. Monotonic tensile loading of the PDL was described as *non-linear elastic*.

2. **Strain rate dependancy**

   The stress response of the PDL prove to be dependent on the tensile loading strain rate (figure 1.8a). The behavior seemed

(a)

(b)

(c)
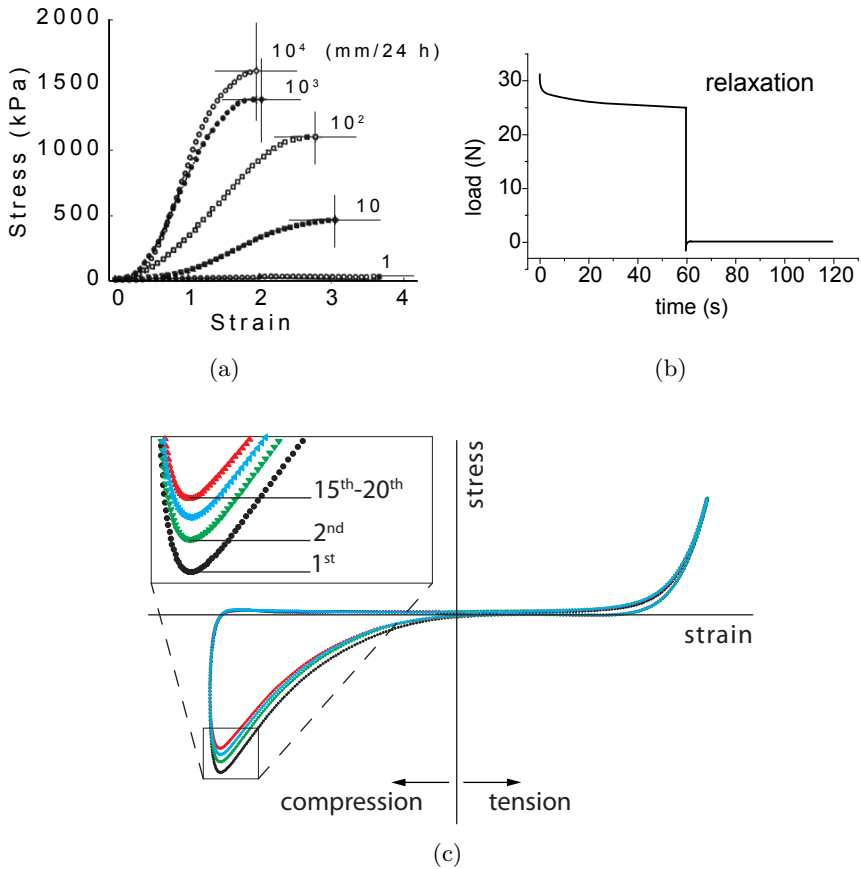
Figure 1.8: Characteristic features of the mechanical behavior of the PDL. Non-linear tensile stress-strain relationship and strain rate dependancy (a), from [25]; relaxation curve (b), from [130]; stress response to sinusoidal tensile-compressive strain cycles (c) showing preconditioning (more pronounced for the compressive phase), from [123].

to depend on the history of the applied loading, indicating thus *viscous* properties of the PDL mechanical behavior.

3. **Relaxation**

   When rapidly pulled in tension to a certain strain, and held in this state for a given time, the recorded load asymptotically diminished toward a certain load level (figure 1.8b). This phenomenon, known as *relaxation*, is also an indicator of a viscous type of behavior.

4. **Tensile-compressive behaviors**

   For the PDL, physiological stimuli include both tensile and compressive loadings. Subjecting this tissue to sinusoidal tensile-compressive strains, resulted in the stress response showed in figure 1.8c. The two phases showed remarkably different behaviors. While the tensile phase was practically *elastic* (i.e., the curves for the tensile loading and unloading paths were superposed, and the *hysteresis* —the area enclosed between these two curves— was almost zero), the compressive phase showed to be highly *dissipative* (almost all the mechanical energy used to compress the ligament was not retrieved when the ligament was pulled back in its initial configuration).

5. **Preconditioning**

   A typical feature for soft living tissues is the so called *preconditioning*. When cyclically loaded, the tissues response slightly softens with the increasing number of cycles. As showed in figure 1.8c, in the case of the PDL, this phenomenon was more evident for the compressive than for the tensile phase, and tended to vanish after a certain number of cycles (from the 15th cycle on, the responses practically superposed). In such a steady state, the tissue is said to be *preconditioned* [50].

The following is an overview of the theoretical frameworks used to model the mechanical features of the PDL described above.

Linear elasticity

Although the PDL clearly showed a nonlinear behavior (which has been known since very early (1935) mechanical tests, [43]), many researchers [2, 3, 114, 120, 143, 168] modeled nonetheless the PDL as linear elastic. To fully characterize such a material, described, in one dimension, by the Hooke's law

$$\sigma = E\epsilon \tag{1.1}$$

and, in three dimensions, by the Kirichhoff - St. Venant constitutive equation

$$\mathbf{S} = \lambda(Tr\mathbf{E})\mathbf{I} + 2\mu\mathbf{E} \tag{1.2}$$

is enough to provide one of the two couples of material constants: (i) the *elastic modulus* (or *Young modulus*) E and the *Poisson's ratio* ν or (ii) the elastic Lamé constants λ and μ. These constants are related via

$$E = \frac{\mu(3\lambda + 2\mu)}{\lambda + \mu} \quad \text{and} \quad \nu = \frac{\lambda}{2(\lambda + \mu)} \tag{1.3}$$

In this case, the stress (the Cauchy stress σ or the second Piola-Kirchhoff stress sensor $\mathbf{S}$, see chapter 2 for definitions) are linearly related to the deformation (the strain ϵ or the Green-Lagrange strain tensor $\mathbf{E}$).

Elastic moduli, or, more appropriately, *tangent elastic moduli E* (as the elastic modulus is defined as the slope of the stress-strain curve at strain equal zero, thus $E_{PDL} \cong 0$), were assessed as the slope of the stress-strain curves at a certain arbitrary strain. This is the reason why their values span over six orders of magnitude, from 0.05MPa [151] to 1750MPa [53].

Since living tissues are mainly made of water, the common assumption for what concerns the Poisson's ratio, which governs the compressibility of the tissue, has been to set it equal to $\nu = 0.49$ [2, 29, 143], meaning that, like water, the material is practically incompressible. However, verified values for ν can not be found in the literature. In fact, this constant is only defined for linear elastic materials, and the PDL is clearly not linear elastic. Furthermore, the experimental measurement of such a constant results to be a quite hard task in the case of

the PDL. Thus, other values spanning practically the entire theoretical range for the Poisson's ratio (i.e., 0.0 to 0.49 [157]), where selected to describe the PDL.

Non-linear elasticity

More recently, studies on the PDL have assigned nonlinear properties to this tissue [40–42, 93, 103, 145, 146]. The majority of the proposed constitutive equations was based on piecewise linear elastic laws. The non-linear stress-strain curve was divided into several zones that were then individually approximated by linear stress-strain relationships, i.e., by different values for elastic modulus and Poisson's ratio for each zone.

Another way to express non-linear elasticity, is to derive the constitutive equations governing the material's mechanical behavior from appropriate strain energy potentials. The tensile behavior of the PDL being similar to the one of other soft tissues, the energy potentials proposed to model their mechanical behaviors was used. Two of the most common potentials are (i) the one proposed by Veronda and Westmann [150] for modeling skin behavior

$$\mathcal{W} = \alpha \exp\left[\beta(I_1 - 3)\right] - \frac{\alpha\beta}{2}(I_2 - 3) \tag{1.4}$$

where α and β are elastic parameters and I_1 and I_2 are strain invariants (see chapter 2, equation 2.29 for definitions) — this potential was also used by Pioletti *et al.* [110] to model knee ligaments — and (ii) the one proposed by Ogden [96]

$$W = \sum_{n=1}^{N} \frac{\mu_n}{\alpha_n} \left(\lambda_1^{\alpha_n} + \lambda_2^{\alpha_n} + \lambda_3^{\alpha_n} - 3\right) \tag{1.5}$$

where μ_n and α_n are material constants and λ_i are the principal stretches.

Lately, refinement of the non-linear elastic laws allowed to introduce material anisotropy [91], accounting for tissue structural arrangement.

In this case, the strain energy potential splits into two contributions

$$\mathcal{W} = \mathcal{W}_{ECM} + \mathcal{W}_{CFs} \tag{1.6}$$

where $\mathcal{W}_{ECM}$ represents the strain energy potential of the extracellular matrix of the form of equation 1.4, and $\mathcal{W}_{CFs}$ is the strain energy potential of the collagen fibers, function of additional invariants dependent on fibers orientation (refer to [61, 97] for details).

Linear and nonlinear visco-elasticity

Viscoelastic theoretical models of the PDL are rarely found in the literature, although, since more than 40 years [13], viscoelastic properties (e.g., strain rate dependency, relaxation and creep behavior, preconditioning) are known features of the PDL mechanical behavior [25, 74, 125, 136, 140, 159].

One among the first works which tried to incorporate the viscous aspects to the mechanics of the PDL is the one by Toms *et al.* [144], who used the theory of *quasi-linear viscoelasticity* (QLV) developed by Fung [50]. In this theory, the stress response $K(\lambda, t)$ to a stretch step is represented by

$$K(\lambda, t) = G(t)T^{(e)}(\lambda) \tag{1.7}$$

where $G(t)$ is the *reduced relaxation function* (a decaying 3 terms exponential function was chosen in [144]), and $T^{(e)}$ the instantaneous *elastic response* of the tissue.

Natali *et al.* [92] lately proposed that the PDL response be formulated by means of a specific *Helmholtz free energy density*

$$\psi(\mathbf{C}, \mathbf{q_i}) = \mathcal{W} - \frac{1}{2}\sum_{i=1}^{n} \mathbf{q_i} : \mathbf{C} \tag{1.8}$$

defined as the difference between an anisotropic hyperelastic stored energy contribution ($\mathcal{W}$) and the energy dissipated during viscous processes (the sum of the scalar products between the internal parameters

$\mathbf{q_i}$, expressing material evolution, and the right Cauchy-Green strain tensor $\mathbf{C}$), represented as a Zener mechanical model (a spring connected in parallel with n viscoelastic branches made of serial spring-dash-pot elements). This model was able to well describe strain rate dependency, relaxation phenomena and hysteretic *tensile* behavior of the PDL.

Still in the framework of linear viscosity, the very recent work by Zhurov *et al.* [170] proposed an accurate model accounting for the compressible, transverse isotropic, visco-hyperelastic large strain PDL behavior. However, up to date, no comparison of the obtained model with experimental results are proposed.

Experimental tests also proved the non-linear character of the PDL viscosity [125]. In the study of the PDL mechanical response, to the author's knowledge, only the work by Justiz [65] attempted to describe such a nonlinearity. Nonlinear power law springs and dash-pots with adjustable exponents allowed to describe the observed large strains *stiffening elasticity* and low strain rates *thinning viscosity* (i.e. pseudo-plasticity). Furthermore, a piecewise split formulation based on the sign of the deformation tensor allowed for the model to include the tensile-compressive dissimilarities.

Other theoretical frameworks developed for the description of linear and nonlinear visco-elastic properties of soft tissues as knee ligaments [110], blood vessels [60] and soft tissues in general [16, 109] can be adapted to the modeling of PDL.

Poro-elasticity and Theory of porous media

The porous media approach, historically derived from the theory developed for the description of saturated and unsaturated soils, has been integrated in theoretical frameworks for the formulation of soft tissues constitutive laws to account for their porous nature. Indeed, part of the time-dependent aspects described above (i.e., strain rate dependency and tensile-compressive dissimilarities) are likely to be captured by a porous material description, where a fluid can flow through a de-

formable porous solid matrix.

With application to the PDL, van Driel *et. al* [148] succeeded in modeling the response of a creep test by assigning to the PDL and to the surrounding alveolar bone poro-elastic properties. Furthermore, to obtain an optimal description, the PDL was split into two layers to which two different values of permeability were assigned.

In the model proposed by Natali *et al.* [94], biphasic mixture (porous solid and pore fluid) and small strains framework were assumed. Prevention for fluid exchanges between PDL and surrounding bone and cementum was imposed. The model proved to be quite accurate in the simulations of the experimental tests reported. Nevertheless, this model resulted to be inappropriate for the description of the physiological large strain PDL mechanical behavior.

More advanced works based on porous media descriptions, can be found in studies applied to other soft tissues;

Kenyon [69] developed a mathematical model, based on Biot's theory of porous media [14], for the description of water flux in porcine aortic wall; Holmes [59] applied a mixture model to interpret uniaxial compression of soft tissues; Yang [165] suggested that the viscoelastic behavior observed for the cardiac muscle was only partially apparent, and mostly due to poro-elastic effects. He's theory was based on Biot's description and accounted for large strains, material non-linearity and strain-dependent permeability. This last property was indeed enhanced in the work by Mansour and Mow [83], who found out that cartilage permeability decreased with increasing compressive strain. Permeability dependency on strain was also included in the models by Mow *et al.* [88] and Ehlers and Markert [45] for cartilage, and by Argoubi and Shirazi-Adl [4], Silva *et al.* [131] and Williams *et al.* [156] for lumbar disc mechanical description. Another recent noteworthy work is the one by Li *et al.* [79], based on the mixture theory of a compressible Neo-Hookean visco-hyperelastic solid matrix.

1.5.2 Cementum and alveolar bone

Compared to the PDL, cementum and alveolar bone are quite stiff [113,142]. In general, in finite element models of periodontium or whole tooth specimens, the two mineralized hard tissues are considered as linear elastic materials. Table 1.1 resumes the values adopted by various authors for the parameters necessary (i.e., Young's modulus E and Poisson's ratio ν) to describe the linear elastic behavior of a medium.

Table 1.1: Cementum and bone mechanical parameters; Young's modulus E (units in GPa), Poisson's ratio ν and porosity n.

Author		*Cementum*			*Bone*		
		E_C	ν_C	n_C	E_B	ν_B	n_B
Middleton *et al.*	[86]	18.6	0.31	-	13.8	0.26	-
Rees *et al.*	[120]	15.0	0.31	-	13.8	0.26	-
van Driel *et al.*	[148]	18.6	0.3	-	4.59	0.3	0.8
Natali *et al.*	[94]	20.0	0.25	-	∞	0.5	-
Pietrzak *et al.*	[103]	15.0	0.31	-	0.345	0.31	-
Dorow *et al.*	[39]	19.0	0.3	-	1.0	0.3	-
Ho *et al.*	[57]	14.0	-	-	18.0	-	-

Although clearly enhanced by histological studies, to the author's knowledge, no works, except the one by van Driel *et. al* [148], considered alveolar bone as a porous materials.

Other frameworks were developed for complex phenomena such as remodeling or damage (e.g., [2, 121]). These models are generally intended for the simulation of stress and strain distributions when metallic dental implants are grafted into the jaw bone.

1.6 Research motivations

Motivations for research in the field of dental biomechanics are well resumed in the introductory part of a work by Davidovitch [35] (1991) entitled *Tooth movement*.

≪*Throughout their natural history, teeth move and migrate...Following their emergence into the oral cavity, teeth reach a position in the dental arch, dictated by the forces of the surrounding muscles of the tongue, cheeks, and lips, and by contact with teeth of the opposite jaw. During mastication, teeth can move slightly in the vertical and horizontal directions, constrained by the PDL and the alveolar socket. Despite their large magnitude, masticatory forces do not alter the position of teeth, probably due to their short duration. However, in the presence of periodontal disease, when tissues of the periodontium are gradually destroyed, teeth can migrate into new positions, where the masticatory and functional forces reach equilibrium. Often, these new positions are aesthetically undesirable.*

Tooth position may be deemed undesirable due to functional and aesthetic considerations, prompting patients to seek orthodontic care. In its most simplistic translation, "orthodontics" means straightening teeth. This "straightening", or movement of teeth into desirable positions, is accomplished by the application of forces to teeth, usually of small magnitude (on the order of a few grams per square centimeter of dental root surface) and long duration (usually about 2 years). Millions of people are subjected annually to orthodontic treatment worldwide, making this branch of dental care a widespread and lucrative specialty...many general dentists worldwide provide orthodontic care to their patients, and all, specialists and generalists alike, base their therapeutic means upon the time-tested observation that teeth can be forced to move away from their position in the dental arch to new locations by means of applied mechanical forces.≫

Thus, understanding of the mechanisms (either mechanical, chemi-

cal or biological) that allow for the teeth to move within the jaw bone, is of paramount importance if one seeks to minimize time and costs of treatments, maximizing thus patient's satisfaction. Form a mechanical standpoint, this resumes to identify the constitutive laws describing the behavior of all the involved tissues; the surrounding alveolar bone, the PDL and the cementum.

1.7 Objectives

Only few works investigated the mechanical behavior of the periodontium while subjected to physiological stimuli (e.g., mastication). Indeed, studies in this field focused much more on it's response under pathologic (tensile rupture) or orthodontic (braces, implants) forces.

Subjecting the periodontium to more realistic *in-vivo*–like conditions while trying to capture the mechanisms involved in its mechanics, were the overall objectives of this thesis. More specifically, efforts were mainly focussed on the role played by the fluid component contained in these tissues.

To this end, the *extraction of specimens* and the *design of devices* allowing for *multiaxial loading*, together with the *structural, histological and morphological characterization* of the tissues involved were some of the challenges faced in this work.

1.8 Thesis outline

Following the present introduction, where a review of (i) the anatomy of the periodontium, (ii) the experimental techniques and (iii) the theoretical frameworks proposed in past studies for the mechanical characterization of the PDL is given, **Chapter 2** (page 33) exposes the tools allowing for the mathematical formulation of the mechanical problem. The description of the methodologies used to study the mechanical behavior of the PDL or to analyze its structure are reported in **Chapter 3** (page 55). The data obtained from the experiments are summarized

and analyzed in **Chapter 4** (page 95). In **Chapter 5** (page 155) a numerical model integrating the phenomena observed in the experimental tests is proposed. Finally, a conclusion, along with suggestions for future work, are given in **Chapter 6** (page 183).

Chapter 2

Theoretical Framework

In order to translate a sentence from English to French two things are necessary. First we must understand thoroughly the English sentence. Second, we must be familiar with the forms of expression peculiar to the French language. The situation is very similar when we attempt to express in mathematical symbols a condition proposed in words. First we must understand thoroughly the condition. Second, we must be familiar with the forms of mathematical expression.

G. Polya, 1887–1985
How to solve it [111]

2.1 Introduction

Experimental and theoretical works reported in the literature proved (see chapter 1) the PDL to be a very complex tissue, from both histo-morphological and biomechanical points of view, suggesting that many different features contribute to its mechanical behavior. The choice of the theoretical framework describing the physiological tensile-compressive mechanical behavior of the PDL was based on the following statements, summarizing the most relevant results on the description of its mechanical behavior:

1. Tensile tests [38,39,106,123] demonstrated that the PDL behaves as a non-linear elastic material undergoing large deformations.

2. Sinusoidal and relaxation tensile-compressive tests proved that the PDL possess non-linear viscoelastic properties [65, 125] The tensile time dependent features were less marked than the ones observed for compressive loading.

3. Interstitial fluid was noticed to be expelled out of the PDL during compressive loading [123]. This, together with histo-morphological observations [19], clearly indicated the porous nature of the periodontal ligament. Nevertheless, only the works by van Driel *et al.* [148] and by Natali *et al.* [94] tried to explain the mechanical behavior of the PDL via a biphasic material formulation, taking into account the presence of two different phases: a solid porous matrix and a pore fluid phase.

4. Furthermore, Provatidis [113], in its comparative study of iso- and anisotropic PDL numerical models, suggested that there were '...*serious indications that it was not probably the visco-elastic nature of the continuous PDL but rather the composition of the PDL as a composite mixture of fluid and fibers...*' that influenced tooth displacement and thus stresses.

5. The PDL presented a very complex structure [19]; its width, contour roughness, fibrous matrix orientation and blood vessels density were highly dependent on the sites of investigation. The structural pattern of the ligament did not follow any trend with position. However, the site of specimen extraction had no significant influence on the energy absorbing capability of the PDL [130].

6. The alveolar bone [9, 149, 153], cementum-dentin [115] and PDL [19, 147] porous characters, suggested that the whole periodontium should be considered as the elementary unit (also see [19]) when analyzing the mechanical behavior of the soft tissue, since fluid exchanges could occur between these three materials.

Based on these assertions, a framework able to describe the *hydro-mechanical* coupling (point 6) between a *porous* (point 3) *non-linear* (*linear*, for bone and cementum) *elastic* (points 1 and 4) solid matrix undergoing *finite* (*small*, for bone and cementum) deformations (point 1), and a pore filling fluid was chosen.

Despite its highly heterogeneous and anisotropic microscopic structure (point 5), *homogeneity* and *isotropy* were selected as properties of all the periodontal tissues. Moreover, all possible viscoelastic aspects (point 2) were not accounted for, in reason of point 4.

The choice to make use of known constitutive relations, aimed at the description of the mechanical behavior of the periodontium, was adopted since the establishment of original constitutive laws was beyond the scope of this work.

Note: The experimental testing procedures reported in chapter 3 (especially in the case of the *cylindrical specimens*) were designed as to experimentally determine to what extent the mechanical behavior of the PDL could be described within such a theoretical framework.

The above mentioned features of the PDL mechanical behavior led to the choice of a two-phase continuum description [7] of the tissues. In such a formulation, a medium is considered as a porous solid matrix saturated with a pore filling fluid. Equilibrium and continuity equations of such a system, furnish the coupled *hydro-mechanical* system of equations allowing for the description of the mechanical interaction of the two material (solid and fluid) phases (see section 2.4). One of the possible formulations is the theory of multiphase mixtures (section 2.3.3), which makes use of the concepts of *effective stress* (introduced by von Terzaghi [152] for the description of the stress state of a porous solid, 2.3.2) and of *Darcy's law* (expressing the fluid flow through the pores, 2.3.1), both defined in section 2.3. The concept of *hyperelasticity*, describing, within the framework of continuum theory, the finite non-linear elastic behavior of the solid matrix, is developed in section 2.2.

2.2 Continuum theory

The basics of *continuum mechanics* are summarized in this section. The definition of the general equations used to describe the mechanical behavior (stress-strain relationship) of hyperelastic media subjected to large deformations are given here.

Since the tools allowing for this description are tensors, large use of their related properties and algebra was made. The reader is addressed to the reference works [20, 32, 50, 62, 97, 108] for a more detailed development.

This overview of the continuum theory treats of:

- The *kinematics*, concerning the study of the body motion, and this independently on the forces that causes it, the constitution of the material and the type of motion.

- The *dynamics*, treating quantities like mass, linear and angular momentum and energy, which are all conserved during the motion. The concept of stress is introduced at this stage of the theory.

- The *constitutive relations*, introducing the model representing the material's behavior. This choice is based on both experimental and morphological observations, as well as theoretical considerations.

- The *strain energy function*, allowing for the description of hyperelastic constitutive behavior.

2.2.1 Kinematics of a continuum

In solid mechanics it is common to use the initial undeformed (and usually known) configuration Ω_0 of a body $\mathcal{B}$ to define strains and stresses (as opposed to the current deformed configuration Ω used in fluid mechanics). This description is conventionally called *material* (or

lagrangian) description (as opposed to the *spatial* or *eulerian* description).
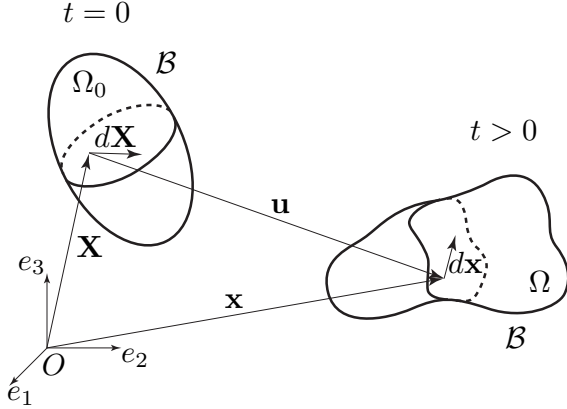
Figure 2.1: Reference and current configuration in *lagrangian* description.

In its initial (or reference) configuration Ω_0, a particle of the body $\mathcal{B}$ is labeled with its position vector $\mathbf{X}$ relative to some origin O and to an orthogonal cartesian frame $Oe_1e_2e_3$ (see figure 2.1). After some time t, that same particle is displaced and tracked in the current configuration Ω by its actual position vector $\mathbf{x}$. Since Ω_0 and Ω are configurations of the same body $\mathcal{B}$, it exists a bijection $\chi : \Omega_0 \rightarrow \Omega$ called *motion* (or *deformation*) such that

$$\mathbf{x} = \chi(\mathbf{X}, t) \quad \text{for all } \mathbf{X} \in \Omega_0, \qquad \mathbf{X} = \chi^{-1}(\mathbf{x}, t) \quad \text{for all } \mathbf{x} \in \Omega. \quad (2.1)$$

The displacement vector $\mathbf{u}$ is defined as

$$\mathbf{u} = \mathbf{x} - \mathbf{X} \overset{(2.1)}{=} \chi(\mathbf{X}, t) - \mathbf{X} \tag{2.2}$$

and the deformation gradient tensor $\mathbf{F}$ as

$$\mathbf{F}(\mathbf{X}, t) = \nabla\chi(\mathbf{X}, t) \equiv \nabla\mathbf{x} \tag{2.3}$$

where ∇ is the material gradient operator. In component form, equation (2.3) is written

$$F_{ij} = \frac{\partial \chi_i}{\partial X_j} \equiv \frac{\partial x_i}{\partial X_j} \qquad (2.4)$$

which can also be expressed by

$$d\mathbf{x} = \mathbf{F}d\mathbf{X} \qquad (2.5)$$

Note that the tensor $\mathbf{F}$ transforms an infinitesimal *reference* segment $d\mathbf{X}$ at the position $\mathbf{X}$, in an infinitesimal *deformed* segment $d\mathbf{x}$ at the position $\mathbf{x}$ following a linear transformation.

The tensor $\mathbf{F}$ represents a *measure* of the deformation induced by the motion χ. The main drawback of this measure is that it is not frame independent, i.e. different observers placed in different frames will have a different descriptor for the same movement. $\mathbf{F}$ is said to be *non objective*. In addition, $\mathbf{F}$ is not a symmetric tensor.

An *objective* description of the movement needs then to be introduced; the *right* Cauchy-Green deformation tensor, defined as

$$\mathbf{C} = \mathbf{F}^T\mathbf{F} \qquad (2.6)$$

is actually an alternative *objective* deformation descriptor, as well as the *left* Cauchy-Green deformation tensor, written as

$$\mathbf{c} = \mathbf{F}\mathbf{F}^T \qquad (2.7)$$

2.2.2 Dynamics of a continuum

Description of the dynamics of a continuum implies firstly the balance of mass, linear momentum, angular momentum and energy, and secondly the introduction of the stress tensor.

Mass conservation

This principle says that the initial mass of a body $\mathcal{B}$ remains unchanged after the motion χ, i.e. the mass expressed in the *material* form (reference configuration) is the same if expressed in the *spatial* form (actual configuration).

Introducing the two scalar quantities of *initial mass density* $P_0(\mathbf{X})$ and *actual mass density* $\rho(\mathbf{x}, t)$, which can also be expressed in material coordinates as

$$\rho(\mathbf{x}, t) = \rho\big(\chi(\mathbf{X}), t\big) = P(\mathbf{X}, t) \tag{2.8}$$

the principle of mass conservation is written as

$$\int_{\Omega_0} P_0(\mathbf{X}) \, dV = \int_{\Omega} \rho(\mathbf{X}, t) \, dv \tag{2.9}$$

dV and dv being the elementary volumes in the reference and actual configuration, respectively. These two quantities are related via

$$dv = \det(\mathbf{F}) \, dV = J \, dV \tag{2.10}$$

where J is the jacobian given by the determinant of $\mathbf{F}$, which, for invertibility of the motion χ, must satisfy the condition $0 < J < \infty$.

Introducing equations 2.8 and 2.10 into equation 2.9 and using the *localization theorem*[1], results in the relation

$$P_0(\mathbf{X}) = J \, P(\mathbf{X}, t) \tag{2.11}$$

which has to be satisfied to guaranty the principle of mass conservation.

Linear and angular momentum conservation, stress tensors

Two other important principles governing the dynamics of a continuum, are the conservation of linear and angular momentum. Hereafter they are expressed in the material form:

- Conservation of linear momentum
  The time derivative of the linear momentum of a part Π_0 of the body $\mathcal{B}$ at a given time t is equal to the resulting force (body forces

---

[1]Be f a continuous function defined over Ω. The localization theorem states that if $\int_\Omega f \, dV = 0$, then $f = 0$.

$\mathbf{F^b}$ *plus contact forces* $\mathbf{F^c}$*) applied to* Π_0 *at the same time* t.

$$\frac{d}{dt} \int_{\Pi_0} P(\mathbf{X}, t)\mathbf{V}(\mathbf{X}, t) \, dV$$

$$= \underbrace{\int_{\Pi_0} P(\mathbf{X}, t)\mathbf{B}(\mathbf{X}, t) \, dV}_{\mathbf{F^b}} + \underbrace{\int_{\partial\Pi_0} \mathbf{T}(\mathbf{X}, t, \mathbf{N}) \, dA}_{\mathbf{F^c}}$$

$$\forall \, \Pi_0 \subseteq \Omega_0 \quad (2.12)$$

- Conservation of angular momentum
  The time derivative of the angular momentum of a part Π_0 *of the body* $\mathcal{B}$ *at a given time* t *is equal to the resulting torque due to the forces (body and contact) applied to* Π_0 *at the same time* t.

$$\frac{d}{dt} \int_{\Pi_0} P(\mathbf{X}, t)\mathbf{X} \wedge \mathbf{V}(\mathbf{X}, t) \, dV$$

$$= \int_{\Pi_0} P(\mathbf{X}, t)\mathbf{X} \wedge \mathbf{B}(\mathbf{X}, t) \, dV + \int_{\partial\Pi_0} \mathbf{X} \wedge \mathbf{T}(\mathbf{X}, t, \mathbf{N}) \, dA$$

$$\forall \, \Pi_0 \subseteq \Omega_0 \quad (2.13)$$

where $\mathbf{V}(\mathbf{X}, t)$ is the velocity, $\mathbf{B}(\mathbf{X}, t)$ the body force density per reference unit volume and $\mathbf{T}(\mathbf{X}, t, \mathbf{N})$ is a vector force per reference unit area dA (thus a stress vector), which is function of the vector $\mathbf{N}$, normally oriented with respect to dA. $\partial\Pi_0$ represents the boundary of Π_0, where the contact forces apply.

From these two principles, the existence of a stress tensor $\mathbf{P}(\mathbf{X}, t)$, called *first Piola-Kirchhoff* stress tensor can be deduced [20], such that

$$\mathbf{T}(\mathbf{X}, t, \mathbf{N}) = \mathbf{P}(\mathbf{X}, t) \, \mathbf{N} \tag{2.14}$$

This tensor represents a measure of the stress field of each particle of the body $\mathcal{B}$ with respect to the reference configuration. This descriptor

is however *non objective*. An objective measure of stress is obtained by the *second Piola-Kirchhoff* stress tensor defined as

$$\mathbf{S}(\mathbf{X}, t) = \mathbf{F}^{-1}(\mathbf{X}, t)\, \mathbf{P}(\mathbf{X}, t) \tag{2.15}$$

Note: For a spatial description, the corresponding stress tensor is the classical *Cauchy* stress $\boldsymbol{\sigma}$ which represents the actual force acting on the deformed configuration. The relation between $\boldsymbol{\sigma}$ and $\mathbf{S}$ is given by

$$\boldsymbol{\sigma} = J^{-1}\mathbf{F}\,\mathbf{S}\,\mathbf{F}^{T} \tag{2.16}$$

and inversely

$$\mathbf{S} = J\,\mathbf{F}^{-1}\boldsymbol{\sigma}\,\mathbf{F}^{-T} \tag{2.17}$$

Thermodynamics of a continuum

Finally, the principles related to the thermodynamics of a continuum have to be satisfied. It's about the first and second principles of thermodynamics which, in the material description, states:

- First principle of thermodynamics — energy conservation:
  The time derivative of total energy (kinetic energy E_{kin} and internal energy E_{int}) in a body $\mathcal{B}$ is equal to the sum of the power of the forces (body and contact) and the rate of heat received by the material.

  If only isothermal processes are considered, energy conservation writes

$$\underbrace{\int_{\Omega_0} P_0 \frac{D}{Dt}\left(\frac{\mathbf{V}\cdot\mathbf{V}}{2}\right) dV}_{\frac{D}{Dt}E_{kin}} + \underbrace{\int_{\Omega_0} \mathbf{P} : \dot{\mathbf{F}}\, dV}_{\frac{D}{Dt}E_{int}}$$

$$= \overbrace{\int_{\Omega_0} P_0 \mathbf{B}\cdot\mathbf{V}\, dV}^{\text{body forces power}} + \overbrace{\int_{\partial\Omega} \mathbf{T}\cdot\mathbf{V}\, dA}^{\text{contact forces power}} \tag{2.18}$$

(The notation ':' represent the scalar product[2] between second order tensors)

- Second principle of thermodynamics — entropy:
  The time derivative of total entropy in a body $\mathcal{B}$ is always greater than or equal to 0.

It is important to note that the internal power, the term $\frac{D}{Dt} E_{int}$ in 2.18, can also be rewritten as

$$\mathbf{P} : \dot{\mathbf{F}} = \mathbf{S} : \dot{\mathbf{E}} = P_0 \dot{U} \tag{2.19}$$

where $\mathbf{E} = \frac{1}{2}(\mathbf{C} - \mathbf{I})$ is the *Green-Lagrange deformation tensor* and U is a function defining the internal energy density (per reference volume). Note that the pairs $\mathbf{P}, \dot{\mathbf{F}}$ and $\mathbf{S}, \dot{\mathbf{E}}$ are *conjugate* parameters.

2.2.3   Constitutive equations

To describe the mechanical behavior of a material it is then necessary to find a mathematical expression relating the strains to the stresses. Such an expression is called *constitutive equation* (or *constitutive law*). Its form is largely based on experimental and morphological observations; the shape of the curve, obtained in simple (and appropriate) mechanical tests, tells how the material behaves under certain loading conditions, shedding light on the type of constitutive equations that likely best model the mechanical response. Additionally, the microscopic structure of the material generally provides information on the mechanisms involved during the deformation.

Because a material reacts differently depending on environmental (or boundary) conditions (e.g., temperature, humidity) and mechanical loads, a constitutive relation is sought to describe its behaviour under well-defined conditions.

---

[2]$\mathbf{A} : \mathbf{B} = \sum_{i,j=1}^{3} A_{ij} B_{ij}$

Hyperelesticity

As already stated, the tensile behavior of the PDL can be assumed to be non-linear elastic when subjected to large (physiological) strains. To describe such a behavior, it is common to assume the hypothesis of the existence of an energy potential $\mathcal{W}(\mathbf{X}, t)$ [97] such that

$$\mathcal{W}(\mathbf{X}, t) = P_0(\mathbf{X})\, U(\mathbf{X}, t) \tag{2.20}$$

where $U(\mathbf{X}, t)$ is an internal energy density function.

The derivative of this expression with respect to time results in

$$\dot{\mathcal{W}}(\mathbf{X}, t) = P_0(\mathbf{X})\, \dot{U}(\mathbf{X}, t) \overset{(2.19)}{=} \mathbf{P} : \dot{\mathbf{F}} \tag{2.21}$$

Moreover, for a homogeneous material, this potential can also be written as function of the deformation gradient 2.3 only

$$\mathcal{W}(\mathbf{X}, t) = \mathcal{W}(\mathbf{F}) \tag{2.22}$$

with its time derivative given by

$$\dot{\mathcal{W}}(\mathbf{F}) = \frac{D\mathcal{W}(\mathbf{F})}{Dt} = \frac{D\mathcal{W}(\mathbf{F})}{D\mathbf{F}} : \frac{D\mathbf{F}}{Dt} = \frac{\partial \mathcal{W}(\mathbf{F})}{\partial \mathbf{F}} : \dot{\mathbf{F}} \tag{2.23}$$

where the operator $D(\cdot)/Dt = \partial(\cdot)/\partial t + \mathrm{grad}(\cdot) \cdot \mathbf{v}(\mathbf{x}, t)$ denotes the material time derivative ($\mathbf{v}(\mathbf{x}, \mathbf{t})$ being the spatial velocity). Eventually, the comparison of equations 2.21 and 2.23, results in the first Piola-Kirchhoff stress tensor written as

$$\mathbf{P} = \frac{\partial \mathcal{W}(\mathbf{F})}{\partial \mathbf{F}} \tag{2.24}$$

To be valid, the potential energy function $\mathcal{W}$ must satisfy the principle of *objectivity*. This is the case if the potential energy can be expressed in terms of the objective tensor $\mathbf{C}$ instead of $\mathbf{F}$. The new energy function is then $\widehat{\mathcal{W}}(\mathbf{C})$ and is related to $\mathbf{P}$ via (see [20])

$$\mathbf{P} = 2\mathbf{F}\frac{\partial \widehat{\mathcal{W}}(\mathbf{C})}{\partial \mathbf{C}} \tag{2.25}$$

By using 2.15, equation 2.25 can be expressed in terms of the objective second Piola-Kirchhoff stress tensor as

$$\mathbf{S} = 2\frac{\partial \widehat{\mathcal{W}}(\mathbf{C})}{\partial \mathbf{C}} \tag{2.26}$$

In addition to objectivity (i.e., frame independency), to be valid, the potential energy function must be zero for the reference configuration (i.e., $\widehat{\mathcal{W}}(\mathbf{I}) = 0$) and must be convex (i.e., $\widehat{\mathcal{W}}(\mathbf{C}) \geqslant 0$).

Incompressibility and compressibility

If incompressibility is assumed (hypothesis often imposed for the description of soft biological tissues, mainly composed of water), there is no change between the volumes dV before and dv after the motion χ. Thus. equation 2.10 becomes

$$J = \det(\mathbf{F}) = 1 \qquad \Leftrightarrow \qquad I_3(\mathbf{C}) = 1 \tag{2.27}$$

where $I_3(\mathbf{C})$ is the third invariant of $\mathbf{C}$ (see equation 2.29 below for definition).

For compressibility $J > 1$.

Isotropy

The form of the strain energy function $\mathcal{W}$ also must reflect possible symmetries of the material. In the simplest case of an *isotropic*[3] material, the potential $\widehat{\mathcal{W}}$ can be expressed as a function of the *principal invariants*[4] I_i or the *principal stretches* λ_i of its argument $\mathbf{C}$

$$\widehat{\mathcal{W}}(\mathbf{C}) = W\big(I_1(\mathbf{C}), I_2(\mathbf{C}), I_3(\mathbf{C})\big) = \phi(\lambda_1, \lambda_2, \lambda_3) \tag{2.28}$$

---

[3]A material is said to be *isotropic* if it shows identical mechanical properties in all testing directions.

[4]The invariants of a tensor represent, as stretches do, a measure of deformation.

where the three invariants of $\mathbf{C}$ are

$$I_1(\mathbf{C}) = tr(\mathbf{C}) \equiv \lambda_1^2 + \lambda_2^2 + \lambda_3^2$$
$$I_2(\mathbf{C}) = \frac{1}{2}\left((tr\mathbf{C})^2 - tr(\mathbf{C})^2\right) \equiv \lambda_1^2\lambda_2^2 + \lambda_2^2\lambda_3^2 + \lambda_3^2\lambda_1^2 \qquad (2.29)$$
$$I_3(\mathbf{C}) = det(\mathbf{C}) \equiv \lambda_1^2\lambda_2^2\lambda_3^2$$

Thus, equation 2.26 is rewritten as

$$\mathbf{S} = 2\frac{\partial W\left(I_i(\mathbf{C})\right)}{\partial \mathbf{C}} = 2\left(\frac{\partial W}{\partial I_1}\frac{\partial I_1}{\partial \mathbf{C}} + \frac{\partial W}{\partial I_2}\frac{\partial I_2}{\partial \mathbf{C}} + \frac{\partial W}{\partial I_3}\frac{\partial I_3}{\partial \mathbf{C}}\right) \qquad (2.30)$$

where

$$\frac{\partial I_1}{\partial \mathbf{C}} = \mathbf{I}, \qquad \frac{\partial I_2}{\partial \mathbf{C}} = I_1\mathbf{I} - \mathbf{C}, \qquad \frac{\partial I_3}{\partial \mathbf{C}} = I_3\mathbf{C}^{-1} \qquad (2.31)$$

so that 2.30 becomes

$$\mathbf{S} = 2\left(\frac{\partial W}{\partial I_1}\mathbf{I} + \frac{\partial W}{\partial I_2}(I_1\mathbf{I} - \mathbf{C}) + \frac{\partial W}{\partial I_3}I_3\mathbf{C}^{-1}\right) \qquad (2.32)$$

Note that, when incompressibility 2.27 is assumed, 2.32 simplifies to

$$\mathbf{S} = -2p\mathbf{C}^{-1} + 2\left(\frac{\partial W}{\partial I_1}\mathbf{I} + \frac{\partial W}{\partial I_2}(I_1\mathbf{I} - \mathbf{C})\right) \qquad (2.33)$$

where $p = -2\frac{\partial W}{\partial I_3}I_3$ is an hydrostatic pressure-like parameter.

Using equations 2.16 and 2.7 and the tensor property $(\mathbf{AB})^{-1} = \mathbf{B}^{-1}\mathbf{A}^{-1}$, it is possible also to express the Cauchy stress as

$$\boldsymbol{\sigma} = -2pJ^{-1}\mathbf{I} + 2J^{-1}\left(\frac{\partial W}{\partial I_1}\mathbf{c} + \frac{\partial W}{\partial I_2}(I_1\mathbf{c} - \mathbf{c}^2)\right) \qquad (2.34)$$

2.2.4 The strain energy function W

In the literature a large number of strain energy functions describing the hyperelastic behavior of materials is available. *Neo-Hookean, Mooney-Rivlin* or *Ogden* strain energy potentials are among the most known

and used. All of these potentials, however, do not account for material compressibility.

Experimental results (refer to section 4.4.5), proved the PDL to be highly compressible. Strain energy potentials allowing for compressibility were thus sought. Hill [56] extended the strain energy function proposed by Ogden [96] to the compressible case by incorporating in it the third invariant $I_3 = J$ of the deformation gradient

$$W = \sum_{k=1}^{N} 2\frac{\mu_k}{\alpha_k^2} \left[\lambda_1^{\alpha_k} + \lambda_2^{\alpha_k} + \lambda_3^{\alpha_k} - 3 + f(J) \right] \tag{2.35}$$

where $f(J)$ is the volumetric function accounting for compressibility. Storakers [135] suggested that

$$f(J) = \frac{1}{\beta_k}(J^{-\alpha_k \beta_k} - 1) \tag{2.36}$$

In these expressions, N is the order of the potential and μ_k, α_k and β_k are material parameters such that

$$\mu_0 = \sum_{i=1}^{N} \mu_i \qquad \text{and} \qquad \nu_i = \frac{\beta_i}{1 + 2\beta_i} \tag{2.37}$$

are the initial shear modulus and the Poisson's ratios, respectively.

2.3 Mechanics of porous media

As already mentioned, there was evidence of the –at least– biphasic PDL nature, consisting in a solid matrix (made of collagen fibers, blood vessels and ground substance) and a fluid content (blood, water). In fact, when subjected to mechanical loading, the soft tissue's matrix deformed, letting the fluid content flow through its pores [123].

Such phenomena correspond well to the ones observed in the field of geomechanics (where soils are considered as deformable matrix saturated with ground water) for which they have been widely described

and translated into mathematical expression [36,78,79,152]. Two main theories are still used nowadays for the description of multiphase continua: (i) the Biot Theory (BT), which find its basics in the fundamental works by K. von Terzaghi [152]; and (ii) the Theory of Porous Media (TPM), referring mostly to the works by Fillunger [47]. Although the two approaches generally lead to similar results [21], the solid–fluid interactions are modeled in quite different ways. In fact, if for the first approach balance equations and constitutive laws are given for the whole (macroscopic) medium, and the coupling between solid and fluid is guaranteed by introducing an additional material parameter, in the second approach the porous medium is considered as a mixture of overlapping phases occupying the same region of the space simultaneously, and the solid–fluid interactions are derived from consideration on the thermodynamics of immiscible mixtures, together with the concept of volume fractions (see below for details).

In the following, a framework describing the hydro-mechanical coupling based on Darcy's law (2.3.1), Terzaghi's concept of *effective stress* (section 2.3.2) and on the theory of multiphase mixtures (2.3.3) is presented.

2.3.1 Darcy's law

Darcy's experimental results has been essential for a continuum description of the motion of a liquid through a porous solid. He obtained the constitutive behavior for pore fluid flow by observing the proportionality between the total volume of water running through a column of compacted sand and the loss of pressure in the liquid. The relationship

$$Q = -k \, \frac{A \cdot \Delta p}{h} \qquad (2.38)$$

was deduced, where Q represents the total volume of fluid percolating per time unit (i.e., the discharge) through the column of sand of cross-sectional area A and height h and subjected to a pressure difference Δp. k is a proportional factor called permeability. The negative sign is needed because fluid flows from high pressure to low pressure.

The expression of Darcy's flux q is obtained by dividing both sides of equation 2.38 by the area A

$$q = -k\frac{\Delta p}{h} \qquad (2.39)$$

Note that this quantity do not express the velocity v_f of the fluid travelling through the pores. In fact, v_f is related to q via $v_f = q/n$ to account for the fact that only a fraction of the total volume is available for flow. The quantity n

$$n = \frac{V_f}{V} \qquad (2.40)$$

is the porosity of the medium, defined as the volume of fluid V_f divided by the total volume V.

The three-dimentional expression for such a flux, accounting for the insensitivity to the gravitational pressure drop, is given by

$$\mathbf{q} = -\mathbf{k}(\nabla\mathbf{p} - \rho_f\mathbf{g}) \qquad (2.41)$$

where the flux $\mathbf{q}$ is now a vector, $\mathbf{k}$ is the permeability tensor, $\nabla\mathbf{p}$ is the pressure gradient, $\mathbf{g}$ the gravity vector and ρ_f the fluid density. Similarly, the fluid velocity vector $\mathbf{v_f}$ is obtained by dividing equation 2.41 by the porosity n.

The permeability k, called *absolute permeability*, depends on both fluid (mechanical) and solid (geometrical) properties. In fact, the ease with which the fluid can flow through the pore space depends on the porosity n of the solid matrix, on its pore geometry S_0 [1/cm] (the specific area per unit volume of matrix particles) and on the mechanical properties (the unit weight γ and the viscosity η) of the fluid involved following the Kozeny-Carman equation [23, 166]

$$k = \frac{\gamma}{\eta}\frac{1}{C_{K-C}}\frac{1}{S_0^2}\frac{n^3}{(1-n)^2} \qquad (2.42)$$

where C_{K-C} is the Kozeny-Carman constant.

Thus, for a highly compressible solid matrix, where porosity and pores geometry vary with deformation, the permeability also results to be function of the amount of strain.

2.3.2 Terzaghi's concept of effective stress

Karl von Terzaghi is considered as one of the fathers of the modern theory of porous media. The very important concept of *effective stress* describing the distribution of stresses in a porous saturated medium is generally attributed to his work of 1923 [152].

Von Terzaghi stated that the level of pressure of the filling fluid do not contribute to the overall strength of a porous soil. It is, in fact, the unique *effective stress* that governs its deformability and stiffness. From a physical point of view, the *effective stress* can be interpreted as the stress that the grains constituting the solid matrix develop in their contact points. Summarizing, there are three kind of stresses that come into play:

- The pore *fluid pressure* p, an hydrostatic, shear-free stress state uniformly distributed over the fluid *and* the solid skeleton.

- The *effective stress* $\boldsymbol{\sigma}'$, the mean stress state only carried by the solid matrix.

- The *total stress* $\boldsymbol{\sigma}$, the sum of the *pore fluid* and the *effective stress*.

These quantities are then related via

$$\boldsymbol{\sigma}' = \boldsymbol{\sigma} - p\mathbf{I} \tag{2.43}$$

where $\boldsymbol{\sigma}'$ and $\boldsymbol{\sigma}$ are here expressed, in spatial description, as *Cauchy* stress tensors and $\mathbf{I}$ is the second-order identity tensor.

Hence, the effective stress $\boldsymbol{\sigma}'$ is a fraction of the total stress $\boldsymbol{\sigma}$, the difference being introduced by the hydrostatic pore fluid pressure p.

2.3.3 Theory of multiphase mixtures

One of the theories developed to describe the mechanical behavior of a porous medium considers the medium as a multiphase mixture of superposed deformable continua, simultaneously occupying the same region of the three-dimentional space [7].

When writing the balance equations for every single phase, interactions between phases are accounted for with additional coupling terms, drawn by the concepts of *phase immiscibility* and *volume fraction*. Particularly, this latter concept enhance the macroscopic scale character of this theory, which considers the medium as isotropic, neglecting thus all the microscopic structural anisotropy.

Balance of mass

The volume fractions occupied by the solid and the fluid phases are given by

$$\phi^s = V_s/V$$
$$\phi^f = V_f/V$$

where V_α is the volume of the α-phase (s for solid and f for fluid) and V is the total volume. In the case of a fully saturated medium, $\phi^s = n-1$ and $\phi^f = n$, where n is the porosity.

The expression of the balance of mass for the solid phase in the *eulerian* description is written as

$$\frac{D\rho^s}{Dt} + \rho^s \operatorname{div} \mathbf{v}_s = 0 \tag{2.44}$$

where ρ^s is the *partial* density of the solid matrix, $\mathbf{v}_s$ is the solid's velocity vector and $D(\cdot)/Dt$ stands for the material time derivative operator.

Similarly, the mass balance for the fluid phase is given by

$$\frac{D\rho^f}{Dt} + \rho^f \operatorname{div} \mathbf{v}_s = -\operatorname{div} \mathbf{q} \tag{2.45}$$

where ρ^f is the *partial* density of the fluid phase and $\mathbf{q}$ is the *eulerian* relative flow of the fluid with respect to the solid. The *partial* densities ρ^α are related to the *true* densities ρ_α via

$$\rho^\alpha = \phi^\alpha \rho_\alpha \qquad (2.46)$$

Now, the expression of the bulk modulus K_α of the α phase (see [79])

$$K_\alpha = \rho_\alpha \frac{Dp_\alpha}{D\rho_\alpha} \qquad (2.47)$$

where p_s and p_f are the intrinsic *Cauchy* pressures of the solid and fluid phases, respectively, can be rewritten in the form

$$\frac{D\rho_\alpha}{Dt} = \frac{\rho_\alpha}{K_\alpha} \frac{Dp_\alpha}{Dt} \qquad (2.48)$$

and, using 2.46, equations 2.44 and 2.45 take the form

$$\frac{D(n-1)}{Dt} + \frac{n-1}{K_s} \frac{Dp_s}{Dt} + (n-1)\operatorname{div}\mathbf{v}_s = 0 \qquad (2.49)$$

$$\frac{Dn}{Dt} + \frac{n}{K_f} \frac{Dp_f}{Dt} + n\operatorname{div}\mathbf{v}_s = -\frac{1}{\rho_f}\operatorname{div}\mathbf{q} \qquad (2.50)$$

Finally, by adding these two last equations, the total *eulerian* mass balance for the mixture is

$$\frac{1-n}{K_s} \frac{Dp_s}{Dt} + \frac{n}{K_f} \frac{Dp_f}{Dt} + \operatorname{div}\mathbf{v}_s = -\operatorname{div}\mathbf{q} \qquad (2.51)$$

Balance of linear momentum

The total *Cauchy* stress $\boldsymbol{\sigma}$, being the sum of the partial stress tensors $\boldsymbol{\sigma}^s$ and $\boldsymbol{\sigma}^f$ arising from the solid and fluid phase stresses, respectively, can be expressed as

$$\boldsymbol{\sigma} = \boldsymbol{\sigma}^s + \boldsymbol{\sigma}^f \qquad (2.52)$$

By the theory of multiphase mixtures, the balance of the linear momentum of the two phases is written as (see [79])

$$\text{div}\,\boldsymbol{\sigma^s} + \rho^s\mathbf{g} + \mathbf{h}^s = \rho^s\frac{D\mathbf{v}_s}{Dt} \tag{2.53}$$

$$\text{div}\,\boldsymbol{\sigma^f} + \rho^f\mathbf{g} + \mathbf{h}^f = \rho^f\left(\frac{D\mathbf{v}_f}{Dt} + (\mathbf{v}_f - \mathbf{v}_s)\cdot\text{grad}\,\mathbf{v}_f\right) \tag{2.54}$$

where $\mathbf{g}$ is the gravity acceleration vector, $\mathbf{h}^\alpha$ is the body force per unit current volume of the solid matrix exerted on the α-phase and $\mathbf{v}_\alpha$ is the α-phase velocity vector. The term within the parentheses in equation 2.54 represents the material time derivative following the fluid phase motion.

Adding these two last equations and noticing that $\mathbf{h}^s + \mathbf{h}^f = 0$ since $\mathbf{h}^\alpha$ are internal forces, the total mixture momentum balance can be written as

$$\text{div}\boldsymbol{\sigma} + \rho\mathbf{g} = \rho^s\frac{D\mathbf{v}_s}{Dt} + \rho^f\left(\frac{D\mathbf{v}_f}{Dt} + (\mathbf{v}_f - \mathbf{v}_s)\cdot\text{grad}\,\mathbf{v}_f\right) \tag{2.55}$$

Introducing then the accelerations $\mathbf{a}_s = D\mathbf{v}_s/Dt$ and $\mathbf{a}_f = D\mathbf{v}_f/Dt$ and the total mass density of the mixture $\rho = \rho^s + \rho^f$, the final expression for equation 2.55 is

$$\text{div}\boldsymbol{\sigma} + \rho\,\mathbf{g} = \rho\,\mathbf{a}_s + \rho^f(\mathbf{a}_f - \mathbf{a}_s) \tag{2.56}$$

which, if the difference between the two accelerations is assumed to be small, becomes

$$\text{div}\boldsymbol{\sigma} + \rho\,\mathbf{g} = \rho\,\mathbf{a}_s \tag{2.57}$$

2.4 Hydro-mechanical coupling

All of the equations needed for the description of the finite deformation of a porous saturated medium have been stated in the previous sections. It only remains to summarize and rephrase them all with respect to a reference configuration (i.e., using a *lagrangian* description).

Equations of mass 2.51 and momentum 2.57 conservation can be expressed (see [79] for details) in *lagrangian* description by

$$\frac{1-n}{K_s}\frac{D(Jp_s)}{Dt} + \frac{n}{K_f}\frac{D(Jp_f)}{Dt} +$$
$$+ \left[1 - \frac{(n-1)p_s}{K_s} - \frac{np_s}{K_f}\right]\frac{DJ}{Dt} = -\frac{1}{\rho_f}\text{DIV}\,\mathbf{Q} \quad (2.58)$$

and

$$\text{DIV}\,\mathbf{S} + J\rho\,\mathbf{g} = J\rho\,\mathbf{a}_s \quad (2.59)$$

respectively, where J is the Jacobian (see equation 2.10), $\mathbf{S}$ is the *second Piola-Kirchhoff* stress tensor defined in equation 2.17, DIV is the divergence operator evaluated with respect to the reference configuration and

$$\mathbf{Q} = J\mathbf{F}^{-1}\cdot\mathbf{q} \quad (2.60)$$

is the *Piola transform* (see [84]) of the flux $\mathbf{q}$ given by Darcy's law 2.41

$$\mathbf{q} = -\mathbf{k}(\nabla p - \rho_f\mathbf{g})$$

Finally, the total stress $\mathbf{S}$ can be expressed in terms of Terzaghi's *effective stress* and pore pressure 2.43 by

$$\boldsymbol{\sigma}' = \boldsymbol{\sigma} - p\mathbf{I}$$
$$J^{-1}\mathbf{F}\mathbf{S}'\mathbf{F}^T \overset{(2.16)}{=} J^{-1}\mathbf{F}\mathbf{S}\mathbf{F}^T - p\,\mathbf{I}$$
$$\mathbf{S}' \overset{(2.6)}{=} \mathbf{S} - J\,p\,\mathbf{C}^{-1} \quad (2.61)$$

where $\mathbf{S}'$ is the effective stress sensed by the solid matrix obtained via equation 2.32, where the strain energy function W, given by 2.35 and 2.36 is

$$W = \sum_{k=1}^{N} 2\frac{\mu_k}{\alpha_k^2}\left[\lambda_1^{\alpha_k} + \lambda_2^{\alpha_k} + \lambda_3^{\alpha_k} - 3 + \frac{1}{\beta_k}(J^{-\alpha_k\beta_k} - 1)\right]$$

Chapter 3

Materials and Methods

I think that in the discussion of natural problems we ought to begin not with the Scriptures, but with experiments, and demonstrations.

Galileo Galilei, 1564–1642

In this chapter, the techniques and methodologies used to study the structure, the morphology and the mechanical behavior of the periodontium are described.

The motivations justifying the choice of an *in-vitro* experimental setup can be found in section 3.1. In section 3.2 the motivations for the choice of bovine's tissue, and where and how it was obtained are exposed. After some common preliminary steps for the specimen extraction (section 3.3), techniques are described for the obtaining of the suitable specimens for histo-morphological (3.4) and mechanical (3.5) studies. The description of the devices and of the loading profiles used in the mechanical testing are reported in sections 3.6 and 3.7, respectively.

3.1 *In-vivo* versus *in-vitro* techniques

In-vivo and *in-vitro* techniques have both their advantages and drawbacks. In the first case, although allowing for physiological conditions, *in-vivo* testing is rarely well suited for the determination of accurate

constitutive behaviors. Indeed, the generally complex geometry of the considered system, as well as the difficulties to access to perform measurements on it, are clear hindrances to that end. In the second case, *in-vitro* techniques represent the best solution to that kind of problems, but the physiological environment is usually lost, resulting in possible artifacts affecting the biomechanical response of the tissue.

The strategy chosen for this work aimed to the combining of the advantage of both techniques. This was achieved by creating a closed environment, recreating as close as possible the physiological conditions, where to test the excised *in-vitro* specimens.

3.2 Selection of tissue

As already mentioned in section 1.2, one of the ultimate long-term goals of this research is to understand and model the mechanical behavior of the periodontium to allow thus dentists and orthodontists in planning optimal strategies for the treatment of pathological situations. For findings to be immediately used in concrete applications, human tissues, then, should have been the natural choice for the investigation on the physiological and mechanical functioning of the PDL. Nevertheless, by weighting the advantages and disadvantages of using human or animal specimens, it turned out the latter to be of better convenience.

In fact, in Switzerland, the handling of biological living or post-mortem tissues for academic or industrial research and development purposes is ruled mainly by three ordinances [1] collected in the Federal Law for Environmental Protection (LPE) [2]. Due to the possible risk of transmission of severe diseases when working with human tissue, this law imposes very strict and time consuming protocols concerning

---

[1]OPAM, Ordinance on the Protection against Major Accidents (`http://www.admin.ch/ch/f/rs/c814_012.html`); OUC, Ordinance on the Utilization of organisms in Confined environment (`http://www.admin.ch/ch/f/rs/c814_912.html`); OPTM, Ordinance on the Protection of Workers against Microorganisms related risks (`http://www.admin.ch/ch/f/rs/c814_312.html`)

[2]`http://www.admin.ch/ch/f/rs/c814_01.html`

storage, testing facilities and waste disposal.

Moreover, choosing human tissue would have been more restrictive in terms of selection of age, sex of the donor and type of tooth. The amount of tissue would have been also drastically lowered, compared to the tissue that can easily be obtained by choosing non-human tissue.

Also, when working in *in-vitro* conditions, the time between the death of the donor and the testing of its tissues is also an important issue that must be addressed. It was important to minimize this time as to prevent severe tissue degradation due to bacterial digestion. By using human tissues, this time was difficult to control for evident reasons. The use of animals instead, allowed for much better control.

At last, the knowhow acquired during past works, together with the already in place facilities for animal specimens extraction of our laboratory, brought to the final choice of **animal specimens** to be used for the experimental testing.

3.2.1 Choice of species

Human tissue having been discarded, it remained to decide which animal species suited at best the requirements of this study. According to the review given in section 1.4, rats, rabbits, monkeys, pigs and bovines were the most recurrent species used up to date for *in-vivo* and *in-vitro* experimental works on the PDL. Advantages and disadvantages in choosing these species are resumed in table 3.1.

In view of the reported positive and negative points, **bovine** was retained for this study. One may question the pertinence of taking cattle teeth into consideration, as cattle are herbivores (whereas humans are omnivores) and they chew almost continuously throughout the day on soft grass. Moreover, some of cattle's teeth are continuously erupting. That said, the work by Berkovitz [12] proved that no major physiological differences were present between the periodontium of the two species.

It should be mentioned at this point, that some restrictive protocols had to be followed due to safety issues related to the *bovine spongiform*

Table 3.1: Advantages and disadvantages for the choice of the species.

Species	Advantages	Disadvantages
Rat [26, 67, 74]	Most common animal used for PDL studies; Ease in their storage and breeding; Availability and high control on age and weight.	Very small and continuously erupting teeth (not the case for humans); Specimens extraction, handling and testing; Similarity with human PDL.
Monkey [101, 102, 161]	Species with the most human-like DNA.	Ethical issues and availability.
Pig [38, 76, 92]	Human-like PDL; Availability.	Somewhat small teeth.
Bovine [105, 125, 130]	Very large teeth; Ease in handling; Availability.	Herbivores; Continuously erupting; Continuous chewing; Width of the PDL twice the human's.

encephalopathy (BSE, or *mad cow disease*). In 1996 epidemiologists suggested that eating BSE-contamined beef could cause a new version of the Creutzfeld-Jacob disease (a human brain disease). This discovery was the cause of the introduction of strict safety protocols concerning bovine tissue handling. If aged of 30 or more months, abattoirs must keep the skulls of every killed bovine overnight. During this time, tests on the cattle's central nervous system are performed to certify that the animals were not infected by BSE. Only when proof that no suspicious prions were present in the cows was obtained, the meet could leave the slaughterhouse for the market. Accordingly, this procedure had to be respected. Thus, the specimens could not be obtained immediately after the animal's death, but only the day after. To slow down tissue

degradation, however, the entire skulls were left until tissue's excision in cold rooms at 0℃.

3.2.2   Choice of animal

Animals aged **between 3 and 6 years** were chosen.

The upper limit was established according to a veterinarian suggestion, so that the PDL and the teeth were still in good conditions. To make sure the animal was not older, an easy check based on dentition was done: mature bovines have, on the lower jaw (see also figure 3.1), 3 pairs of permanent incisors (the central, the middle and the lateral paris) which completely replace the deciduous (baby) teeth once the animal approaches 4 years of age. From then on, almost continuous chewing induces wearing of the incisors, starting from the central towards the lateral ones. The noticeable wearing on the middle incisors (the second pair) is a clear indicator that the animal reached his 6th year of age. Thus, selected mandibles should show wearing on the central incisors at most.

As mentioned above, bovines posses deciduous teeth, which, in their adult age, are substituted by permanent teeth. Our concern was to test completely mature bovine's teeth to ensure steady conditions for all the specimens. Therefore, depending on the chosen tooth, a different minimal age was required, since permanent incisors erupt from 1.5 (central) to 4 (lateral pairs) years, whereas permanent molars from 0.5 (for the 1st molar) to 2.5 (for the 3rd molar) years. Excluding the lateral pair of incisors as possible candidates for this study, as they are too small, a minimal age of 3 years was required. A good indicator that established whether the animal reached that age, was the full eruption of its 3rd molar.

Eventually, in general the mandible should look in good conditions, not broken and with a healthy dentitions.

3.2.3 Choice of tooth

Cattle's upper (maxilla) and lower (mandible) jaws present different dentition patterns; the maxilla do not show incisors, only appearing in the mandible in 4 pairs. Beside that, they both show 3 pairs of molars and 3 pairs of premolars.

According to previous studies [64, 123], incisors were discarded and the **mandibular 1st molar** was retained as tooth of interest due to the following reasons.

- Incisors have a really broad PDL and their mobility into the bony sockets is too wide compared to what observed in humans. Moreover, their roots are short, making difficult the extraction of good quality samples.

- As is the case for incisors, premolars —which size is comparable to human's molars— have short roots. Furthermore, their shape is not consistent between animals.

- Among the 3 pairs of molars, the first to erupt are the 1st molars. These teeth in all bovines, except in rare circumstances, have two well defined roots with no deformities: one distal root (towards the back of the mouth) and one mesial root (towards the front of the mouth). This is not the case for the 2nd and the 3rd molars which can both develop anywhere between two to five different roots.

- Eventually, the mandible was easily handled, transported and cleaned from all the surrounding soft tissues than the maxilla.

3.3 Preliminary steps for specimens extraction

Whichever type of specimen (i.e., assigned to histological investigation or suitable for mechanical testing) had to be extracted, the subsequent protocol was followed to isolate the 1st lower molars from the rest of

the mandible.

After the mandible was withdrawn from the local slaughterhouse (Vuillamy-Bell, Cheseaux-sur-Lausanne, Switzerland), the dissection of the regions of interest (i.e., left and right 1st molar blocks, containing 1st molar teeth and as much as possible surrounding alveolar bone) from the rest of the mandible was performed. The sequence of the cutting is shown in figure 3.1.

With the help of a scalpel, the remaining traces of soft tissues (i.e., skin, mussels and gingiva) that were still attached to the jaw had to be removed in the laboratory (École Polytechnique Fédérale de Lausanne EPFL, LMAF, Switzerland) before cutting.

Using a heavy industrial band saw (Magnum Bs0633, Metabo, Nürtingen Germany) a first cut was done between the 1st and 2nd premolar teeth (cut 1 in figure 3.1) to divide the mandible into left and right sides.

Further sectioning was done to isolate the molar blocks. In order to preserve the 1st molar (M1, in figure 3.1) and its surrounding PDL and alveolar bone, cuts along the long axes of the 2nd molar (cuts 2) and 3rd premolar (cuts 3) were made far from the site of interest to avoid for unwanted sectioning and excessive heating of the tissues. A 4th cut was also carried out to reduce the size of the block and to allow for its comfortable gripping into custom-made chucks for further sectioning. Finally, the crowns were cut away approximately at the alveolar crest (cut 5) and discarded.

At this stage, depending on the type of specimen required, the protocols described in sections 3.4.2 or 3.5.1 were followed.

3.4 Histo-morphology

A basic knowledge of the anatomy and histology of the periodontium was a prerequisite for a better understanding of the phenomena involved in its mechanical behavior. Concerning bovine tissue, however, there
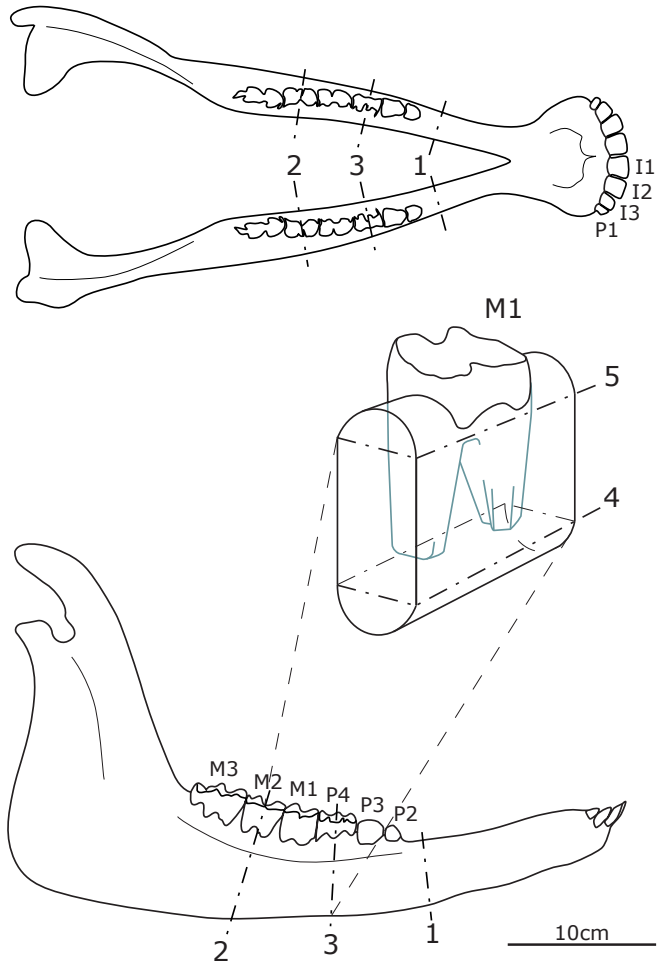
Figure 3.1: Schematic showing upper and lateral views of a bovine mandible. Sequential cuts 1–5 were performed for the obtaining of the 1st molar block (in the centre). M1–M4: molars 1–4; P1–P4: premolars 1–4; I1–I3: Incisors 1–3 [64].

is an almost complete lack of available information, the only study illustrating structural aspects of bovine PDL being the one by Berkovitz [12].

Assessment of anatomical and histological aspects affecting the mechanical behavior of the PDL was therefore essential.

3.4.1 Some terminology

In anatomy, specific terminology is used to define the positioning of body parts with respect to some reference point. For the reader to be able to locate the specimen origin within the mouth [5], the recurrent terms used along this work and their definitions are reported in table 3.2 (see also figure 3.5).

Table 3.2: Definition of spatial locations.

Term	description
Mesial	refers to the direction toward the anterior midline in a dental arch, as opposed to *distal*. Each tooth can be described as having a mesial surface
Distal	refers to the direction towards the last tooth of a dental arch, as opposed to *mesial*. Each tooth can be described as having a distal surface
Lingual	refers to the side of a tooth adjacent to (or toward) the tongue, as opposed to *buccal*
Buccal	refers to the side of a tooth that is adjacent to (or toward) the inside of the cheek, as opposed to *lingual*
Coronal	refers to the direction towards the crown of a tooth, as opposed to *apical*
Apical	refers to the direction towards the root tip(s) of a tooth, as opposed to *coronal*

3.4.2 Specimen preparation for histological investigation

In performing histological studies, it is of paramount importance that the selected sample be as fresh as possible. Post-mortem degradation, in fact, rapidly affects the tissue's biological aspects that histology is supposed to reveal.

It was therefore not possible to select the same animals as the ones chosen for the mechanical testing, due to the compulsory safety overnight stay of the animal's skulls at the slaughterhouse (see section 3.2.1). Bovine younger than 30 months, however, were not subjected to this restrictive norm and could be immediately retrieved after death.

Bovine mandibles of animals aged 2 years were obtained from another local slaughterhouse (Abattoirs de Clerens, Vevey, Switzerland), placed in ice cooler containers and brought within 30 minutes to the laboratory for subsequent sectioning. Their age guaranteed that the 1st molar tooth was completely erupted, maximizing thus the similarity with the teeth selected for the mechanical testing (see section 3.2.2). The steps described in section 3.3 were followed to obtain the preliminary 1st molar blocks from which the samples were subsequently extracted.

Each molar block was cut with the heavy industrial band saw to separate the mesial from the distal root. The obtained mesial and distal blocks were then mounted in a vice and further sectioned in 4 horizontal mini-blocks (a, b, c and d) of about 1cm thickness each (see figure 3.2). As they became available, the root sections were immediately dipped in room temperature fixative solution to stop natural tissue's degradation.

Further tissue processing was performed in the histology laboratory of the Department of Periodontology and Prosthodontics, School of Dental Medicine, University of Bern, Switzerland, where, as described in [19], two types of specimens were obtained for the histological investigation: the undecalcified ground sections and the decalcified semi-thin
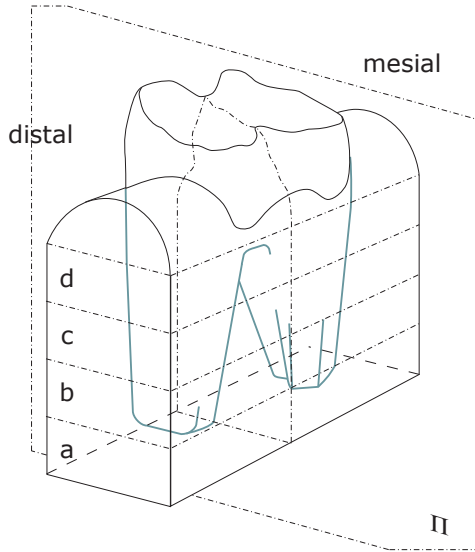
Figure 3.2: Schematic illustrating the obtaining of the specimens for histological studies. After separating the mesial from the distal root (cut Π), four mini-blocks (a, b, c and d) were cut.

sections.

Undecalcified ground sections

Tissue samples were fixed in 4% buffered formalin for 4 days, rinsed in running tap water, dehydrated in ascending concentrations of ethanol, and finally embedded in methylmethacrylate. The embedded tissue blocks were then horizontally cut into approximately 200μm-thick sections using a low-speed diamond saw (Varicut$^{®}$ VC-50, Leco, Munich, Germany). For the analyses, 4 sections per root, each one coming from a different root level, that did not include undesired artifacts as presence of enamel (most coronal sections) or too much irregular structures (most apical sections), were selected. Care was taken in selecting sections which were at about equal distance from one another. The

sections were grounded to a final thickness of about $100\mu m$, polished (Knot-Rotor-3, Struers, Rodovre–Copenhagen, Denmark) and surface stained with toluidine blue–McNeal after they had been mounted onto opaque (or transparent if assigned for the polarized light microscopy observation) acrylic glass slabs.

Decalcified semi-thin sections

Tissue samples were fixed for 72 hours in 1% glutaraldehyde and 1% (para)formaldheyde, buffered with 0.08M sodium cacodylate (pH 7.4). Following a brief wash in 0.1M sodium cacodylate buffer with 5% sucrose (pH 7.4), the tissue samples were exposed to a decalcifying solution containing 4.13% disodium ethylenediamine tetraacetic acid (EDTA). Decalcification was performed at 4℃ for 3 months. The solution was changed twice a week and continuously stirred.

The bloks were then sectioned with a razor blade into approximately 50 slices per tooth in a corono-apical and bucco-lingual direction. Following extensive washes in buffer solution, 10 slices were processed for tissue maceration in 10% NaOH solution, under constant 4 days lasting stirring (the solution was daily changed) and at room temperature. This procedure removed cells and non-collageneous extracellular matrix constituents but preserved collagen structure and position [77,81]. Both macerated and non-macerated slices were dehydrated in increasing concentration of ethanol and embedded in LR white resin (Fluka, Buchs, Switzerland).

Semi-thin sections of $1\mu m$ thickness were prepared using glass and diamond knives (Diatome, Buchs, Switzerland) on a Reichter Ultracut E microtome (Leica Microsystems, Glattbrugg, Switzerland), stained with toluidine blue and observed in a Leica Dialux 22 EB microscope.

3.4.3 Histometric measurements

Blood vessels

The histological slides were analyzed in a light microscope (AX70, Olympus Corporation, Japan) at 10X magnification. All around the roots and for all the root levels (a, b, c, d), a set of pictures (depending on the width and morphology of the PDL) was taken in digital format (640 x 512 pixels) to cover the PDL region. Overlapping pictures of the total PDL surface were produced. Using a commercial imaging software (Adobe™ Photoshop™, Adobe Systems Incorporated, USA), the images obtained were then assembled to picture the entire contour of the PDL (refer to figure 4.1 on page 98).

Next, all visible blood vessels (no less than 6 pixel in diameter) were filled with a white background color to allow their detection in the subsequent automated steps. The resulting images with white-filled blood vessels were then processed with a custom-made routine (LabView, National Instruments, USA). After the operator had manually selected the PDL area between the alveolar bone and the root surface as the region of interest (ROI), using threshold-based routines, the software calculated both ROI's and total blood vessels surfaces. With the aid of a standard gauge, the program eventually provided the PDL and the blood vessel areas in mm^2, the blood vessel area fraction (percent of blood vessel total surface vs. PDL surface), the number of blood vessels contained in the ROI and their numerical density (number of blood vessels / PDL area [mm^{-2}]).

Eventually, the diameters of all the blood vessels were measured. Since the cross-sections of the blood vessels did not often appeared as perfectly circular, but mostly as elliptical (due to the fact that many blood vessels were not exactly normally oriented with respect to the transverse cut), it was decided to consider the ellipses short axes as the real blood vessels diameter.

PDL width

The PDL width was assessed for each root level (a, b, c, d). Using the graphics software, a line was drawn through the central zone of the periodontal ligament. The PDL total surface calculated during the blood vessel measurements was then divided by the line length to yield the PDL width.

Bone- and cementum-PDL interfaces

It has been noticed [19, 123] that the bone-PDL interface is usually much more tortuous than the PDL-cementum one. To measure and quantify this winding, the fractal dimensions of both interfaces was assessed [18, 66]. Briefly, the real length L of a curved segment can be considered as

$$L = \lim_{\epsilon \to 0} L(\epsilon) \tag{3.1}$$

where $L(\epsilon)$ is the measured length of the curve obtained with the measuring gauge ϵ. $L(\epsilon)$ can be thus experimentally determined by fitting a series of measuring gauges along the curve

$$L(\epsilon) = \epsilon N(\epsilon) \tag{3.2}$$

where $N(\epsilon)$ is the number of times that the unit ϵ fits into the curve.

It has been empirically determined [18] that the number $N(\epsilon)$ depends on ϵ via the exponential relationship

$$N(\epsilon) = K\epsilon^{-D} \tag{3.3}$$

where K and D are constants dependent on the line's morphology. In particular D is referred to as the *fractal dimension* of the curve. Its value is bounded between 1 and 2, the lower limit representing smoothness and the upper limit severe roughness, and can be assessed in the following way:

By injecting the equation 3.3 in 3.2, the measured length $L(\epsilon)$ can be expressed as

$$L(\epsilon) = K\epsilon^{1-D} \tag{3.4}$$

which, on a log-log scale, can be rewritten

$$\log L(\epsilon) = \log K + (1 - D)\log(\epsilon) \tag{3.5}$$

so that $1 - D$ is given by the slope of the fitting line of the plot of $L(\epsilon)$ versus ϵ on log-log axes.

In the present study ϵ was taken equal to 1, 1/3, 1/9 and 1/27. These unit gauges were manually fitted to the intricacies of the bone and cementum boundaries. The number of times $N(\epsilon)$ that the gauge fitted the curve was recorded. The scalar dimension D could then be evaluated from the log-log plots of $L(\epsilon)$ versus ϵ.

3.5 Specimen preparation for mechanical testing

Two kinds of periodontal specimens, with different geometries, were extracted to allow for mechanical testing at various loading configurations. *Flat* and *cylindrical* uniaxial specimens (figure 3.3(a) and 3.3(b), respectively) were extracted following the protocols reported in section 3.5.1. The required labeling, cementing and gauging are presented in sections 3.5.2, 3.5.3 and 3.5.4, respectively.

3.5.1 Extracting specimens

Cutting of flat specimens

After the obtaining of the 1$^{\text{st}}$ molar block (see section 3.3), transverse sections (i.e., slices perpendicular to the tooth long axis, see also figure 1.6b) were cut with the aid of a custom-made chuck grafted onto a precision cutting system (Exakt, Germany). The use of a 0.3 mm diamond coated band saw and of a positioning system with a resolution of $\pm 20 \mu m$, ensured a precise control of the thickness of the sections, which werecut at low feed force (50g) under abundant normal saline solution (9% g/l NaCl de-ionized water) irrigation.

flat specimen · cylindrical specimen

bone

PDL

l

t

cementum-dentin

b

d

l_{bone}

l_{cem}

(a) (b)
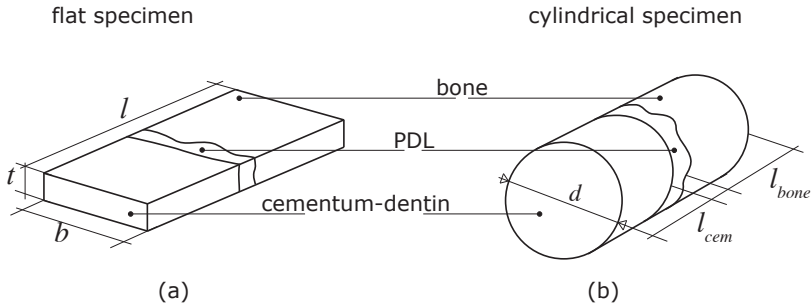
Figure 3.3: Schematics of the two specimen geometries; flat (a) and cylindrical (b) specimens. $l \approx 8$mm: total length; $l_{bone} \approx 3$mm: length of bone part; $l_{cem} \approx 2$mm: length of cemento-dentin part; $t \approx 2$mm: thickness; $b \approx 5$mm: breadth; $d \approx 6$mm: diameter.

Initial cuts were made in order to find where the 1st molar split into the two distinct mesial and distal roots. Starting from this point —called *the apex*— down, cuts were regularly placed every 2mm; the resulting 5 to 6 useful sections were labeled, gauged and stored at -21℃ until the day of testing.

The methodology developed in this work was such that all the specimens underwent to a unique freezing-thawing process at most before mechanical testing. Storage, in fact, is a crucial step in preparing biological *in-vitro* samples as multiple freezing-thawing cycles are known to reduce the mechanical properties of the excised tissues [116].

Note: Cutting transverse sections was a time consuming task and approximately 2 hours were needed to complete the sectioning of one tooth. Thus, while a block was being processed, the other one was kept into saline solution at 5℃to minimize tissue degradation.

On the day of mechanical testing, the previously frozen transverse sections were thawed at room temperature, photographed and fixed

onto a custom-made shape guide mounted on the precision band saw. Before proceeding to ulterior cutting the best locations for the flat specimens to be extracted from were selected on the basis of the following criteria:

- The specimen had to contain all of the three tissues involved in dental mobility (i.e., alveolar bone, PDL and dentin), the bone and dentin parts allowing for the gripping of the specimen to the testing machine.

- The layer of PDL within the extracted specimen had to be as planar as possible and perpendicular to the long axis of the specimen itself.

These two criteria implied that the flat specimens could not be extracted from the region within the two roots, where the PDL presented highly irregular shape and the alveolar process was too porous to allow for an appropriate gripping of the specimen. Furthermore, due to geometrical constraints, a breadth of at most $b = 5$mm was obtained. Figure 3.4 shows the resulting candidate sites for the extraction and their corresponding labels (see section 3.5.2).

Depending on the sample, 4 to 6 flat specimens were extracted from each transverse section. As it became available, each specimen was labeled, placed in a saline filled vial and stored at 5℃ until testing.

Cutting of cylindrical specimens

After that the crown was discarded (above level A in figure 3.5), the 1$^{\text{st}}$ molar block was taken off the chuck and its upper surface, showing the distal and mesial roots, drawn in a schematic sketch for the planning of the ideal extraction sites.

As in the case of the flat specimens, the cylindrical ones had to fulfill the same criteria for PDL layer (i.e., planar and normally oriented to the specimen's vertical axis). Guaranteeing such requirements for this kind of specimen was, however, more complicated, since for the extraction
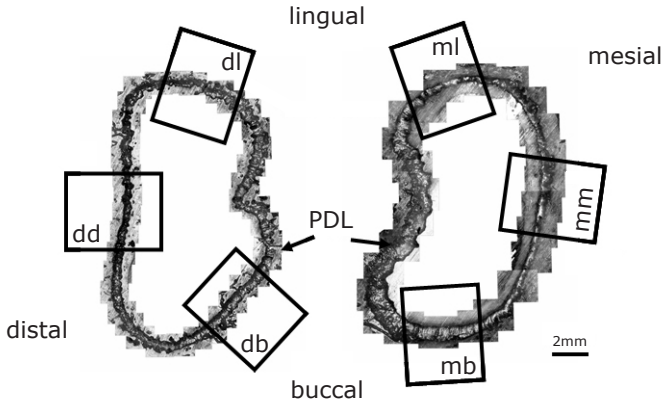
Figure 3.4: Ideal extraction sites, with corresponding label, for the flat specimens shown on a transverse section. m: mesial; d: distal; l: lingual; b: buccal.

the use of a drilling machine equipped with a trephine was needed. This tool, together with the morphology of the molar's roots, prevented, in fact, the operator for a visual control at the extraction site. Thus, only a comprehensive understanding of the roots morphology, together with accumulated experience, allowed for the obtaining of pertinent cylindrical specimens.

The molar block was held in place under the trephine by a vice allowing for the adjustment of five degrees of freedom (tree rotations and two translations in the horizontal plane). A steel wire (of 0.5mm in diameter) was then inserted into the pulp of the root of interest, giving a good indication on how the root was oriented into the bone. By adjusting the vice, then, the sample was accurately positioned so that the PDL was perpendicularly oriented to the trephine. Eventually, the specimen was extracted by moving the cutting tool downwards, with a fast and delicate jerky movement and under abundant saline irrigation.

Once the cylinder made of bone, PDL and dentin was obtained, its extremities were made planar and nearly perpendicular to the specimen long axis to allow for further cementing to the gripping system (sections
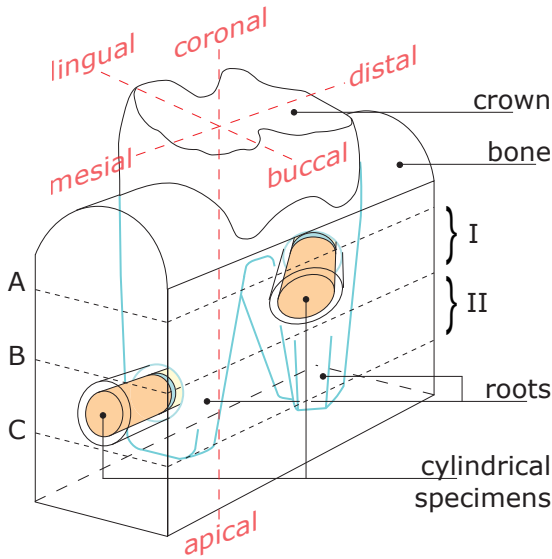
Figure 3.5: Schematic illustrating the extraction of cylindrical specimens. Specimens coming from distal root, buccal region, level I (dbI) and mesial root, mesial region, level II (mmII) are shown.

3.5.3 and 3.6).

A maximum of 6 cylindrical specimens, coming from the same locations than the flat ones (i.e., mb, mm, ml, dl, dd and db), were extracted from a first root depth level. The molar block was then put back onto the band saw and the already drilled part was discarded. Owing to the size of the extracting tool (of 6mm internal and 8mm external diameters), a maximum of two depth levels could be selected for specimens extraction. Depending on the sample, the same procedure was followed for the extraction of specimens from a second root depth level (between levels B and C in figure 3.5).

As it became available, each specimen was labeled (section 3.5.2), placed in hermetic vial and stored at -21℃ until the day of testing.

3.5.2 Labeling

Each animal was named by a capital letter (e.g., A, B, C, . . .). The letters L or R were added after the animal's name as to distinguish left from right molar (e.g., AL, AR). The following lower-case letters identified the root where the specimen came from —mesial (m) or distal (d) root— and its spatial location —mesial (m), distal (d), buccal (b) or lingual (l)— respectively (e.g., ALmb). Finally, roman numbers I to VI (to II in the case of cylindrical specimens) indicated the depth (from coronal to apical) from which the specimen was extracted (e.g., ALmbII).

3.5.3 Cementing

Cylindrical specimens, as opposed to the flat ones, which were mechanically clamped with some chucks, had to be glued to the gripping system designed for the mechanical tests (see section 3.6.2). This choice was made owing the testing conditions applied to this new specimen geometry. It was important in fact, to be able to seal the specimens from the surrounding environment by means of a thin-walled tubular rubbery membrane.

To glue the two hard tissues (i.e., bone and dentin) to the stainless steel specimen holders, a dental cement (Panavia™ F2.0, Kuraray Medical Incorporated, Japan) used for cementation of metal crowns and bridges was selected. This cement allowed for a really short curing time (3min) in a humid environment, very important conditions for the preservation of the mechanical properties of the PDL. Preliminary tests were also carried out to verify that this cement sustained the maximal stresses encountered during the tearing of the specimens.

On the day of testing, the cylindrical specimens were taken out of the refrigerator and left thawing at room temperature in normal saline solution, while the specimen holders were cleaned in an ultrasonic bath. Two rubbery o-rings and the tubular membrane were lodged into
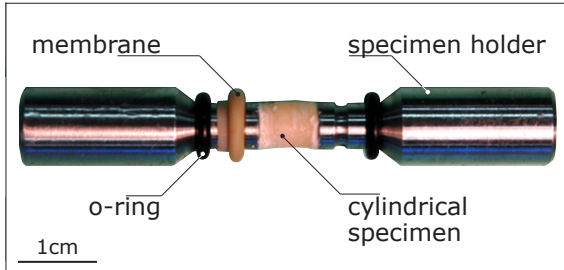
Figure 3.6: Cementing of cylindrical specimen on the specimen holders.

appropriate toroidal grooves machined onto the holders (see figure 3.6), while the tubular membrane was rolled up and wedged into its holding groove.

Before cementing, all the gluing interfaces (metal, bone and dentin) were treated, as specified by the cement's manufacturer, to improve bonding strength. A thin layer of cement was sufficient to ensure the gluing, which occurred after oxygen-free polymerization induced by an oxygen-blocking paste smeared above the cement. A custom made cementing gauge was used to guarantee the axial alignment of the specimen with the holders.

Once the curing was complete (in about 3 minutes), the holder-specimen-holder system, ready for gauging, was placed into a saline filled vial.

3.5.4 Gauging

Owing to variability within specimens, the PDL's width w_0 was measured for every specimen, to provide for an accurate estimation of the stretch ratio λ during the mechanical tests.

Flat specimens

Immediately after the cutting of the transverse sections, pictures of the whole PDL contour were taken at magnification 5X with an optical

microscope (Olympus AX70, Olympus Corporation, Japan). To cover all the perimeter, a series of overlapping pictures was taken and assembled afterwards with an imaging software (Adobe™ Photoshop™, Adobe Systems Incorporated, USA) as shown in figure 3.4.
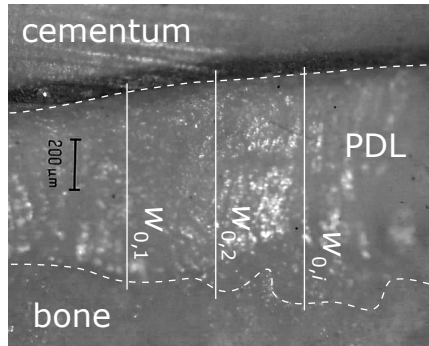
Figure 3.7: Measuring the PDL width.

Several measures of the PDL's width $w_{0,i}$ were then recorded from the selected sites (see figure 3.7) at equidistant intervals ($\sim$0.25mm) on a 5mm breadth. The average value w_0 was retained as the specimen PDL width.

After the flat specimens were cut out of the transverse sections, their external dimensions (breadth b, thickness t and length l, see figure 3.3(a)) were measured for the further calculation of stresses.

Cylindrical specimens

To guarantee good contour covering, images were taken each $\sim$30 degrees around the cylindrical specimen. Measurements ($w_{0,i}$) were made at $\sim$0.25mm intervals on every picture and the total mean (w_0) was calculated.

The diameter d and lengths l_{bone} and l_{cem} of the specimen (figure 3.3(b)) were also measured.

3.6 Testing devices

All of the mechanical tests performed in this study were carried out with the use of a commercial testing machine (Microtester 5848, Instron, Massachusetts, USA). With its characteristics (see appendix A for details), this machine was among the best commercial system for the purpose of soft biological tissues testing. High displacement resolution and very low force detection were the main assets of the Instron Microtester.

3.6.1 Flat specimens testing chamber

The flat specimens were tested with the facilities designed in the previous work by Sanctuary [123].

Briefly, the clamps of a custom-made gripping system were closed over the bone and dentin extremities of the flat specimens, leaving the PDL visible for observation. A saline bath was then raised to completely submerge the specimen.

3.6.2 Cylindrical specimens testing chamber

One of the main challenge in this work was the designing and the tuning of the device allowing for the testing of the periodontium in a controlled pressure chamber, the scope being the approaching of *in-vivo*–like conditions (multiaxial loading), by nevertheless keeping all the advantages of the *in-vitro* techniques.

Multiaxial loading of cylindrical specimens was obtained by applying simultaneously axial loading and lateral confinement. Such a testing configuration is often encountered in the field of geomechaincs were cylindrical soil specimens are extracted form the ground, wrapped in a tubular rubbery membrane (holding their watery content) and placed into a pressurized loading chamber. For the monitoring of the stress, a load cell is placed either outside or inside the pressurized chamber. Displacements are either recorded by the use of a linear variable differential transformer (LVDT), by optical methods or by strain gauges. In

addition, both specimen extremities are usually in contact with highly porous plates, usually connected to sensors measuring pressure and volume changes, allowing for the pore water to drain free during loading.

The major differences between these systems and the one designed here, resided in the geometrical dimensions and in the magnitude of the recorded quantities. Periodontal specimens dimensions were of about ten millimeters, and maximal loads of about a hundred Newtons, which were roughly a tenth and a hundredth of the typical dimensions and loads, respectively, encountered for the soil specimens.

The determination of the maximal pressure that the chamber had to face, was based on the following considerations. The masseter, the principal muscle involved in the masticatory process, is known as one of the strongest muscle in the body. Maximal biting force in human molars can thus reach peaks values as high as 1kN [46] (corresponding to 30MPa pressure on it's surface). However, depending on the foodstuff, physiological loadings are reported to be in the order of 100N [34], whereas orthodontic loadings range rather in the order of 1N [39].

Preliminary tests performed under the conditions specified in the following section (3.7), allowed for the determination of an average maximal uniaxial compressive load of -30N. The pressure chamber was then designed to be able to bear the equivalent pressure increase by a safety factor of 3.5, for a total of 4MPa.

The sketch in figure 3.8 shows the main technical aspects of the designed pressure chamber:

- Slender actuator bar (part 1 in the figure), allowing for the chamber cap to be raised enough to permit loading and handling of the specimen.

- Dynamic sealing joint (2), guaranteeing water tightness during high pressure dynamic tests.

- Air/Saline/Pressure in- and outlets (3,4,5), for the complete filling of the chamber with (pressurized) saline.

78

slender actuator bar (1)

air outlet (3)

dynamic sealing
joint (2)

upper grip (6)

upper spec. holder

specimen location

control viewport (9)

proximity bearing (8)

lower spec. holder

ø 80mm

lower grip (7)

saline

PMMA

saline inlet/outlet (4)

sub. load cell (10)

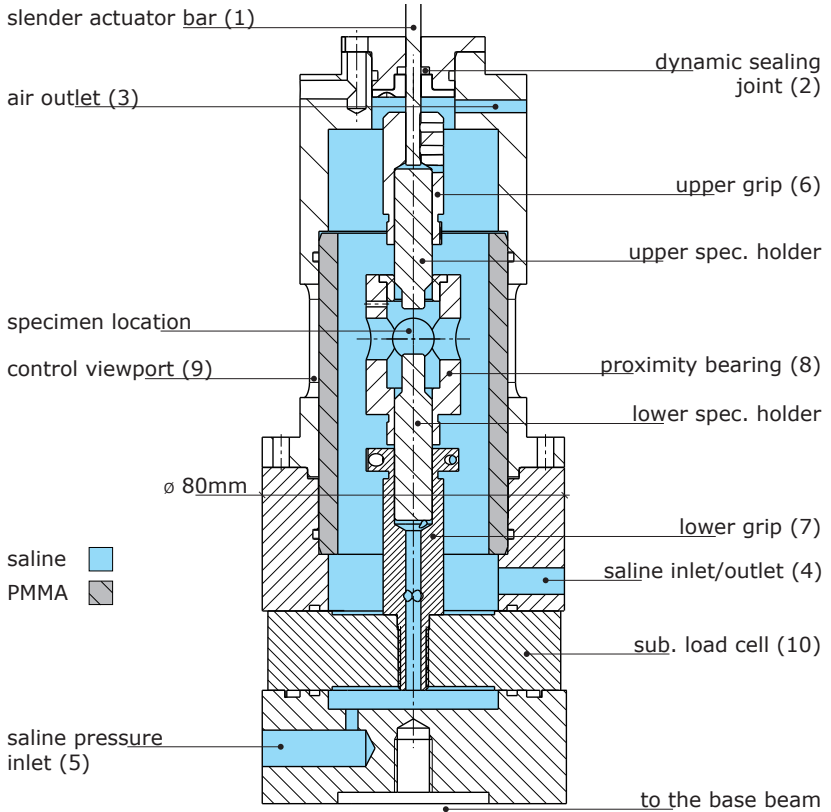saline pressure
inlet (5)

to the base beam

Figure 3.8: Design of the custom made pressure chamber (see text for explanation).

- Upper/Lower grips (6,7), where to tight the holder-specimen-holder system obtained after the cementing of the specimen (see figure 3.6).

- Proximity bearing (8), ensuring the pure axial loading of the specimen.

- Control viewport (9), for the visual monitoring and measuring of the specimen during the tests.

- Submersible load cell (10), to avoid recording of unstable parasite loads due to the dynamic sealing joint friction.

The proximity bearing (part 8) was introduced to prevent lateral bending of the slender actuator bar (part 1). This slight bending was, for time to time, generated during the compressive phase of the tests by the irregular morphology of the bone-PDL and/or cementum-PDL interfaces, which were occasionally slightly tilted with respect to the horizontal plane.

Visual monitoring of the specimen during the loading was ensured by 4 viewports (9) machined in the stainless steal chamber cap, where was lodged a transparent (PMMA) tube.

In the design of this pressure chamber, no possibility of controlling nor monitoring the pore water pressure was integrated. This aspect could be improved in further studies.

Compared to other possible designs (e.g., confinement of the specimen by a metal (porous) jacket), the solution adopted herein proved to be more flexible in the sense that allowed for the generation of a wide range of multiaxial loading paths. Also, the hydraulic resistance exercised by the surrounding fluid present in physiological conditions, as well as the fluid flows that could rise within the periodontium during mechanical loadings, were accounted for with this design. Eventually, parasite frictions between the confining system and the specimen was avoided.

The pressure pump

A commercial electromechanical pump (200cc/2MPa ADVDPC, GDS Instrument Ltd., UK) especially designed for geomechanical testing was chosen to control the pressure of the testing chamber.

The major concern for this choice was the ability of the pump to compensate for dynamic volume changes, induced by the up-down movement of the actuator bar (part 1) of the chamber room. The pump could make up for this inconvenience thanks to an integrated feedback control. Considering the worst case (incompressible specimen, maximal extension and speed), the highest volume change rate to compensate was in the order of $15\text{mm}^3/\text{s}$, which was largely below the pump capability (see appendix B).

The pump was filled with saline, which was pressurized by a piston moving in a cylinder and actuated by an electric step motor. The maximal reachable pressure (2MPa) well suited our requirements.

The load cell

The choice to use a submersible load cell (SLC), which could be dipped into the saline bath, was made after having experienced the difficulties in eliminating parasite loads introduced by the dynamic sealing joint's friction, which were sensed by the transducer when placed outside the pressurized chamber.

The sensitivity of the SLC to the environmental pressure was then evaluated. Figure 3.9 shows in fact that the recorded load F_{SLC} was dependent on the chamber pressure level p. However, pressurizing cycles between 0.0 and 1.0MPa (with pressure steps of 0.25MPa) showed the extremely high repeatability of this response and the absence of hysteresis. The induced load offset $F_{SLC}(p)$ could thus be easily subtracted from the recorded data, before their analysis.

Other technical specifications of the load cell can be found in appendix C.
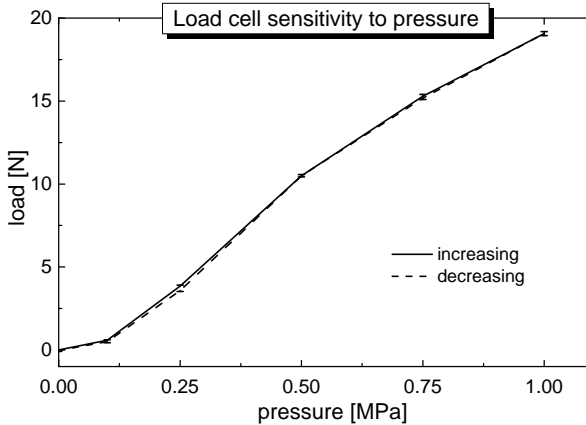
Figure 3.9: Sensitivity of the submersible load cell to environmental pressure. Mean curves obtained for increasing (solid) and decreasing (dotted line) pressures are shown with standard deviation bars.

3.7 Testing profiles

In this section are described the different loading profiles to which the two types of specimens were subjected.

As already mentioned, one of the goal of this work was the testing of *in-vitro* periodontal specimens in as much as possible *in-vivo*–like conditions.

Question raised then about what are the physiological conditions for the periodontium. Evidently, mastication is one of the natural loadings of this system. In humans, chewing pattern has been idealized to be of *teardrop* shape, with frequencies spanning form 49 to 120 cycles per minute [119]. Furthermore, experimental evidence [130] that the linear part (see figure 1.7) of the mechanical response of the PDL extends between $\lambda = 1.4$ to $\lambda = 1.6$, suggested the PDL to be able to sustain, without damage, a deformation corresponding to the $\pm 35\%$ of its

resting width w_0.

The vast majority of the mechanical tests performed in this work were thus carried out under the following general loading conditions:

- cyclic sinusoidal wave (simplifying the *teardrop* shape)

- 1Hz frequency.

- amplitude of $\pm 35\%$ of the resting PDL's width w_0

- 100% saline saturated environment

- room temperature.

Note: If not otherwise specified, these conditions were used in all tests and are identified in this text as *normal* loading profile.

In opposition to what has been done in the majority of the past studies on the PDL mechanical response, where attention was focussed on its tensile monotonic behavior (e.g., maximal tangent modulus, strength and strain at rupture, failure energy) [25, 71, 82, 105], major effort in this work was addressed to the cyclic tensile-compressive behavior, with special care to the compressive part of the response. In fact, as a consequence of its confinement in the alveolar socket, in the *in-vivo* displacement of a tooth, tension of the PDL at one side of the root leads inevitably to compression on the opposite side [130].

Moreover, sinusoidal strain histories probably provide the most complete input tests to characterize the PDL, both theoretically and experimentally, because they include other tests (such as relaxation) while being infinitely smooth in time and hence well-applicable [65]. Sinusoidal oscillations, scanning a frequency-spectrum, also provide more insight into the time dependent behavior of the mechanical response of the PDL.

3.7.1 Zeroing

A fundamental problem in testing *in-vitro* soft tissue specimens is represented by the definition of their *resting* (or *zero*) *state*, i.e., which geometrical configuration represents the zero displacement, thus zero load. Indeed, when pulling a soft tissue, its tensile response generally begins with a more or less large *zero region* (see figure 3.10), where no load response is recorded for a wide range of displacements. Only after a certain amount of stretch the collagen fibers start to align along a preferential direction (the loading one) and to bear a measurable load; this stage is known as the *toe region* and its beginning is usually defined as the *resting state*.

Results presented in this manner can be, however, misleading, especially when the specimen is to be tested both in tension and compression; in fact the *resting* configuration should be the one that separates the tissue's tensile from its compressive state.

It is well known that many soft tissues are in a pre-stressed state when they are in their physiological configuration; in fact, by excising specimens from such tissues, their dimensions reduce to reach a free stress state. For tissues like blood vessels [61], skin [150] or mesentery [49] however, the specimens dimensions can be easily recorded before excision, so that the physiological dimensions can be recovered and the physiological *zero state* be retrieved for the *in-vitro* specimens.

In the case of the extraction of PDL cylindrical specimens, such a procedure could not be used because of the impossibility to measure its physiological dimensions before the extraction. As a result, the methodology developed by Sanctuary [125] to define the *zero state* was adopted, so that all the specimens were into a common geometrical configuration prior testing. Figure 3.10 graphically shows how the *zero state* was established for each specimen after its mounting in the testing machine. Briefly, the position d_0 displayed by the displacement sensor after the specimen had been tightened to the loading machine was recorded. The specimen was then slowly pulled in tension to a load of $+5$N, and the corresponding displacement recorded as d_t. The load
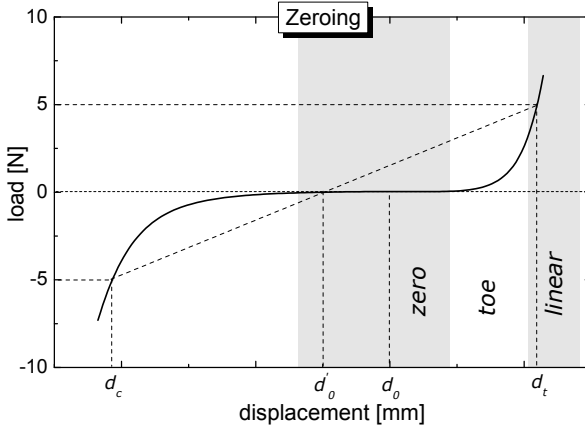
Figure 3.10: Defining the *zero state* of a PDL specimen for a tensile-compressive loading. A *zero* region followed by *toe* and *linear* regions are typical for soft tissue's tensile mechanical responses.

of -5N was subsequently reached by gently compress the specimen and the corresponding d_c annotated. The *zero position* d_0' was defined as the middle point between d_c and d_t and determined by

$$d_0' = \frac{d_t + d_c}{2} \tag{3.6}$$

3.7.2 Mechanical testing of flat specimens

Flat specimens were basically used to determine the dependance of the mechanical response of the periodontium on animal, tooth side, root, location and depth. Such investigation required a large number of specimens on which statistical analyses could be performed. It was necessary then to generate the largest specimen population relatively easily, and the methodology used to extract flat specimens (exposed in section 3.5.1) suited at best this purpose.

Preconditioning

As mentioned in section 1.5.1, to reach a steady response when cyclically tested, the tissues needed to be subjected to a certain number of cycles (see figure 1.8c on page 21) [50]. This characteristic was taken into consideration and the initial cycles of the sinusoidal tests (see below) were always discarded from any analysis of data.

Sinusoidal tests

Each specimen was subjected to a sinusoidal testing profile, involving 16 separate harmonic oscillations of 30 cycles each, at frequencies varying from 0.2 to 3Hz, with 0.2Hz increments, and at 4Hz.

Although several harmonic oscillations were recorded to obtain information on the mechanical response of the ligament at different strain rate excitations, the larger part of the results presented in this work was based on the analysis of the data obtained for the 1.0Hz sinusoidal loading.

Relaxation tests

Relaxation tests, besides enhancing viscoelastic characteristics of the PDL, allowed to check for the integrity of the tissue's mechanical properties after successive harmonic oscillations. Intermediate tensile and compressive step-relaxation strain tests were carried out at $\pm 35\%$ of w_0. Relaxation tests in tension were performed three times during the sinusoidal cycling: at the very beginning of the test, between the 2.0 and the 2.2Hz sinusoidal displacements, and at the end of the test. Compressive relaxations were instead performed twice: between the 1.0 and the 1.2Hz, and between the 3.0 and the 4.0Hz sinusoidal displacements.

The ligament was subjected to a rapid (3mm/s) strain step and held in this position until the its complete relaxation. The *zero state* was recovered afterwards.

Comparison of the sequential relaxation responses permitted to verify whether or not the tissue underwent significant damage.

3.7.3 Mechanical testing of cylindrical specimens

Cylindrical specimens were tested in a closed environment. The overall aim was to generate multiaxial loading conditions by simultaneously applying axial loading and lateral confining pressure to the specimens.

To achieve this task, several preliminary tests have been made to validate the pertinence of the testing methodology. These tests showed that comparing the responses of a set of specimens tested in certain conditions with *another* set of specimens tested in other conditions, would have made no sense because of the great variability of the mechanical responses observed between specimens tested in *same* conditions. This variability was due to factors such as the so-called *bio-variability*, accounting for *bio-* and *morpho*-logical inter-specimen differences, as well as to gauging and zeroing uncertainties. To establish the influence of a factor on the mechanical response of the periodontium, this factor was varied along the testing of each specimen for a set of, in general, 5 samples. For each specimen then, the variation of parameters describing the mechanical response was assessed as percent difference between the different testing conditions. The mean and standard deviation of the percent differences were then calculated for the set of samples. Due to the need of performing such such an *intra*-specimen analysis then, the experiments on cylindrical specimens required fairly long testing sequences.

Cylindrical specimens were tested in various loading and environmental conditions, allowing for the assessment of some of the characteristic mechanical features of the periodontium. Efforts were focussed on phenomena such as preconditioning, loading rate effects, compressibility and fluid phase contribution to the mechanical response.

Note: Not to affect the results, once the specimen was loaded in the testing device, it was removed *only* after the testing sequence was completed.

Long lasting cycling

To make sure that the tissue did not suffer any fatigue structural damage during long lasting tests, 2000 *normal* loading profile cycles (corresponding to 34min) were performed.

***Non*-mechanical degradation**

Tissue's degradation due to *non*-mechanical phenomena (e.g., natural post-mortem biological degradation) was assessed to evaluate its contribution to the possible variation of the PDL's mechanical response during long lasting testing. To this end, three sets of 40 *normal* loading profile cycles were performed at time intervals corresponding to the maximal testing duration of 30min. Evident changes in the mechanical response would have been a sign of tissue's degradation.

Effects of loading frequency

As it was for flat specimens, tests establishing for loading rate dependancy of the mechanical response were carried out for the cylindrical specimens.

After being preconditioned at 1.5Hz sinusoidal displacement (1000 cycles), load responses were recorded at the 100th cycles of each loading frequency $f = 1.5$, 1.0, 0.5 and 0.1Hz. The downward stepping frequency was the result of the two following considerations: first, the high frequency preconditioning allowed for the shorter time for this stage to be completed; second, chances of damage are likely to occur after long lasting cycling and at high frequencies. This problem was avoided by choosing to begin the test with the 1.5Hz and stepping back to the 0.1Hz excitation.

Optical monitoring and measurements

The custom-made pressure chamber designed for the testing of the cylindrical specimens present 4 see-through control viewports (see fig-

ure 3.8, part 9), allowing for visual feedback during testing. Important phenomena, as fluid exchanges, could thus be observed and recorded with the aid of a standard commercial digital camera (NV-DS990EG, Panasonic, Japan).

The lateral deformation of the PDL layer was also tracked via the recorded images. Synchronization with the axial displacement allowed the for the evaluation of an apparent tissue's Poisson's ratio.

Porosity of the PDL

The amount of pore volume within the PDL was assessed by weighting a blotting paper before (W_{paper}^{dry}) and after (W_{paper}^{wet}) it was used to blot the fluid content out of the PDL. The porosity n_{PDL} was calculated via the relation

$$n_{PDL} = \frac{V_{pores}}{V_0} = \frac{(W_{paper}^{wet} - W_{paper}^{dry})/\rho_{H_2O}}{V_0} \tag{3.7}$$

where V_0 is the volume of the PDL in its zero state (specimen's cross sectional area $\times$ w_0) and ρ_{H_2O} is the specific weight of water.

For the blotting procedure to be consistent among specimens, the samples were compressed with a force of -50N. The fluid spurting out of the specimen was then collected by the blotting paper, which was immediately weighted with a precision balance (PL200, Mettler-Toledo Inc., USA).

Permeability of the periodontium

Cylindrical specimens were also used to determine the permeability of the periodontal tissues.

Due to its structure however, the permeability of the PDL could not directly be measured and was left as parameter to be identified with a numerical model (refer to section 5.2).

Concerning the two hard tissues, disks of bone and cementum were obtained from cylindrical specimens by cutting the PDL layer with a

surgical knife. The two parts were subsequently reduced to ∼2mm thick cylinders by using the precision band saw. Attention was paid to that the original interface with the PDL was kept as one of the bases of the disk (see figure 3.11a).

Each disk was then loaded in the custom-made device shown in figure 3.11b, and a constant saline pressure gradient ΔP was applied

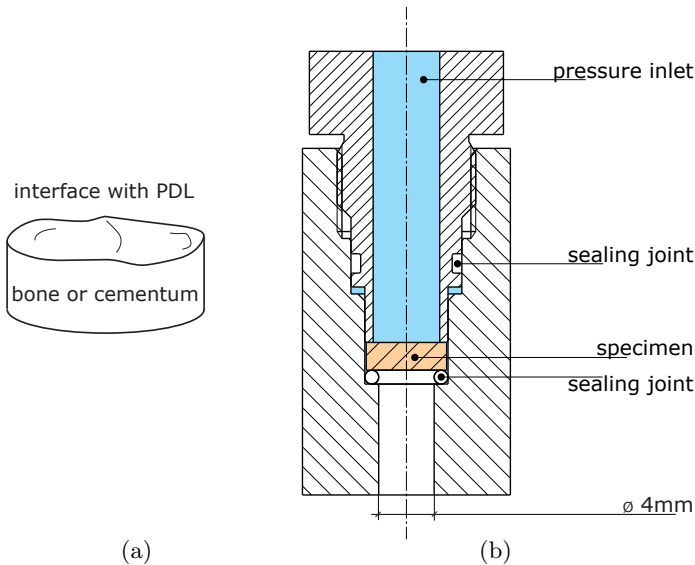Figure 3.11: Specimen (a) and device (b) used for the determination of bone and dentin permeabilities.

to it via the pressure pump. By measuring the volume of saline V_{sal} flowing through the specimen during a specific time Δt, the fluid flux Q (units of $[\frac{m^3}{s}]$) was determined as

$$Q = \frac{V_{sal}}{\Delta t} \tag{3.8}$$

The absolute permeability k $[\frac{m^4}{Ns}]$ was then obtained from Darcy's law

(see also section 2.3.1, page 47)

$$Q = k \frac{A \cdot \Delta P}{h} \tag{3.9}$$

where $A = 2\pi(d/2)^2$ and h were the active area ($d = 4mm$) and the height of the specimen, respectively.

Finally, the hydraulic conductivity k_s ($\frac{m}{s}$), related to k via the specific weight γ_w of the wetting fluid ($\gamma_w = 9965[\frac{N}{m^3}]$ for water at room temperature), was obtained by

$$k_s = k \cdot \gamma_w \tag{3.10}$$

Matrix and fluid contributions

A testing protocol was established to determine to what extent the fluid content contributed to the mechanical response of the periodontium.

Each specimen was tested with *normal* loading profiles in two different humidity conditions:

- **Saturated**: the specimen was entirely submerged in the saline bath during the cycling.

- **Blotted**: the saline bath was kept just below the specimen, the fluid content of which was blotted up (see below), prior sinusoidal testing.

After being tightened to the upper and lower grips (refer to figure 3.8) and *zeroed*, the specimen was subjected to a first relaxation test (rel_{01}) prior any preconditioning. The saline solution was subsequently raised to fill up the chamber and the *saturated* test was executed with a 1000 *normal* loading cycles. At the end of this step, a second relaxation test (rel_{02}) was performed only after the saline bath had been evacuated.

The chamber was opened and the PDL specimen was emptied of its fluid content. To make sure that the blotting procedure was consistent

along all the tested specimens, a compressive load of -50N was imposed to all of them, so that the pore fluid was squeeze out in a somehow equal manner. The out pouring fluid was collected with a blotting paper.

The chamber was closed and the saline solution was raised this time just below the lower end of the specimen. The 1000 *normal* loading cycles were then run a second time. Finally, a last relaxation test (rel_{03}) was performed.

Unjacked tests

Note: The term *unjacked* refers to the fact that the specimens were not sealed from the surrounding environment (i.e., the saline bath) during the testing procedure.

The testing procedure for the *unjacked* tests is resumed by table 3.3. After that the specimen was loaded in the pressure chamber and subjected to preconditioning at room pressure (i.e., 0.0MPa), 5 hydrostatic pressure levels were sequentially imposed to it. The pressure was increased while the specimen was continuously cycled (i.e., the sinusoidal excitation was uninterrupted until the end of the test). Due to the pump capabilities, however, the pressure increments took some time to take place (especially at low pressures). A 100 cycles transition period was thus left for the pressure to reach the desired level.

Table 3.3: Testing profile for *unjacked* tests.

Cycles	Pressure level	Transition cycles	Recorded cycles
1–1000	Prec.	-	1-**1000**
1001–1200	0.0MPa	1101–1200	1001–**1100**
1201–1400	0.1MPa	1301–1400	1201–**1300**
1401–1600	0.5MPa	1501–1600	1401–**1500**
1601–1800	1.0MPa	1701–1800	1601–**1700**
1801–2000	0.0MPa		1801–**2000**

Note: Boldfaced numbers in table 3.3 indicate the cycles which were

used for the comparison of the mechanical responses to the different pressure levels.

Jacked tests

Note: The term *jacked* refers to the fact that here the specimens were wrapped in a rubbery tubular membrane (6mm in diameter, 0.2mm wall thickness, Piercan, Paris, France) and sealed from the surrounding environment (i.e., the saline bath) during the testing procedure.

The multiaxial loading of the periodontium was obtained by simultaneous application of axial displacement and lateral pressure. Several preliminary tests led to the following testing protocol, which allowed for the analysis of the combined effects of lateral pressure *and* initial level of saturation of the PDL.

The holder-specimen-holder system was loaded in the pressure chamber, at room pressure (0.0MPa), with the tubular membrane rolled-up on its groove. After *zeroing*, a 1000 *normal* loading cycles were performed in a fully saturated saline environment to precondition the specimen. The sample was subsequently tested with 3 level of pore saturation:

- **Over-saturated**: the specimen was held in its maximal stretched position (i.e., at $\lambda = 1.35$) while the surrounding saline was allowed to completely fill the pore volume of the PDL during 5 minutes. The saline was then evacuated from the testing room and the chamber opened for manipulation. The membrane, rolled-up on the lower specimen holder, was carefully raised over the specimen and the two o-rings (refer to figure 3.6) were placed over it, ensuring complete sealing of the specimen from the environment. Only at this stage, the stretch on the specimen was released to retrieve the *zero state* (e.g., $\lambda = 1.0$). The term *over-saturated* designates then the fact that, in the *zero state*, there was more water than needed to totally fill the pore volume of the solid matrix. The chamber was closed, and the saline bath raised again

to fill the testing room. Loading involved now 5 series of 200 sine cycles each (for a total of 1000 cycles) upon which the chamber pressure was varied as shown in table 3.4 (boldfaced numbers indicate the cycles used in the analysis of the data).

Table 3.4: Testing profile for *jacked* tests.

Cycles	Pressure level	Transition cycles	Recorded cycles
1–200	Prec.	-	1-**200**
201–400	0.0MPa	301–400	201–**300**
401–600	0.1MPa	501–600	401–**500**
601–800	0.5MPa	701–800	601–**700**
801–1000	1.0MPa		801–**900**

- ***Saturated***: After the *over-saturated* test, the specimen was held in its *zero state* (i.e., at $\lambda = 1.0$), the saline solution was then evacuated from the testing room, the chamber opened and the membrane rolled back onto its groove. Both the specimen and the membrane surfaces were carefully dried before the sealing system (membrane and o-rings) was repositioned, so that the pore volume of the solid matrix was, this time, completely filled with saline when it was in its *zero state*. The test sequence reported in table 3.4 was run a second time on the same specimen.

- ***Partially-saturated***: A third initial level of saturation of the PDL was finally tested. The same procedure described for the *saturated* test was followed, but the fact that the specimen was held in its minimal stretched position (i.e., $\lambda = 0.65$) for the complete filling of the pore volume[3]. Evidently, after the sealing system was repositioned and prior cycling, the specimen was brought to the *zero state* (i.e., $\lambda = 1.0$).

---

[3]In this context, thus, the term *partially* does not mean that a portion of the pore volume contained a gas phase.

Chapter 4
Experimental Results

> *However beautiful the strategy, you should occasionally look at the results.*

> Winston Churchill, 1874–1965

All the main experimental results obtained from histo-morphological investigation (in section 4.2) and mechanical testing (section 4.3 for flat and 4.4 for cylindrical specimens) on the periodontal tissues are reported in this chapter. Analysis of data was performed using the methodology exposed in section 4.1.

4.1 Analysis of experimental data

4.1.1 Statistical analysis

One-way analysis of variance (ANOVA) was used to examine whether or not eventual differences were statistically significant among several (more than two) specimen groups. When significant differences were encountered, ANOVA was followed by Scheffé's test to obtain paired comparison, allowing to tell between which among the groups the differences were statistically relevant. When the comparison had to be done between *only two* groups, a pairwise Student's t-test was used instead.

In all statistical analyses, the confidence interval was set at 95% and the parameter for the comparison was $P = 0.05$. When significant

difference at 95% confidence level appeared (marked in the graphs with $*$), it was also tested for more restrictive confidence intervals (99%, $P = 0.01, **$ and 99.9%, $P = 0.001, ***$).

4.1.2 *Intra-specimen* analysis

Since the mechanical response of the periodontium widely varied among specimens due to the already mentioned *bio-variability* (see section 3.7.3), comparing the responses of a set of specimens tested in certain conditions with *another* set of specimens tested in other conditions, would have made no sense. Thus, *intra-specimen* comparisons were performed.

To establish the influence of a factor on the mechanical response of the periodontium, this factor was varied along the testing of each specimen for a set of, in general, 5 samples. For each specimen then, the variation of parameters describing the mechanical response was assessed as percent difference between the different testing conditions. The mean and standard deviation of the percent differences were then calculated for the set of samples.

The data reported in tables 4.6–4.8 and 4.13–4.18 were obtained from such an analysis.

4.2 Histo-morphology

The results obtained from the histo-morphological observation were carried out in collaboration with Dr. D. Bosshardt (Department of Periodontology and Prosthodontics, School of Dental Medicine, University of Bern), Mrs. G. Vaglio and Dr. A. Wiskott (Section de Médecine Dentaire, Faculté de Médecine, Université de Genève) and are extensively detailed in [19] and [147].

The histo-morphological findings relevant to the understanding of the PDL's mechanical functioning are given in the following sections.

4.2.1 Blood vessels

Thirty-two undecalcified ground sections obtained from 2 animals (A and B) furnished a total of 95 specimens for which the blood vessel's area fraction, number, numerical density and diameter were assessed as specified in section 3.4.3. Every specimen came from one among the 6 suitable regions for mechanical testing (i.e., db, dd, dl, ml, mm and mb).

The steps through which the images of the ground sections of the periodontium were processed are shown in figure 4.1. After assembling the different images taken from a same region (in figure 4.1a only 3 images among the usual 7 that were necessary to cover the entire specimen's breadth –5mm– are shown), the blood vessels were filled with a white background as to facilitate further automatic detection (4.1b). To allow for density calculation then, the PDL area was manually selected as region of interest (ROI, darker area in figure 4.1c).

Densities

General means and standard deviations (over the 95 specimens) of the different density values are reported in table 4.1.

Table 4.1: PDL area and blood vessel densities.

PDL area [mm^2]	BV area [mm^2]	BV area fraction [%]	BV number [#]	Numerical density [#/mm^2]
2.44±0.51	0.42±0.16	**17.58±6.49**	100±23	41.79±10.07

Almost the 20% of the PDL space was occupied by the vascular system. Despite possible *intra*-spices and regional dependencies of the blood vessel density [19, 147], the most important observation from a mechanical standpoint is the fact that, compared to other fibrous connective tissues, the PDL vascular system resulted to be highly developed [48]. It has been suggested [85] that the vascular system plays an
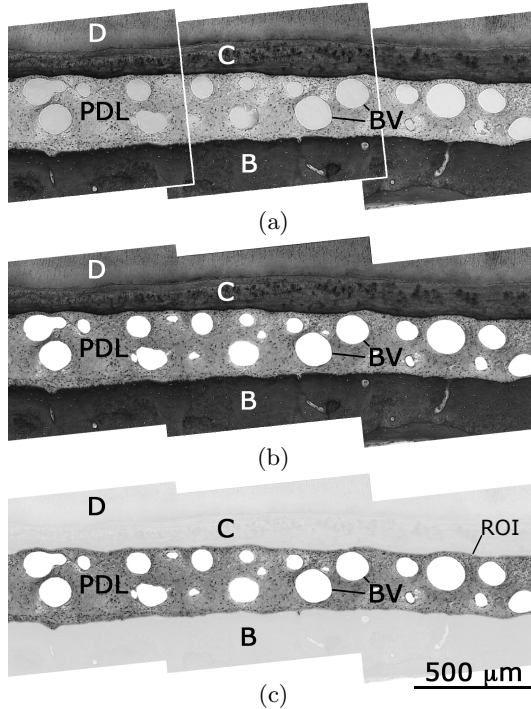
Figure 4.1: Procedure for blood vessel detection: assembling of the images (a); filling of the BV with white background (b); selection of the ROI (c). D = Dentin, C = Cementum, PDL = Periodontal Ligament, BV = Blood Vessel, B = Bone.

important role in shock absorption during mastication impacts. This issue will be addressed in more details in section 4.4.8.

The blood vessel area fraction obtained was in line with what reported in the literature; the wide spread of the values retrieved (from 4 to 47% of the PDL space [17, 132]) was justified by the fact that, as reported in [147], this parameter was dependent on animal ($P = 0.007$), root depth ($P = 0.003$) and location ($P = 0.01$).

Diameters

As blood vessels probably represent the main contribution to the total porosity of the PDL, their geometry likely have an influence on its mechanical behavior. In fact, as shown by the Kozeny-Carman equation 2.42, the permeability of a material depends also on the specific area S_0 of the pores per unit volume of solid matrix.

From the total of the analyzed specimens, coming from animals A and B, the diameters spanned form 8 (the smallest detectable vessel) to 463μm, with the median value at $\bar{d}_{BV} = 43\mu$m.

With respect to their spatial distribution, no general trends could be identified as their distributions was not consistent among teeth, root depth or location.

4.2.2 PDL width

The PDL area obtained from the previous definition of the ROI (see figure 4.1c) allowed also for the calculation of the mean PDL width w_0 for every specimen, obtained by

$$w_0 = \frac{PDL\ area}{image\ length} \qquad (4.1)$$

where *image length* was the length of the line drawn on the PDL images and which was approximatively equidistant from the bone and the cementum surfaces.

The average over the whole specimen population gave a mean value of

$$w_0 = 551 \pm 125\ \mu\text{m}. \qquad (4.2)$$

As detailed in the work by Vaglio [147], this quantity appeared to be animal and root depth dependent ($P = 0.03$).

Note that, when compared to human PDL width, which is in the order of 100–300μm [30, 128], bovine PDL is wider by about 2 times.

4.2.3   Bone- and cementum-PDL interfaces

Qualitative assessment of both bone-PDL and cementum-PDL inter-
faces suggested a more marked roughness of the former for the vast
majority of the analyzed locations (see figure 4.2). When compared
to humans, the bony socket of the bovine mandibular 1st molar de-
noted a high remodeling activity. This could be explained by the fact
that, in opposition to humans, bovines are ruminant herbivores with
extreme horizontal tooth movements during mastication and that their
mandibular 1st molars are continuously erupting teeth, processes which
both highly promote remodeling activity [1, 154].

For a quantitative assessment of the PDL boundaries, the fractal
dimensions D of the bone- and cementum-PDL interfaces were obtained
as described in section 3.4.3 for the usual six locations. A total of 22
specimens were measured, and the values reported in table 4.2 obtained.

Table 4.2: Fractal dimensions D for bone and cementum at the 6 usual locations.

location (# of spec.)	Cementum - PDL D	Bone - PDL D
mb (4)	1.01±0.01	1.04±0.01
mm (2)	1.01±0.02	1.14±0.04
ml (4)	1.05±0.02	1.07±0.04
dl (4)	1.10±0.05	**1.22±0.08**
dd (4)	1.09±0.06	1.06±0.03
db (4)	1.08±0.05	**1.18±0.05**
means	1.06±0.05	1.19±0.08

The general means of bone-PDL and cementum-PDL fractal di-
mensions confirmed the qualitative observation that alveolar bone was
subjected to higher remodeling activity than cementum. Except for
location dd (see table 4.2), this was also the case for every location
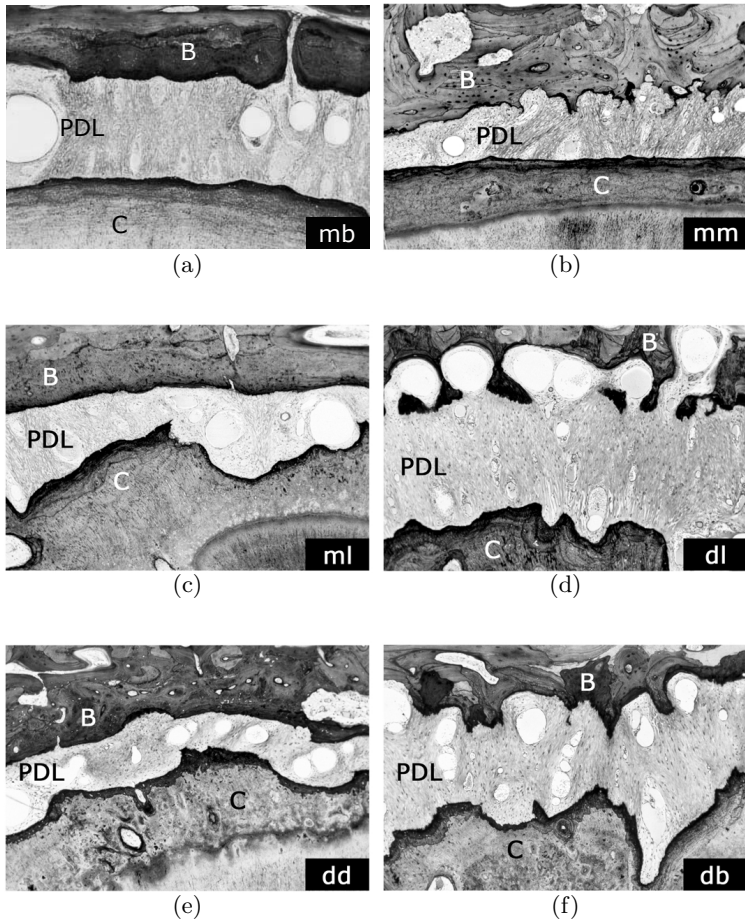considered.

Figure 4.2: Typical periodontium morphology of the usual mb (a), mm (b), ml (c), dl (d), dd (e) and db (f) regions. C = Cementum, PDL = Periodontal ligament, B = Bone.

Moreover, within the bone-PDL interfaces, the regions that showed the highest fractal dimensions were dl and db (in **bold** in the table). In a recent work [154] it has been proved that mechanical loading produces an increase of the bone-PDL interface fractal dimension. As a conclusion it was suggested that the distal root of the first mandibular molar was particularly subjected to bucco-lingual excitations, result which was actually in total agreement with the physiological masticatory pattern of the bovine.

4.2.4 Collagen fibers

Collagen fibers are the PDL constituent which mainly support, at least in tension, mechanical loadings. From a mechanical standpoint, it is thus essential to know how they link bone to cementum and how dense is the mesh they generate, in order to better understand the mechanisms underlying the mechanics of the PDL.

Qualitative assessment of such characteristics were obtained by polarized light microscopy on undecalcified ground sections (see figure 4.3, from [19], with permission). It was observed that both fiber orienta-

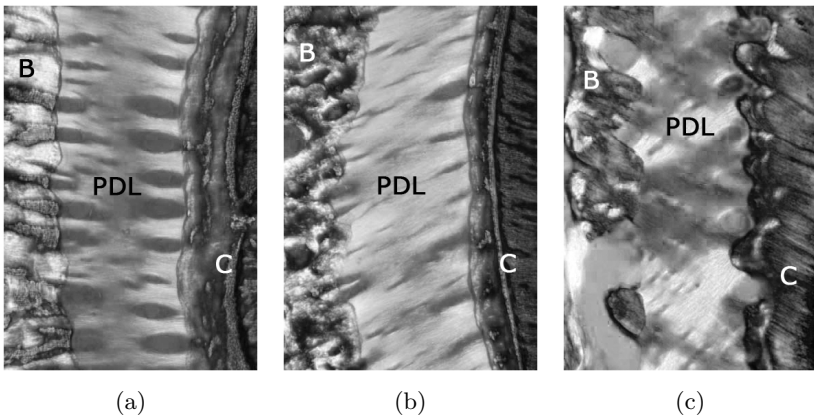(a)   (b)   (c)

Figure 4.3: Collagen fibers orientation: perpendicular (a), oblique (b) and crisscross (c) patterns. C = Cementum, PDL = Periodontal Ligament, B = Bone.

tion and density greatly varied among locations and root depths. In general, sections coming from coronal portions (figures 4.3a and 4.3b) were densely packed and showed a marked degree of orientation than specimens obtained at apical levels (figure 4.3c).

4.2.5 Summary

All the observation exposed in this section supported findings reported in previous works.

Qualitative and quantitative descriptions indicated the bovine periodontium to be highly inhomogeneous both within and between animals, resulting thus in its structural pattern to be hardly predictable. In fact, all of the six locations investigated revealed large variation in PDL width, area fraction and number of blood vessels, amount and orientation of collagen fibers and interface roughness of both bone- and cementum-PDL interfaces.

The high degree of vascularization of the PDL has been quantified and resulted to occupy almost the 20% of the PDL volume. The number of blood vessels per unit area, together with their diameter dependancy on root depth level and location, however, could not provide for a clear trend of the vascular structure of this connective tissue.

4.3 Mechanical testing of flat specimens

PDL's mechanical parameters obtained from flat specimens subjected to relaxation and sinusoidal tests are reported in this section. The principal aim was to complete a previous study [123] by determining their possible dependancy on specimen root depth level (I to VII) and location around the roots (mb, mm, ml, dl, dd and db).

For the analysis of all mechanical tests, the recorded load $F(t)$ and the imposed displacement $d(t)$ data (units in [N] and [mm], respec-

tively) were converted as nominal stress $T(t)$ [MPa] and stretch ratio $\lambda(t)$ [dimensionless] via

$$T(t) = F(t)/A_0 \qquad (4.3)$$

and

$$\lambda(t) = \frac{w_0 + d(t)}{w_0} = 1 + \epsilon(t) \qquad (4.4)$$

where A_0 is the initial cross-sectional area of the specimen and w_0 is the original PDL width

Note how the stretch ratio $\lambda(t)$ can also be written in terms of strain via equation 4.4

4.3.1 Preconditioning

It is well established [50] that the mechanical response of living soft tissues subjected to cyclic loading varies with the number of cycles until a steady state is reached. For the PDL it has been showed [123,125] that the number of cycles needed to obtain a steady response was greater for the compressive process (about 20 cycles) than for the tensile one (usually between 3 and 5 cycles).

As illustrated in figure 4.4, the PDL response of specimens subjected to 30 cycles of *normal* loading profile softened with the number of cycles. The enlargements of the compressive and tensile extremities show how the maximal and minimal stresses decrease over the 30 cycles.

Summary

In agreement with the procedure established in a previous work for such flat specimens, the 30th cycles of every sinusoidal loading profile was selected as the cycle after which the mechanical response was independent on the cycle number.
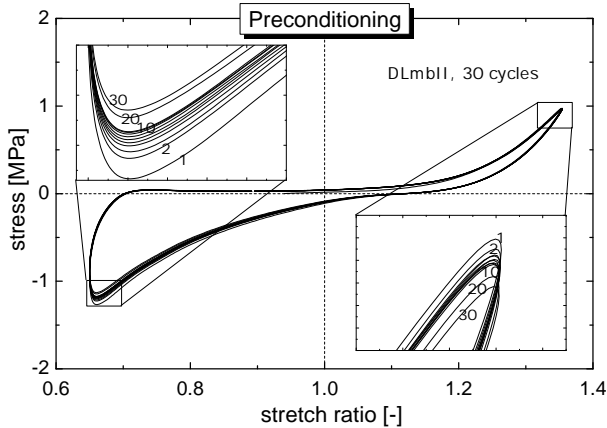
Figure 4.4: Preconditioning: the mechanical response of the PDL to cyclic loading (cycle numbers in the enlargements) was considered as steady starting from the 30th cycle on. Note: for clarity, the cycles 11-19 and 21-29 were omitted.

4.3.2 Stress relaxation

Figure 4.5 shows typical results to stress relaxation tests performed as specified in section 3.7.2 (page 86).

A systematic difference between the $relax_{tens1}$ and $relax_{tens2}$ was recorded. It was suggested that this difference was the consequence of lack of preconditioning while performing the very first relaxation step. Following the first set of cyclic loading indeed, this difference disappeared ($relax_{tens2}$ and $relax_{tens3}$ curves being practically superposed), furthermore indicating the tissue was not altered during tensile-compressive cyclic loading.
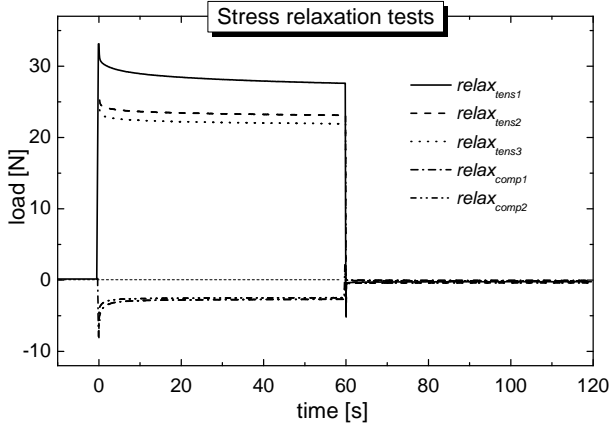
Figure 4.5: Stress relaxation curves in tension and compression before ($relax_{tens1}$), during ($relax_{comp1}$, $relax_{tens2}$, $relax_{comp2}$) and after ($relax_{tens3}$) cyclic loading. Overlapping of $relax_{tens2}$ and $relax_{tens3}$ as well as $relax_{comp1}$ and $relax_{comp2}$ denoted tissue's mechanical integrity during cyclic loadings.

4.3.3 Mechanical response to sinusoidal cyclic loading

The testing profile described on page 86 was imposed on 84 flat specimens obtained from one of the appropriate sites (6 locations and 6 depths) of the 1$^{\text{st}}$ left and right molars of 5 animals.

Typical sinusoidal loading displacement and the corresponding response curves are shown in figure 4.6a. The associated stress-stretch ratio curve is presented in figure 4.6b. The principal parameters used to quantify the evolution of the mechanical behavior of the PDL are defined on these plots. Namely,

- T_t and T_c : the maximal and minimal stresses recorded during the sinusoidal loading.

- λ_t and λ_c : the imposed maximal and minimal stretch ratios.
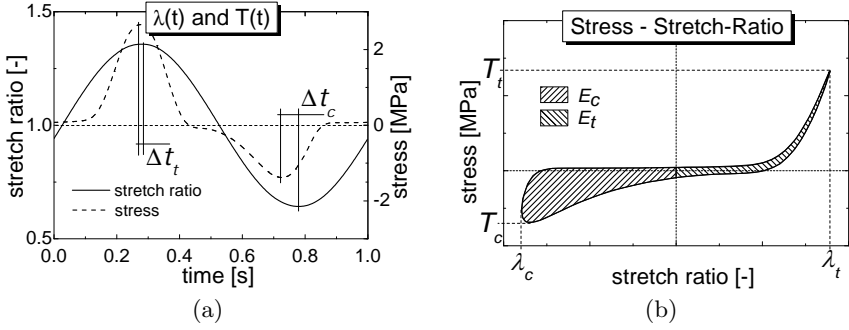
Figure 4.6: Definition of mechanical parameters; tensile and compressive time lags $\Delta t_{t,c}$ (a), maximal and minimal stresses $T_{t,c}$ and stretch ratios $\lambda_{t,c}$ and dissipated energies $E_{t,c}$ (b).

- Δt_t and Δt_c : the time differences between the occurrence of T_t and λ_t, and between T_c and λ_c, respectively.

- $\tan \delta_t$ and $\tan \delta_c$: the tensile and compressive tangent phase lags defined as

$$\tan \delta_{t,c} = \tan(\omega \Delta t_{t,c}) \qquad \text{with} \quad \omega = 2\pi f \qquad (4.5)$$

where ω is the angular frequency and f the frequency of the input signal.

- E_t and E_c : the energy needed for the tensile (compressive) phase to be completed. It corresponds to the area enclosed by the *loading* and *unloading* tensile (compressive) paths.

- H_t and H_c : the hystereses of the tensile and compressive processes, defined as the ratio between $E_{t,c}$ and the area under the *loading* path of the respective process. Hysteresis represents the fraction of mechanical energy absorbed by the system during a loading cycle.

- α_{tl}, α_{tu} and α_{cl} : the degree of non-linearity of the tensile loading (tl), tensile unloading (tu) and compressive loading (cl) paths.

These last parameters were introduced by Fung [49,50] to easily quantify the level of non-linearity of the tensile response of soft biological tissues.
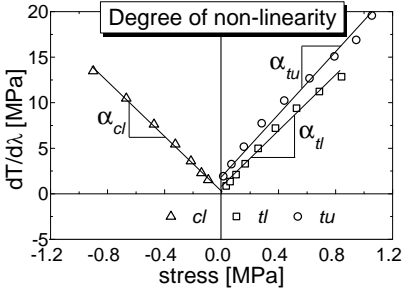

Figure 4.7: Degree of non-linearity for the tensile loading (α_{tl}), tensile unloading (α_{tu}) and compressive loading (α_{cl}) phases.

He noticed that a convenient way to examine the $T - \lambda$ relationship was to plot the values of the tangent modulus $dT/d\lambda$ of the curve versus T, as shown in figure 4.7. In fact, it turned out that, when separately considering the *loading* and the *unloading* processes, each set of data could be represented by the linear relationship

$$\frac{dT}{d\lambda} = \alpha(T + \beta) \qquad (4.6)$$

where α (dimensionless) and β (units of stress) are constants obtained by linear fitting of the curves. Integration of equation 4.6 leads to the direct relationship relating T to λ

$$T = c e^{\alpha(\lambda - \lambda^*)} - \beta \qquad (4.7)$$

where $c = T^* + \beta$ is an integration constant (T^* and λ^* are specified stress and stretch ratio on the $T - \lambda$ curve). The fact that the loading and unloading phases needed to be identified by two different sets of parameters, led Fung to name this phenomenon *pseudo*-elasticity; the material behaved as if it were ruled by an elastic law when loaded, and by another elastic law when unloaded.

All of these parameters were automatically extracted with a custom-made Matlab® (The MathWorks, Natick, Massachusetts) routine from the selected cycles (usually the 30th, for the preconditioning phase to be
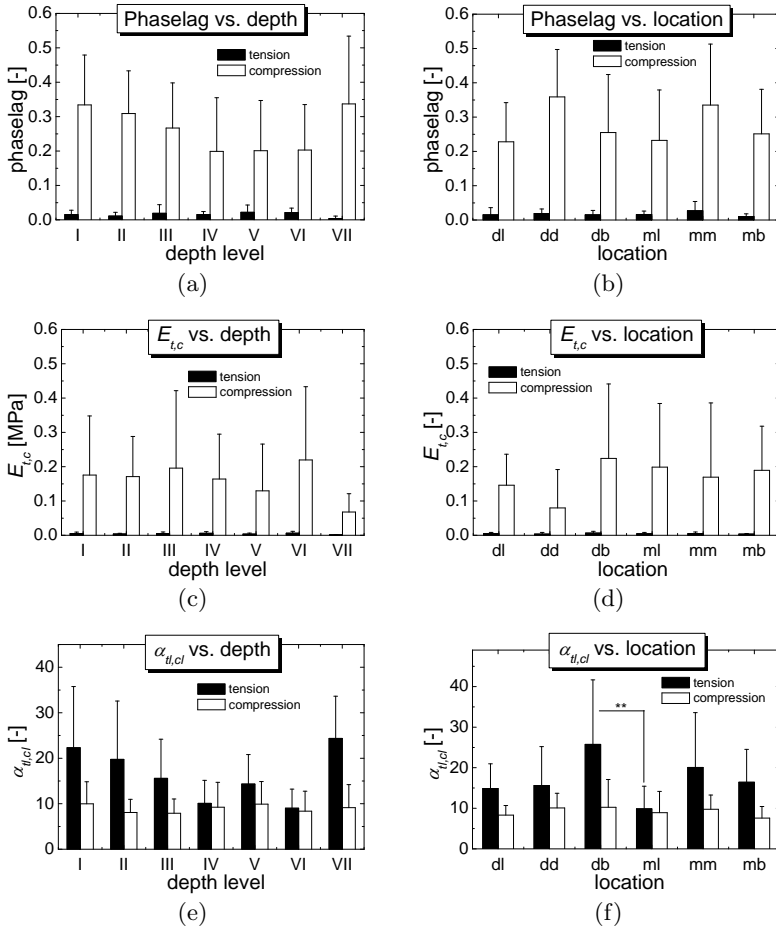
Figure 4.8: Statistical comparison of $\tan\delta_{t,c}$, $E_{t,c}$ and $\alpha_{tl,cl}$ among root depth levels (a), (c), (e) and among locations (b), (d), (f) obtained from *normal* loading profiles. Significant differences ($P = 0.001$, not illustrated for clarity) were recorded between tensile and compressive values of $\tan\delta$ and E (plots (a) to (d)). Among tensile and compressive groups no significant differences were encounterd.

The coefficients of non-linearity $\alpha_{tl,cl}$ did not present such a difference between tensile and compressive behavior. However, the tensile coefficient of location db showed to be statistically higher ($P = 0.01$) than the one of location ml.

completed – see section 4.3.1) of all the tested specimens. Comparisons and statistical analysis were carried out by pooling the data by root depth level (figures 4.8a, 4.8c and 4.8e) or location (figures 4.8b, 4.8d and 4.8f).

Summary

Although tests with different loading frequencies were performed, the results presented herein are only the ones obtained at the testing frequency of 1.0Hz, which is considered as the frequency reflecting at best the physiological stimulus.

From the plots reported in figure 4.8 it resulted that *compressive* tangent phase lag ($\tan \delta$) and energy loss (E) were much greater ($P = 0.001$) than the *tensile* values.

No significant differences were observed, however, between root depth levels or locations for these parameters, suggesting that the energy absorbing capacity of the PDL did not depend on these factors.

The non-linearity coefficients α represent the *constant* rate of increase of the tissue's stiffness with respect to increasing stress. The larger the slope α, the greater is the degree of non-linearity of the response. For the range of stretch ratio used in this work ($\lambda = 0.65 - 1.35$), it appeared that the choice of a linear fit of the curve $dT/d\lambda$ versus T was appropriate. This allowed to represent the stress-strecht ratio relationship in tension or compression by the exponential law 4.7.

In the analysis of organ functions, such a parameter is frequently used [49, 107, 136, 141, 163, 167] since it offers a convenient comparison of the non-linear behavior of different soft tissues. As a matter of comparison, the value of α_{tl} of the PDL was more than 6 times the value found for the dog's aortic tree [141], quite similar to that of the rabbit papillary muscle [107] and two-thirds that of the rabbit ureter [167].

As shown in figure 4.8, α_{tl} and α_{cl} did not show major tensile-compressive differences. Only an isolated significant difference between

110

the tensile parameter of locations db and ml was recorded.

4.4 Mechanical testing of cylindrical specimens

The main results obtained from the experimental testing of the PDL cylindrical specimens are reported in this section. All the tests were performed with the device purposely designed (see figure 4.9).

Figure 4.9: Photograph of the custom made pressure chamber (see figure 3.8 for details).

4.4.1 Comparison with flat specimens

It was essential to verify that the new extraction protocol was adequate for obtaining of cylindrical specimens and did not alter the mechanical behavior of the PDL (e.g., by excessive heating during drilling) in a significant way. Thus, a preliminary study was carried out to compare the cylindrical specimens with the classical flat ones [10]. To this end, the set of parameters reported in table 4.3 obtained from 16 flat and 16 cylindrical specimens, loaded with a 30 *normal* loading profile cycles, were statistically compared.

Table 4.3: Comparison (Student's t-test) of mechanical parameters obtained from flat and cylindrical specimens.

Param.	Flat [mean±%SD]	Cylindrical [mean±%SD]	Statistical difference
$\tan\delta_t$	0.011±82	0.016±46	NO
$\tan\delta_c$	0.235±67	0.201±34	NO
H_t	0.178±81	0.213±34	NO
H_c	0.944±17	0.841±16	NO
α_{tl}	16.4±58	13.0±40	NO
α_{tu}	17.2±59	13.9±39	NO
α_{cl}	-13.8±69	-15.1±41	NO

Both types of specimens showed similar general mechanical response; the nonlinear behavior could be quantified by extracting the slopes α from the plots of $dT/d\lambda$ vs. T (see section 4.3.3 for details) and tangent phase-lags and dissipated energy were both larger in compression than in tension.

As shown in table 4.3 there was no significant differences between the corresponding parameters of the two types of specimens. Moreover, the relaxation curves both in tension and compression, performed as described in section 3.7.2, showed that none of the specimens suffered of severe damage or degradation.

Summary

For the totality of the examined parameters, the two specimens showed a statistically similar behavior. It was then concluded that the protocol established for the extraction of the new specimens was adequate for the obtaining of PDL samples to be assigned to mechanical testing.

4.4.2 Long lasting cycling

As described on page 88, long lasting tests (2000 *normal* profile cycles), performed to guarantee consistency of the recordings on very long cyclic loadings, were executed on 5 specimens, resulting in the responses shown in figure 4.10.

After severe changes (mostly for the compressive response) during the very first cycles (1st to 100th), a more steady response to cyclic loading was obtained only after an important amount of cycles. Thus, preconditioning of the PDL proved to be a fairly long process. It was less pronounced for the tensile than for the compressive response. In fact, on average, the amount of peak stress loss over a 2000 cycles ranged at about 40% of the initial value of T_t, whereas, it was of about the 70% for T_c. The almost continuous chewing pattern of bovines could be the explanation for such a long process. Indeed, this could be the origin of possible differences between bovine and human tissues.

To determine the number of cycles after which the PDL reached an acceptable steady mechanical response, the following analysis was proposed.

Tensile behavior

The values of maximal tensile stresses T_{ti} were extracted for the ith cycle (i equal to 1, 2...10, 20...100, 200...1000 and 2000) and normalized by the peak value at the last cycle T_{t2000}. This operation was done on the 5 tested specimens so that an average value $\widehat{T}_{ti}$ could be obtained at each ith cycle (see figure 4.11). The plot of $\widehat{T}_{ti}$ versus number of cycles i was then fitted with an exponential curve of the form
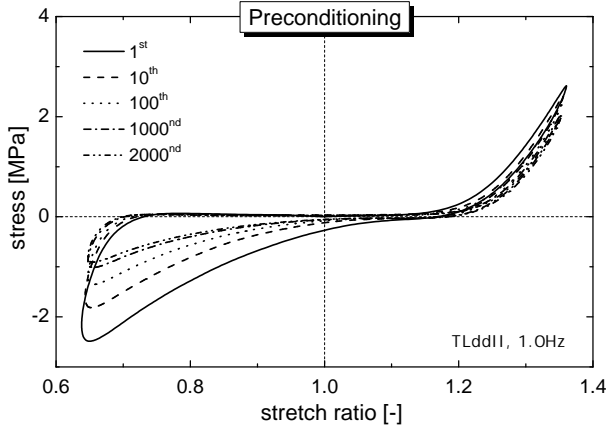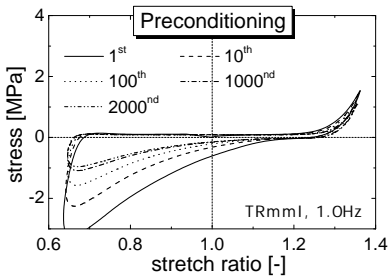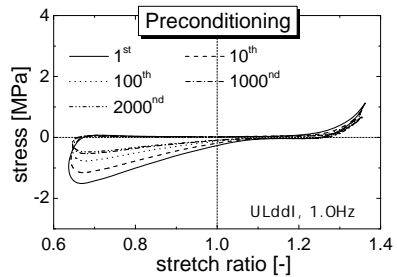
(a)
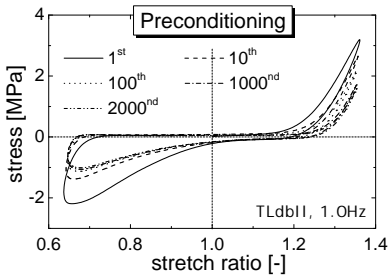
(b)
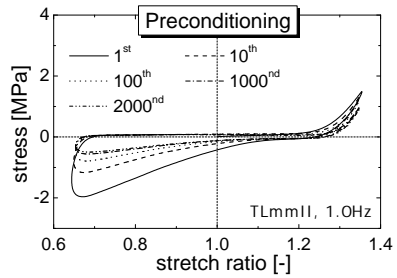
(c)

(d)

(e)

Figure 4.10: Effect of preconditioning on specimens from different locations. Nominal stress response to a 2000 *normal* loading profile cycles. As a matter of clarity, only the 1st, 10th, 100th, 1000nd and 2000nd cycles are shown.
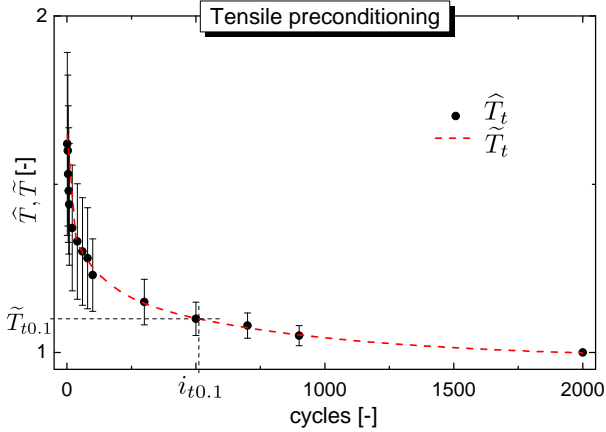
Figure 4.11: Tensile relaxation of the PDL during a 2000 sine cycling. Average of maximal tensile stress over 5 specimens with standard deviation bars and exponential decay fit.

$$\widetilde{T}_t(i) = \widetilde{T}_{t\infty} + \widetilde{T}_{t1}e^{-i/i_{t1}} + \widetilde{T}_{t2}e^{-i/i_{t2}} + \widetilde{T}_{t3}e^{-i/i_{t3}}, \qquad (4.8)$$

representing the superposition of 3 exponential decay processes, where the 3 different characteristic number of cycles (i_{tj}) indicate the *rate* at which each process (with initial amplitude $\widetilde{T}_{ti}$) vanishes with cycling, leaving $\widetilde{T}_{t\infty}$ (in this case $\widetilde{T}_{t\infty} = 1$ due to the previous normalization) as asymptotic value. Table 4.4 shows the numerical values obtained from this fitting.

Table 4.4: Values of the parameters of the exponential decay for tensile preconditioning

$\widetilde{T}_{t\infty}$	$\widetilde{T}_{t1}$	$\widetilde{T}_{t2}$	$\widetilde{T}_{t3}$	i_{t1}	i_{t2}	i_{t3}
1.00	0.30	0.19	0.22	7	109	783

To determine the minimal number of cycles up to which the speci-

mens should have been preconditioned to show nearly stable mechanical response, the effect of the total exponential decay had to be considered. Allowing for a maximal variation of 10% of the response over a large number of cycles (a maximum of 1000 cycles were imposed in the testing procedures of the cylindrical specimens), a threshold of $\widetilde{T}_{t0.1} = 1.1 \times \widetilde{T}_{t\infty} = 1.1$ was set as level for the peak tensile stress to be reached to guarantee response stability. The corresponding number of cycles was graphically extrapolated (see figure 4.11) and estimated at

$$i_{t0.1} = 511 \text{ cycles.} \tag{4.9}$$

Compressive behavior

The same procedure was followed to obtain the curve $\widetilde{T}_{ci}$, fitting the maximal compressive stresses (see figure 4.12). The corresponding

Table 4.5: Values of the parameters of the exponential decay for compressive preconditioning

$\widetilde{T}_{c\infty}$	$\widetilde{T}_{c1}$	$\widetilde{T}_{c2}$	$\widetilde{T}_{c3}$	i_{c1}	i_{c2}	i_{c3}
1.00	1.12	0.69	0.56	3	33	575

values are reported in table 4.5. The threshold and the corresponding number of cycles, were

$$\widetilde{T}_{c0.1} = 1.1, \quad \text{and} \quad i_{c0.1} = 964 \text{ cycles.} \tag{4.10}$$

Summary

For an *intra-specimen* comparison to be pertinent, the preconditioning process of the tissue should be completed. The results shown above pointed out that the minimal number of cycles suggested either by Fung [50] or Sanctuary [125] for the preconditioning of soft tissues to be completed (i.e., between 3 and 10 cycles) was not sufficient for the tests performed on the cylindrical specimens.
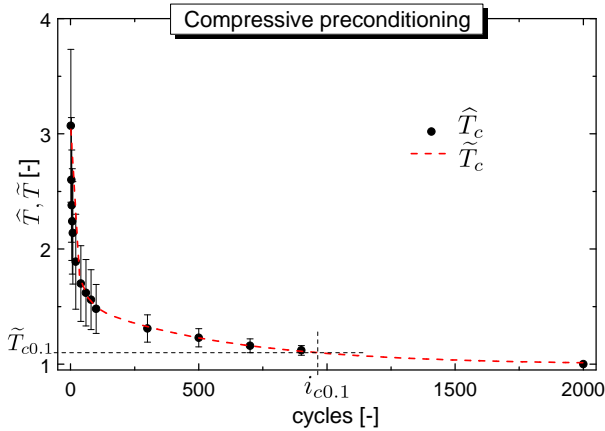
Figure 4.12: Compressive relaxation of the PDL during a 2000 sine cycling. Average of maximal compressive stress over 5 specimens with standard deviation bars and exponential decay fit.

In fact, to reach the plateau of the curves reported in the figures 4.11 and 4.12, where the mechanical response did not vary of more than the 10% of the asymptotic value, a minimal of 511 cycles (equation 4.9) for the tensile and 964 cycles (equation 4.10) for the compressive processes were needed.

Eventually, it has been established that the PDL was in a fully preconditioned state in both tensile and compressive behavior only after a minimum of a 1000 cycles.

4.4.3 *Non*-mechanical degradation

This test was performed to make sure that the PDL mechanical response did not suffered any discernible changes due to natural biological degradation while left in the testing chamber for long lasting tests

at room temperature. It also allowed to check whether the phenomena recorded during the preconditioning tests (see section 4.4.2) were strictly related to purely mechanical processes (and not to a combination of both mechanical and biological issues).

Figure 4.13 shows the last cycles of a set of three 40 cycles of *normal* loading profiles performed at time intervals of 30min (corresponding roughly to a 2000 *normal* loading cycles) on 5 specimens. The curves did not perfectly superpose; a slight softening in the mechanical response of the PDL occurred when left at rest for 30min. Moreover, this difference was more marked between the 1st and the 2nd sets than between the 2nd and the 3rd. This was mainly due to the fact that for the very 1st set the specimens were not preconditioned at all and presented air *and/or* debris, due to specimen extraction, within their fluid content (for details see section 4.4.5). Once these perturbing elements were eliminated by the action of the 1 st cycling set, the differences were less pronounced.

For each specimen, the mechanical parameters shown in table 4.6 were extracted and compared for the 40th cycles of the 3 cycling sets. The differences (loss in percent) were averaged over the 5 specimens.

Table 4.6: Mean and standard deviation of percent differences of mechanical parameters for *non*-mechanical degradation tests.

Param.	1st-2nd sets [%]	2nd-3rd sets [%]
T_t	3.7±2.8	3.5±2.5
T_c	15.9±2.5	8.7±2.2
E_t	7.7±3.9	6.4±3.0
E_c	11.0±2.8	8.1±2.9

Summary

For a waiting time of 30min between cycling, the variation of the mechanical response of the PDL did not exceed 8.7% of the initial value of

(a)
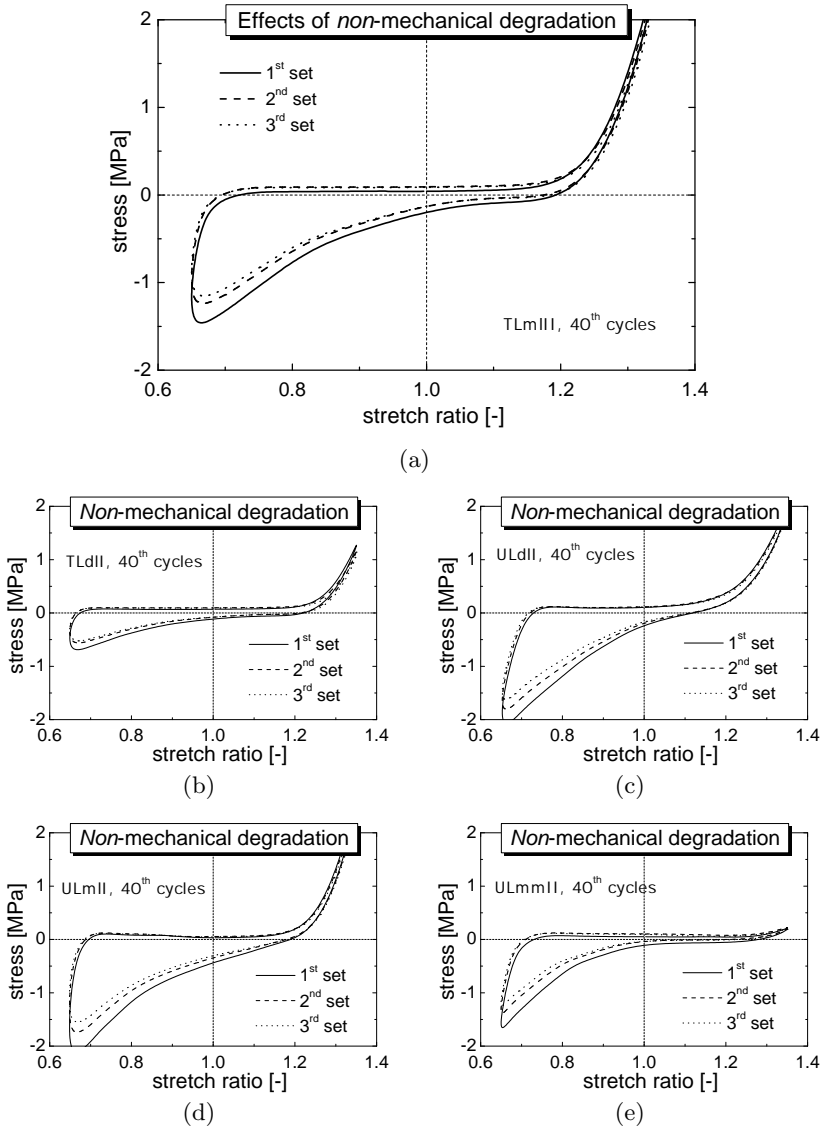

(b)

(c)

(d)

(e)

Figure 4.13: Effect of *non*-mechanical degradation: 40th cycles of the 3 sets of cycling executed at time intervals of 30min.

the control parameters. This value was obtained only when the tissue was previously put in a fully saturated saline state: all the air *and/or* debris contained in the tissue were evacuated in the 1$^{\text{st}}$ cycling set. If this was not the case, higher values were obtained (15.9%).

These variations were considered small for biological tissues and were not investigated further.

4.4.4 Effects of loading frequency

As a consequence of the findings on the preconditioning behavior (see section 4.4.2), every specimen was subjected to a 1000 cycles (at 1.5Hz in this case) prior data recording.

The results obtained by applying on 5 specimens the testing profile described on page 88 are shown in figure 4.14. In the plots, the 10$^{\text{th}}$ (crosses) and the 100$^{\text{th}}$ (solid lines) cycles are displayed for each testing frequency.

Table 4.7 shows the mean differences (in percent and calculated over the 5 specimens) between the 10$^{\text{th}}$ and the 100$^{\text{th}}$ cycles of each frequency for the parameters T_t, T_c, E_t and E_c. Apparently, no significant changes

Table 4.7: Comparison of mechanical parameters between the 10$^{\text{th}}$ and the 100$^{\text{th}}$ cycles for the four testing frequencies.

Parameter	1.5Hz 10$^{\text{th}}$-100$^{\text{th}}$ cycles [%]	1.0Hz 10$^{\text{th}}$-100$^{\text{th}}$ cycles [%]	0.5Hz 10$^{\text{th}}$-100$^{\text{th}}$ cycles [%]	0.1Hz 10$^{\text{th}}$-100$^{\text{th}}$ cycles [%]
T_t	7.1±3.1	4.5±2.2	2.1±0.9	3.0±1.1
T_c	5.4±2.1	2.7±1.5	0.8±0.7	4.6±1.4
E_t	4.1±1.4	2.1±1.2	1.2±1.1	3.3±2.4
E_c	5.8±2.0	2.7±1.6	0.5±0.3	2.9±2.4

in the mechanical response of the PDL occurred within each testing frequency.
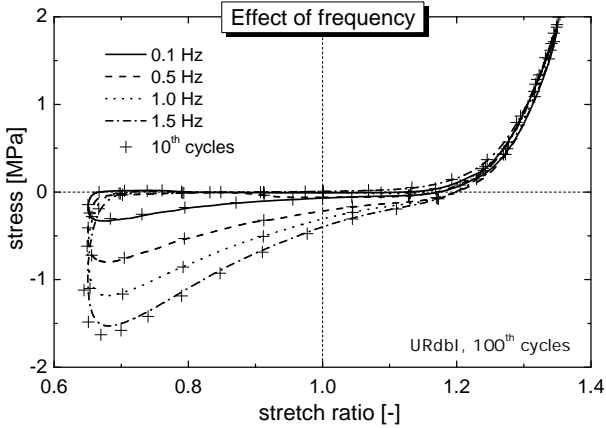
(a)
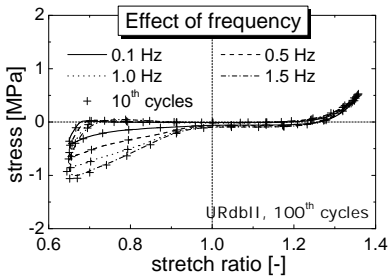
(b)
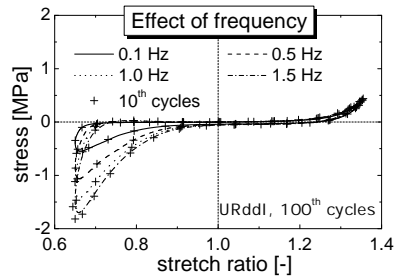
(c)
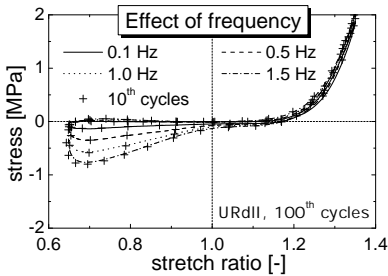
(d)
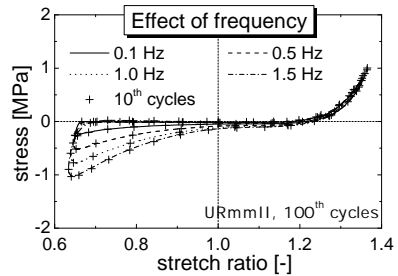
(e)

Figure 4.14: Effect of frequency: 10th and 100[th]cycles for 0.1, 0.5, 1.0 and 1.5Hz frequencies. Each line style indicate the 100th cycle of a testing frequency; the closest set of crosses (+) to each line indicate the 10th cycle of the corresponding testing frequency.

By assessing the differences between the 100th cycles of the different testing frequencies, however, significant changes occurred (see table 4.8, **bold** faced values). The amplitude of these differences were systemat-

Table 4.8: Comparison of mechanical parameters between the 100th cycles of the four testing frequencies.

| Parameter	0.1-0.5Hz 100th cycles [%]	0.5-1.0Hz 100th cycles [%]	1.0-1.5Hz 100th cycles [%]
T_t	5.8±2.1	3.5±4.0	3.2±4.3
T_c	**106.8±40.4**	**44.9±13.7**	**27.1±6.1**
E_t	*32.3±11.7*	*22.6±16.3*	14.8±13.8
E_c	**125.4±33.3**	**48.8±15.4**	**27.6±8.4**

ically lower for the parameters describing the tensile behavior (i.e., T_t and E_t) than the values for the compressive parameters. This clearly indicated that the major changes took place during the compressive part of the cycle, while the tensile phase was practically unaffected by the variation of the loading frequency.

Quite high values (in *italic* in table 4.8) were also recorded for the tensile parameter E_t (the energy loss during the tensile phase of the cycle). This was because the transition path between the tensile and compressive states was affected by frequency changes already in the tensile phase (striking in plot 4.14a). This caused the loop area defining E_t to increase with frequency. Moreover, the numerical value of E_t being close to zero, any slight variation of it resulted in a sensible percent difference.

The PDL showed two very different responses depending on whether it was pulled in tension or pushed in compression.

Tensile behavior

The response to the tensile part of the sinusoidal excitation did not significantly vary for frequencies spanning over more than one order of magnitude (0.1 to 1.5Hz). The loss of energy E_t (i.e., the area between the loading and unloading processes), and the maximal stress T_t could be considered as constant.

These features indicated that the model of *pseudo*-elasticity proposed by Fung [50],

$$T = ce^{\alpha(\lambda - \lambda^*)} - \beta \tag{4.11}$$

and already used in section 4.3.3, still well represented the tensile behavior of the PDL, at least for the given range of frequencies and displacements (well within the physiological range).

Compressive behavior

The loading frequency had a marked influence on the compressive response of the PDL. Dependency of maximum compressive stress and compressive energy loss on the loading rate indicated the material to present a significant viscous behavior.

A viscous component is generally represented as a dashpot, such as the stress-stretch ratio rate relationship is given as

$$T = \eta\frac{d\lambda}{dt} = \eta\dot{\lambda} \tag{4.12}$$

where the stress T is proportionally related to the time derivative of the stretch ratio $\dot{\lambda}$ via the viscosity of the material η.

The viscosity η can be independent, and in this case the material is said to be linear viscous, or dependent, indicating a non-linear viscous behavior, on $\dot{\lambda}$. In this last case, the description of the dependency of η on $\dot{\lambda}$ is assessed empirically [15]. To establish what type of viscosity described best the PDL compressive behavior, the following data analysis was carried out for the 5 specimens.

The plot of the stresses T versus the stretch ratio rate $\dot{\lambda}$, directly indicated the type of relationship between η and $\dot{\lambda}$ (see equation 4.12);

obtaining of a straight line would be the evidence of linear viscosity, whereas a curved line would imply non-linear viscosity.
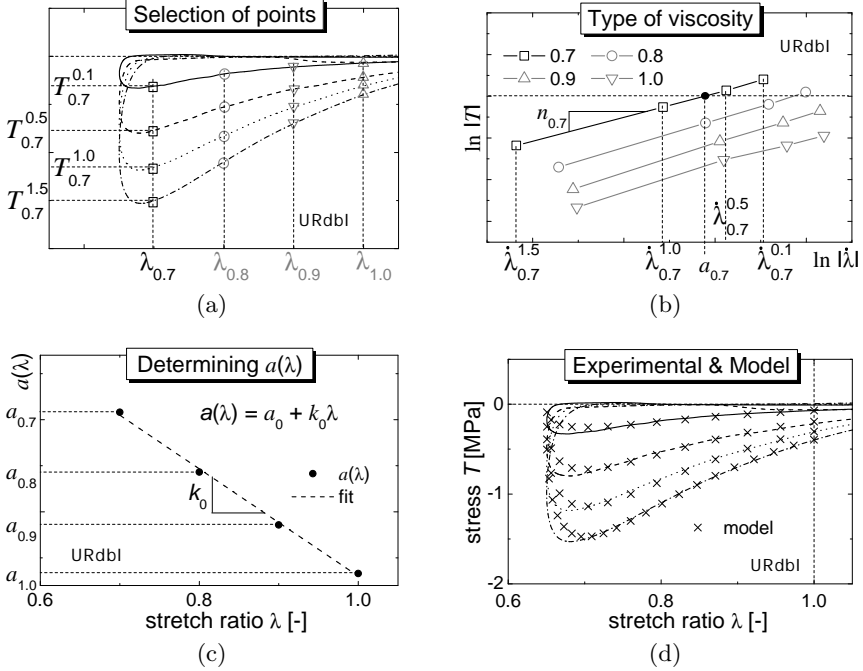

Figure 4.15: Assessment of the type of viscosity. (a): Different stretch ratios (λ_x) were selected and the corresponding stresses T_x^f for the different loading frequencies were recorded. (b): Plot of the corresponding data form (a) in a ln-ln graph. (c): Determination of $a(\lambda)$. (d): Comparison between the experimental curves (lines) and the model ($\times$) for $a_0 = 4.13$, $k_0 = -5.83$ and $n_0 = 0.64$.

Figure 4.15a shows a magnification of the compressive response of specimen URdbI (from plot 4.14a) for the four loading frequencies. The stretch ratio $\lambda = 0.7$ ($\lambda_{0.7}$) was selected, and the corresponding stresses noted for the different loading frequencies f ($T_{0.7}^f$, for $f = 0.1 - 1.5$). Also, the time derivative of the stretch ratio function was calculated at the selected stretch ratio, giving the values $\dot{\lambda}_{0.7}^f$. Plotting $|T_{0.7}^f|$ versus $|\dot{\lambda}_{0.7}^f|$ in a ln-ln graph (4.15b) clearly showed a linear logarithmic

dependency between the two terms:

$$\ln|T| = a_{0.7} + n_{0.7}\ln|\dot{\lambda}| \tag{4.13}$$

implying a direct relationship of the form

$$|T| = e^{a_{0.7}}|\dot{\lambda}|^{n_{0.7}} \tag{4.14}$$

which can be rewritten as

$$|T| = \underbrace{e^{a_{0.7}}|\dot{\lambda}|^{n_{0.7}-1}}_{\eta_{0.7}}|\dot{\lambda}| \tag{4.15}$$

where term $e^{a_{0.7}}|\dot{\lambda}|^{n_{0.7}-1}$ represents the viscosity $\eta_{0.7}$, comparable to η of equation 4.12. In the case of Note that for $n_{0.7} = 1$ and $e^{a_{0.7}} = \eta$, the viscosity is linear. Thus, the deviation of $n_{0.7}$ from the unity indicates the deviation of the behavior from linear viscosity.

This operation was reiterated for the stretch ratios $\lambda_{0.8}$, $\lambda_{0.9}$ and $\lambda_{1.0}$ to extract the corresponding parameters a_λ and n_λ. By plotting the obtained values of $|T_\lambda^f|$ and $|\dot{\lambda}_\lambda^f|$ on the same plot 4.15b, it has been noticed that the viscosity was not only dependent on $\dot{\lambda}$, but also on λ (the curves did not superpose); whereas the slope $n_\lambda = n_{0.7} = n_0$ did not vary, the shifting value a_λ was found to be dependent on λ (see plot 4.15c) via a linear relationship of the type

$$a(\lambda) = a_0 + k_0\lambda \tag{4.16}$$

Thus, the final form for the stress-stretch ratio relationship for the loading part of sinusoidal compressive path was

$$T = -e^{a_0+k_0\lambda}|\dot{\lambda}|^{n_0-1}|\dot{\lambda}| \tag{4.17}$$

The comparison between the experimental data and the model is shown in the plot 4.15d for the specimen URdbI. A good match was found so that the tree-parameters model 4.17 well described the sinusoidal compressive loading of the PDL for different frequencies. The

Table 4.9: Parameters for the viscous model.

Specimen	a_0	k_0	n_0
URdbI	4.13	-5.83	0.64
URdbII	4.82	-7.36	0.37
URddI	7.23	-10.41	0.33
URdlI	3.78	-6.28	0.55
URmmII	3.91	-6.44	0.51
mean±SD	4.77±1.43	-7.26±1.85	0.48±0.13

values of a_0, k_0 and n_0 obtained for the 5 specimens are reported in table 4.9.

The fact that n_0 was less than 1 implied that the term representing the viscosity η decreased with increasing $\dot{\lambda}$. For a viscous behavior this feature is termed *pseudo-plasticity* [15].

Summary

Varying the displacement loading frequency had a direct influence on the mechanical response of the PDL. Whereas the tensile behavior showed to be almost independent on it, the compressive response proved to be highly affected by the loading rate.

The tensile response of the PDL to sinusoidal cycles with characteristics within the physiological range, could be described by the same model as presented in section 4.3.3 and proposed by Fung [50]. The stiffness $dT/d\lambda$ of the PDL was found to be exponentially dependent on the stretch ratio λ, i.e., the *tangent modulus* of the ligament response varied with the geometrical configuration of the specimen. From a phenomenological point of view, the explanation for such a response is commonly attributed to the progressive straightening, thus engaging in the loading bearing process, of the tissue's collagen fibers with increasing stretch.

The compressive response of the PDL presented viscous features. From the analysis of the results it appeared the viscosity η to be non-linear, dependent on the loading rate $\dot{\lambda}$ *and* on the stretch ratio λ itself. This direct dependency on λ suggested, as in the case of the tensile response, that the process laying behind the compressive behavior should likewise be linked to a structural modification. This change could be the progressive collapse of the pore spaces (mainly represented by blood vessels, see section 4.2.1) contained in the PDL. Thus, the dependency of the compressive response on the loading frequency, could be due to the interactions between a porous structure, which pore volume can vary with deformation, and its fluid content, rather than to viscoelastic properties of a continuum PDL.

It is important to emphasize that the two models presented here are limited, as they *separately* described the tensile (loading and unloading) and the compressive (loading only) phases of the response to the specified loading profile.

4.4.5 Optical monitoring and measurements

The four control viewports integrated in the pressure chamber allowed for the direct observation of the specimen during the loading sequences. This was important to have a real-time visual feedback in order to check for the integrity of the specimen, and for the monitoring of the associated phenomena.

Fluid flow

It was mentioned earlier (section 4.4.4) that compressive loading of the PDL could induce its pore volume to decrease. Therefore, due to its incompressible character, the fluid, contained in the pore space, had to come out during the compression of the PDL.

This process was well observed during the cyclic testing and recorded

via a digital camera. An example of these recordings can be found in the CD-ROM included at the end of this manuscript (see the VideoPDL folder).

It was noticed that during the first compressive cycles, before any preconditioning, air bubbles and/or debris (e.g., bone and dentin) probably collected during the cutting procedure, were progressively squeezed out of the PDL, and subsequently replaced by the saline solution drawn in the pore spaces during the tensile phases. Once all the *parasites elements* were evacuated, only saline flowed in and out during cycling.

Apparent Poisson's ratio

Form the series of images acquired, a value for the *apparent* Poisson's ratio of the PDL was evaluated. The use of the adjective *apparent* is justified as this constant is only defined for a linear elastic behavior, and, as all plots of T versus λ show, this is not the case for the PDL. However, this value could give general indications as to the compressibility of the PDL.

In the analysis of these images with a commercial software (Matlab$^{\circledR}$, The MathWorks, Natick, Massachusetts, USA) the lateral deformation Δd of 5 specimens was tracked and measured (at 24 frames per second) during 3 cycles around the 1st, the 10th, the 100th and the 1000nd cycles of a 1000 *normal* loading profile cycles test. The Poisson's ratio ν was calculated as

$$\nu = -\frac{\epsilon_{trans}}{\epsilon_{axial}} = -\frac{\Delta d/d_0}{\Delta w/w_0} \tag{4.18}$$

where ϵ_{trans} and ϵ_{axial} are the transversal and axial strains, respectively; d_0 was the initial diameter of the specimen and Δd its deformation (see figure 4.16a); w_0 was the initial PDL's width and and Δw its deformation. ϵ_{axial} was easily obtained as

$$\epsilon_{axial} = \lambda - 1 \tag{4.19}$$
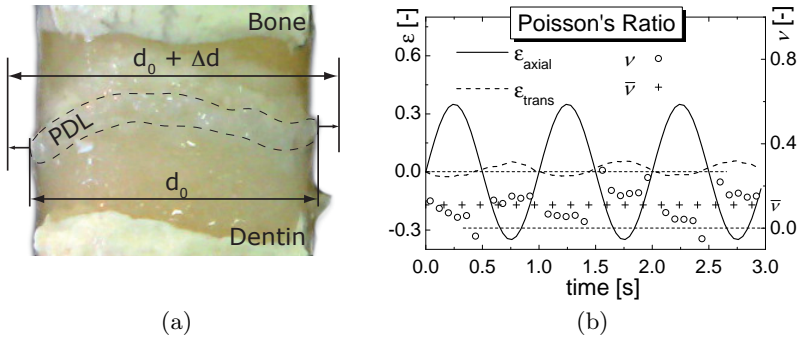
(a)   (b)

Figure 4.16: Definition of the parameters for the determination of the apparent Poisson's ratio (a) and plot of ϵ_{trans}, ϵ_{axial}, ν and $\bar{\nu}$ versus time for 3 cycles (b).

The graph of figure 4.16b shows the superposition of the measured transversal ϵ_{trans} and the imposed axial strain ϵ_{axial} for 3 loading cycles. Using equation 4.18, the Poisson's ratio was obtained at every image and averaged over the 3 cycles. Eventually, a general mean was computed over the totality of the measurements to give a PDL Poisson's ratio of

$$\bar{\nu} = 0.086 \pm 0.016 \qquad (4.20)$$

Summary

An important fluid exchange between the PDL and the external environment has been observed. This clearly indicated that the PDL possesses an *open* type of porosity. Moreover, preconditioning effects (see section 4.4.2) could be partially explained by the expulsion of air bubbles and/or solid particle debris from the ligament during the firsts testing cycles.

These findings suggested that, in order to obtain a more realistic mechanical response of the PDL, a lateral confinement was needed as to avoid the fluid to flow out of the specimen without the resistance that the missing surrounding tissues would have exerted on it.

A Poisson's ratio of $\nu = 0.086$ has been evaluated. Compared to what reported in the literature, this value suggested a very high compressibility of the PDL; values ranging between 0.25 and 0.49 were commonly adopted in most of the works treating this ligament as a linear elastic material [63, 67, 94, 112, 113, 120, 123, 126, 145, 171].

Furthermore, it was noticed that the value obtained was comparable to the ones typical for foam-like materials, which Poisson's ratio is slightly above zero [87] or even negative [54].

4.4.6 Porosity of the periodontium

It has been established that alveolar bone and cementum both presented some degree of porosity. Since the PDL is bounded between these hard tissues, it was thus pertinent to suppose that fluid exchange between PDL and bone or/and PDL and cementum-dentin could take place during the mechanical loading, influencing thus the total response of the bone-PDL-cementum system.

Porosity of the alveolar bone

Alveolar bone porosity values (n_{bone}) are rarely found in the literature. Nevertheless, the porosity of cortical bone from femur [9,153], mandible [149], and other compact bones [31], ranging between 8 to 12%, could be taken as representative values, since these tissues are considered to be of the same nature as alveolar bone.

However, form the histological observations detailed in section 4.2, it could be stated that, due to the presence of soft tissue inclusions derived from the process of bone remodeling, n_{bone} was likely to be higher than the cited values.

Porosity of the cementum-dentin

Cementum showed a very low degree of porosity. The few values obtained from a literature survey were of about $n_{cem} = 5\%$ [115]. This

porosity is mainly due to the presence of very tiny tubules called *dentinal tubules* [127, 169] connecting the pulp of the teeth to the PDL and to the oral cavity, though the enamel. Teeth hypersensitivity to cold and/or hot foodstuff has been proved to be related to the presence of these tubules [100, 169].

In the specific case of bovine tissue, it has been lately found [19] that, in opposition to what observed for humans, soft tissue inclusions could also form within cementum. This finding suggested, as it was the case for bone porosity, a higher value for n_{cem} than the ones cited in the literature.

Porosity of the PDL

For what concern the PDL, the experimental protocol described on page 89 was followed to obtain a value for its porosity. In table 4.10 are reported the measurements obtained for 5 specimens.

Table 4.10: Porosity of the PDL.

Specimen	V_0 [mm^3]	W_{paper}^{dry} [g]	W_{paper}^{wet} [g]	n_{PDL} [-]
VLdbI	21.27	0.023	0.040	0.89
VLdlI	15.30	0.074	0.086	0.75
VLmmI	8.16	0.064	0.068	0.49
VLdbII	17.91	0.046	0.057	0.53
VRdlI	16.59	0.048	0.060	0.69

The mean value and corresponding standard deviation are

$$n_{PDL} = 0.67 \pm 0.17 \qquad (4.21)$$

A more common quantity used to indicate the amount of voids into a solid matrix is the void ratio $\bar{e}$. It is related to the porosity via

$$\bar{e} = \frac{n}{1 - n} \qquad (4.22)$$

131

and represents the ratio between the volume of pores V_{pores} and the volume occupied by the solid matrix $V_{matrix} = V_0 - V_{pores}$.

It must be noticed that this value was valid only for the *zero* state configuration of the PDL. In fact, as already mentioned in sections 4.4.4 and 4.4.5, the pore volume of the ligament could vary deformation.

Summary

Values for the porosity of the three tissues composing the periodontium were obtained.

Alveolar bone and cementum porosity were retrieved for a literature survey. However, the proposed values ($n_{bone} \cong 0.1$ and $n_{cem} \cong 0.05$) were judged to underestimate the real porosity, as soft tissue inclusions due to remodeling processes were found both in bone and cementum (see section 4.2).

PDL porosity was experimentally assessed to $n_{PDL} = 0.67$. This value was well in line with what proposed in different works on ligaments and tendons [22, 94, 104, 148], where the porosity of soft tissues ranged from 0.5 to 0.8. Evidently, this value represented the porosity of the tissue in its *zero* states; a different configuration should indeed vary the pore volume.

4.4.7 Permeability of the periodontium

As mentioned in the previous sections (4.4.5 and 4.4.6) all of the components of the periodontium presented a more or less high degree of porosity. When mechanically loaded, such porous medium deforms, inducing modifications of the pore space volume, letting thus the fluid phase flow through the solid skeleton.

Histo-morphological studies certified that both alveolar bone and cementum were likely to allow for fluid exchanges with the PDL. On the bone side, this was guaranteed by the presence of vascular cap-

illaries and large soft tissue inclusions, resulting from tissue remodeling activity, which, moreover, has been related to fluid flow generated stresses [90, 95, 139]. On the cementum side, fluid flow was allowed by the dentinal tubules.

The permeability of the constituent of the periodontium was assessed via the experimental protocol described on page 89.

Permeability of the alveolar bone

Since, during cyclic tensile-compressive mechanical loading, the fluid could flow both out and in the PDL, permeability measurements were done twice for each specimen; (i) with the bone-PDL interface oriented outwards and (ii) with the bone-PDL interface oriented inwards (see figure 3.11b).

The values (imposed —*italic*— or measured —**boldface**—) of the quantities needed to assess the permeability of alveolar bone (see equations 3.8 – 3.10) are summarized, for two specimens, in table 4.11.

Table 4.11: Permeability of two specimens of alveolar bone. Note: for the specimen XLddI it was not possible to obtain a valid measure when the bone-PDL interface was placed inwards (the other surface was too irregular to guarantee the complete sealing by the downstream joint (see figure 3.11b)).

Spec.	d [mm]	h [mm]	Outw. face	Δt [s]	ΔP [kPa]	ΔV [mm^3]	k_s^{bone} [mm/s]
WLmmI	*4.00*	*2.45*	PDL	*300*	*50*	**1300**	1.68×10^{-4}
			Bone	*300*	*20*	**2850**	9.22×10^{-4}
XLddI	*4.00*	*2.14*	PDL	*300*	*20*	**1740**	4.90×10^{-4}
			Bone	—	—	—	—

Note: Due to the maximal flow supply limit of the pressure pump, an imposed pressure gradient of $\Delta P = 50$kPa was reached only in one case. For the other cases a lower pressure level (20kPa) had to be chosen, so that the pump could supply the necessary saline flow able to generate a constant pressure gradient.

A mean value of

$$k_s^{bone} = 5.27 \times 10^{-4} \text{ mm/s} \tag{4.23}$$

was retained for the hydraulic conductivity of the alveolar bone.

Permeability of the cementum

The same procedure was followed to measure cementum permeability. The relevant values are shown in table 4.12 and the mean value for

Table 4.12: Permeability of two specimens of cementum.

Spec.	d [mm]	h [mm]	Outw. face	Δt [s]	ΔP [kPa]	ΔV [mm^3]	k_s^{cem} [mm/s]
WLmmI	4.00	2.04	PDL	1800	50	**43**	7.71×10^{-7}
			Cem.	1800	50	**37**	6.63×10^{-7}
XLddI	4.00	2.17	PDL	1800	50	**4**	7.65×10^{-8}
			Cem.	1800	50	**2**	3.82×10^{-8}

cementum permeability was

$$k_s^{cem} = 3.87 \times 10^{-7} \text{ mm/s} \tag{4.24}$$

Permeability of the PDL

As mentioned in section 3.7.3 (page 89), due to its geometrical and structural characteristics, the experimental determination of the permeability of the PDL is not an easy task. In fact, the few values found in the literature come usually from a numerical derivation [94, 148].

The results reported in sections 4.4.4 and 4.4.5 led to the conclusion that the pore volume of the PDL varied as a function of deformation. As shown by equation 2.42, permeability is in general dependent on the geometrical dimensions of the pores. Consequently, k_s^{PDL} should as well be a function of the amount of deformation.

An exponential form, based on standard forms used to describe permeability of soft biological tissues (like inter-vertebral disks [4,131]),

of $k_s^{PDL}(\bar{e})$, where $\bar{e} = \bar{e}(\lambda)$, was proposed and identified via a numerical model (see section 5.2).

Summary

The permeability values of the three tissues constituting the periodontium were assessed. Whereas for alveolar bone and cementum numerical values could be experimentally obtained, for the PDL an identification from a numerical simulation was needed.

Alveolar bone permeability k_s^{bone} (see equation 4.23) resulted to be 3 orders of magnitude higher than the one of cementum. Its higher porosity n_{bone} (see section 4.4.6) together with the presence of capillary blood vessels crossing the bone-PDL interface (see section 4.2.1 and [129]), should be the reason for this difference. Explicit values for it are rarely found in the literature, but comparison with the reported quantities assessed for cortical bone (ranging from 3×10^{-6} to 7×10^{-1} mm/s, [32, 68, 80, 148]) showed the obtained value to be reasonable.

Cementum appeared to be less porous, the only pore spaces being represented by the *dentinal tubules* [127] and the rare bovine-specific soft tissue inclusion [19]. This resulted in a much lower permeability. Zahng et al. [169] obtained values of higher magnitude than what evaluated herein. The difference, however, was explained by the fact that in their study the cementum surface was treated (by acid etching or polishing) prior measurements to open free all of the dentinal tubules.

It has been suggested that permeability of the PDL largely depended on porosity, thus on stretch ratio. Such a dependency was integrated in the numerical model exposed in section 5.2.

Note: The results reported in these last two sections (4.4.6 and 4.4.7) lead to the following conclusion: *for an accurate and realistic modeling of the PDL, it is necessary to take into consideration the surrounding*

mineralized tissues, i.e., alveolar bone and cementum, to account for the fluid exchanges between these strictly connected tissues. When trying to simulate the mechanical behavior of this ligament thus, the *periodontium*, including alveolar bone and cementum, should be considered as the **elementary unit**.

4.4.8 Matrix and fluid contributions

The protocol described on page 91 was followed to establish the contribution of the fluid phase to the mechanical response of the PDL. The two tests, *saturated* and *blotted*, were sequentially performed on 5 specimens. Preconditioning of the tissue (see section 4.4.2) was guaranteed by performing a 1000 *normal* loading profile cycles for both testing conditions. Moreover, relaxation tests were carried out to check for the tissue's mechanical integrity during the entire testing procedure.

The response to the 1000nd cycles are shown, for the *saturated* and the *blotted* tests, in figure 4.17.

As shown in figure 4.18, where typical responses to the three relaxation tests are reported, the peak (F^{peak}) and tail (F^{tail}) loads were compared. The differences (average in percent over the 5 specimens) of the values obtained from rel_{02} and rel_{03} to the values of rel_{01} are given in table 4.13. Losses in F^{peak} and F^{tail} of about 13% were recorded for

Table 4.13: Differences between relaxation responses during fluid contribution tests.

Parameter	rel_{02} - rel_{01} [%±SD]	rel_{03} - rel_{01} [%±SD]
F^{peak}	-12.1±5.3	-13.6±4.7
F^{tail}	-13.3±5.5	-15.3±6.0

both rel_{02} and rel_{03}.
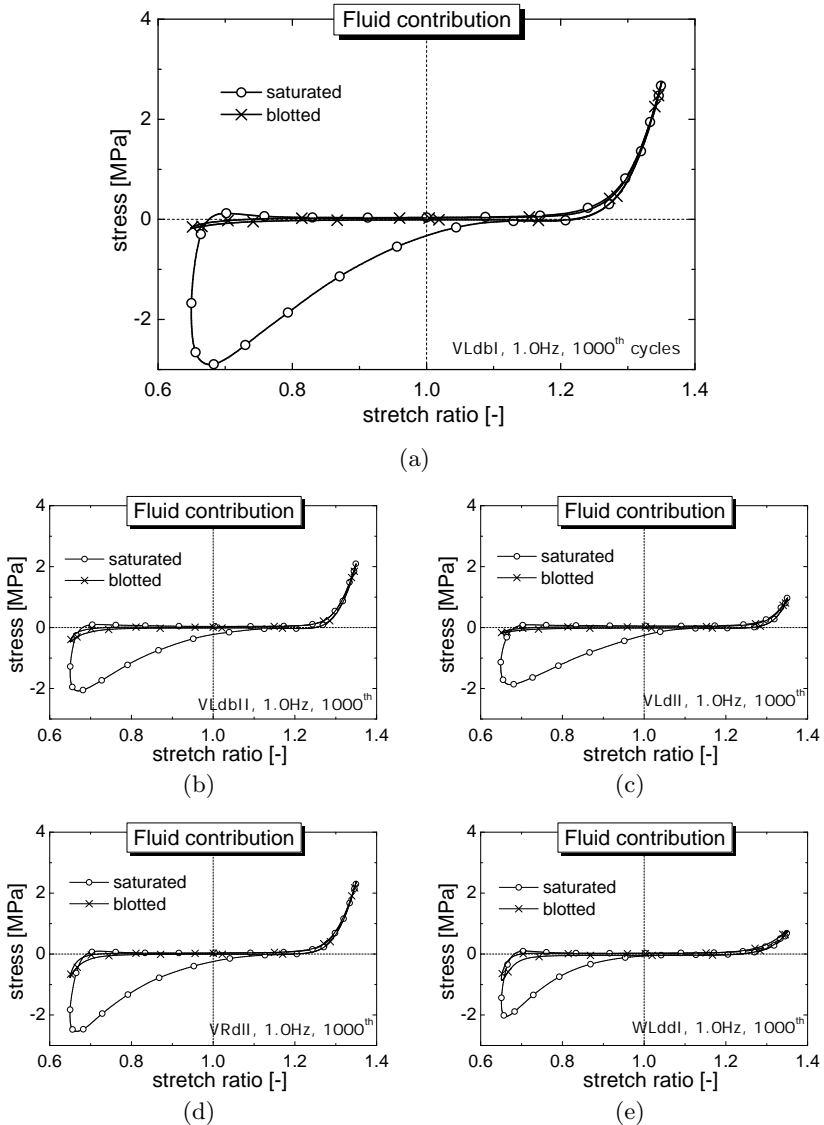
(a)

(b)

(c)

(d)

(e)

Figure 4.17: Contribution of the fluid phase to the mechanical response of the PDL: curves at the 1000nd cycles for the *saturated* (–o–) and the *blotted* (–x–) tests.
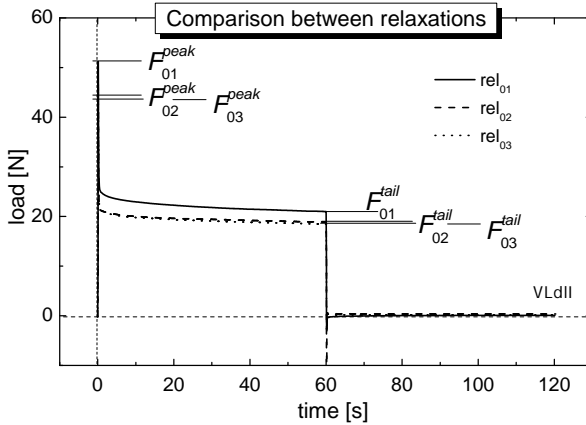
137

Figure 4.18: Typical relaxation responses before *saturated* (rel_{01}), between *saturated* and *blotted* (rel_{02}) and after *blotted* (rel_{03}) tests.

Tensile behavior

The nearly perfect graphical superposition of the tensile responses in the two testing conditions demonstrated that the fluid content played a minor role during the tension phase. A slight difference was only noticed for the tensile unloading process, starting at about $\lambda = 1.1$ down to $\lambda = 1.0$.

The tensile parameters T_t, E_t, α_{tl} and α_{tu} were evaluated for the curves plotted in figure 4.17. In table 4.14 are shown the differences (average in percent over the 5 specimens) between the *saturated* and the *blotted* parameters.

Beside a decrease of 36.7% (in bold in the table 4.14) in the energy loss for the *blotted* with respect to the *saturated* test, all of the differences were minimal.

Table 4.14: Difference in mechanical tensile parameters between *saturated* and *blotted* conditions.

Parameter	sat - $blot$ [%±SD]
T_t	-3.1±3.9
E_t	**-36.7±15.3**
α_{tl}	-2.1±7.6
α_{tu}	0.9±4.2

Compressive behavior

Important changes were observed during the compressive phase of the cycle when the pore fluid was squeezed out of the ligament; the clear hysteresis recorded in the *saturated* test almost completely disappeared, and a behavior similar to the one obtained for the tensile phase (i.e., *pseudo*-elastic behavior) was obtained.

The parameters describing the compressive response were compared for the two testing conditions in the same manner as it has been for the tensile ones. Table 4.15 relates the variations of T_c, E_c and α_{cl}.

Table 4.15: Difference in mechanical compressive parameters between *saturated* and *blotted* specimens.

Parameter	sat - $blot$ [%±SD]
T_c	**-77.8±14.9**
E_c	**-93.7±4.4**
α_{cl}	**478.7±151.3**

All of the differences were clearly significants, with a drastic loss in T_c and E_c and a dramatic increase of the response non-linearity coefficient α_{cl}.

Summary

The influence of the fluid content of the PDL on its mechanical response to sinusoidal cyclic loading was investigated. Its contribution was found to be unequal, depending on whether the tissue was in a tensile or a compressive state.

Relaxation tests certified that the tissue did not suffer any damage during testing. In fact the difference between the parameters obtained for rel_{02} and rel_{03} were minimal (2% at most, see table 4.13). The 13% difference of rel_{02} and rel_{03} from the first relaxation test was attributed to the complete lack of preconditioning of the specimens before rel_{01} was taken.

On the one hand, emptying the ligament of its fluid content did not affect much the tensile parameters describing the pseudo-elastic behavior (the two degrees of non-linearity and the maximal stress), only the dissipated energy during the loading-unloading process slightly decreased.

On the other hand, the fluid phase seemed to play a major contribution during the compressive phase of the cycle. In fact, once the fluid was blotted out of the tissue, the compressive behavior almost completely lost its dissipative character in favor of a pseudo-elastic tensile-like behavior.

It was furthermore established that the viscous behavior reported in section 4.4.4 strongly depended on the level of saturation of the PDL. In fact, performing the same test used to investigate the effect of frequency on a specimen initially in saturated (see figure 4.19a) and subsequently in blotted (figure 4.19b) conditions, resulted in the dependency of the compressive response to the loading rate to be less pronounced for the second case.

In blotted conditions, loading rate dependancies were only observed for highly compressive states ($0.65 < \lambda < 0.75$). These viscous effects
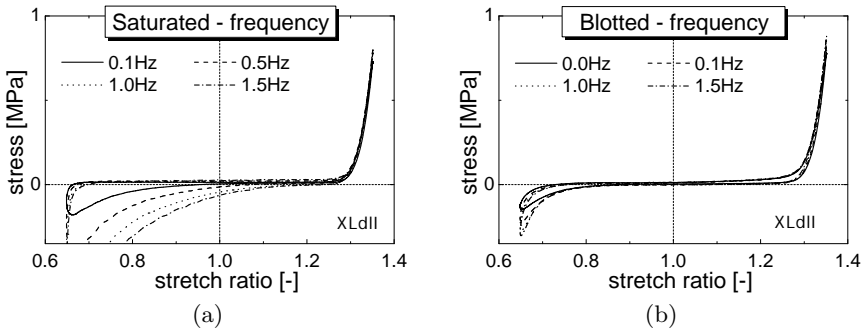
Figure 4.19: Comparison between the responses to various loading frequencies (100th cycles) in saturated (a) and blotted (b) conditions.

were likely due to the remaining bounded water that was still trapped in the ligament's ground substance.

Note: This kind of test shed light to the phenomena involved in the mechanics of the PDL. The overall response is the result of the interactions of two distinguished components: a porous solid matrix (i.e., collagen fiber, blood vessels, ground substance) and a fluid phase (i.e., blood, interstitial water) filling the pore space.

The solid matrix alone showed an almost perfectly non-linear elastic response, both in the tensile and compressive aspects. The dissipative process, observed mainly in the compressive response of the PDL, was found to be principally due to the *pore fluid – solid matrix* interaction during the deformation.
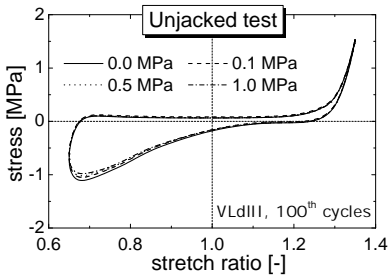
4.4.9 Unjacked tests

The mechanical responses of five specimens to the testing profile described on page 92 are shown in figure 4.20.
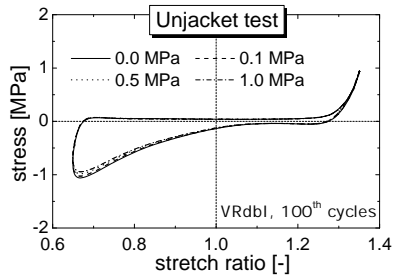
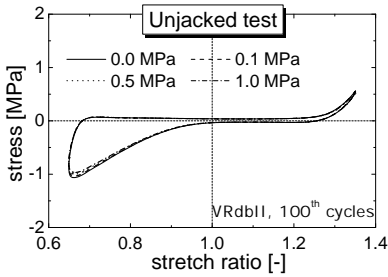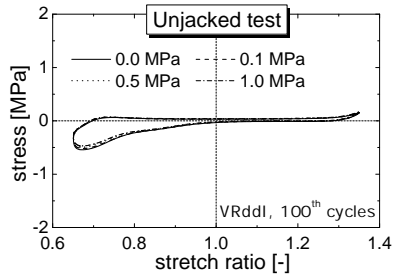The recorded data were pre-processed as to eliminate the load offset
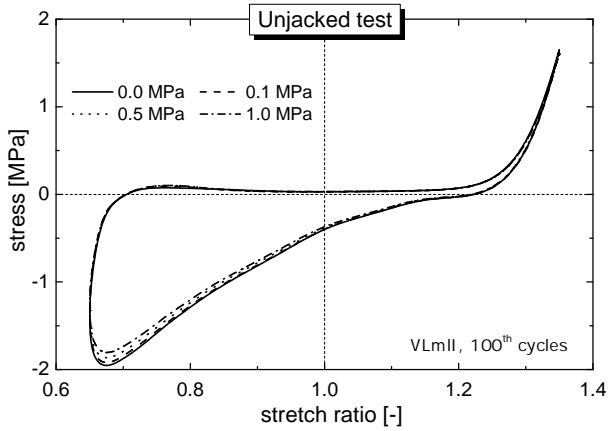
(a)

(b)

(c)

(d)

(e)

Figure 4.20: Effect of fluid pressure: unjacked tests at pressures p=0.0, 0.1, 0.5 and 1.0 MPa.

due to the sensitivity of the submersible load cell to the environmental pressure p (see figure 3.9 on page 82). Depending on the level of the chamber pressure p, the offset load $F_{SLC}(p)$ was subtracted to the recorded load $F_{meas}(t)$ to obtain the net load $F(t)$

$$F(t) = F_{meas}(t) - F_{SLC}(p) \qquad (4.25)$$

generated by the specimen and used to calculate the stress $T(t) = F(t)/A_0$, where A_0 is the initial PDL cross-sectional area.

Tensile and compressive behaviors

The parameters reported in table 4.16 were evaluated at the 100th cycles of every testing pressure profile. Their relative differences were assessed and averaged over the five specimens. This comparison clearly

Table 4.16: *Unjacked* tests: Differences in the mechanical parameters (means and standard deviation over 5 specimens) between the 100th cycles at the four testing pressure profiles.

Param.	0.0-0.1MPa 100th cycles [%]	0.1-0.5MPa 100th cycles [%]	0.5-1.0MPa 100th cycles [%]	0.0-1.0MPa 100th cycles [%]
T_t	-0.2±0.9	0.0±2.6	0.1±1.5	-0.1±4.8
T_c	-3.5±1.4	-3.6±0.9	-3.8±0.7	-10.5±2.3
E_t	-2.1±0.5	-5.2±2.3	-2.6±0.9	-9.6±3.2
E_c	-1.6±0.5	-3.2±0.5	-3.2±0.9	-7.9±1.6
α_{tl}	0.3±2.1	1.9±1.6	-0.2±0.9	2.0±3.7
α_{tu}	-0.5±2.2	-6.0±3.3	1.5±1.6	-5.2±3.8
α_{cl}	-0.2±4.9	0.1±5.4	-0.4±2.8	-0.4±10.8

showed that the increase of the chamber fluid pressure did not introduce any significant change in the mechanical response of the PDL. The progressive softening of the response, enhanced in figure 4.21, recorded during the compressive phase of the test could thus not be attributed to the increase of the fluid pressure.

The last 0.0MPa pressure test (triangles in figure 4.21) showed that the tendency was inverted, indicating that the change of pressure may play some role. However, this role can be assessed as not significant, as a variation of the environmental pressure by a factor 10 induced a maximal change factor of 1.1 in the measured parameters.
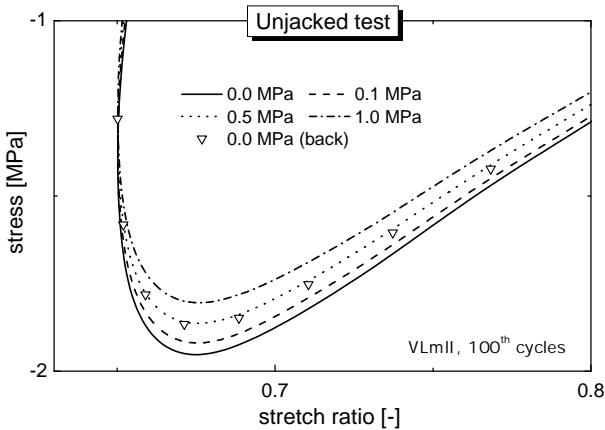

Figure 4.21: Effect of fluid pressure: enlargement of the responses for the compressive phase of specimen VLmlI (plot 4.20a). Triangles indicate the response obtained after the pressure was brought back to 0.0MPa.

Summary

This testing procedure allowed to test the PDL at different environmental pressure levels. The mechanical response not showing any dependance on this parameter, the following observations could be stated.

As it was qualitatively observed in section 4.4.5, the results obtained here quantitatively confirmed that the PDL mainly possess an

open type of porosity (i.e., the pores in the solid skeleton are interconnected, allowing for the fluid phase to flow through the porous solid matrix). In fact, if this would not have been the case, an increase of the environmental pressure would have induced evident changes, both geometric and mechanical (just like a rubbery balloon *decrease in size* and become *stiffer* when the external pressure is increased). Neither of these phenomena were observed, and the PDL reacted to a change of the external pressure as if it was an incompressible material. This was, however, in opposition with the results reported in section 4.4.5.

For these conditions to coexist, the only possible explanation was that the pores of the PDL were directly connected with the environmental pressurized fluid, so that the pore pressure could equal the external pressure without any geometrical changes. The PDL thus behaved in a very similar way to what is observed for soils or materials presenting an open type of porosity in general. In fact, the principle of *effective stress* proposed by Terzaghi [152] (see also section 2.3.2, page 49) to describe the mechanical behavior of porous soils, was verified by the reported results.

Von Terzaghi found that any change in p produced practically no volume changes and had practically no influence on the stress conditions for soil failure. In this same way, the results of this work showed that the pore fluid pressure did not produce any volume changes nor modify the mechanical response of the fibrous matrix. Interestingly, based on Terzaghi's findings, Skempton [133] reported that all measurable effects of change of stress (e.g., compression, distortion) were *exclusively* due to changes in the *effective stress*, operating on the solid matrix.

4.4.10   Jacked tests

The multiaxial loading of the PDL was obtained by wrapping the cylindrical specimen in a thin tubular membrane and by simultaneously applying axial displacement and lateral pressure to it.

The contribution of the membrane to the response to sinusoidal tests needed thus to be firstly quantified.

The three testing protocols described on page 93 were then executed on five specimens. Only four of them were retained, the fifth being discarded due to the failing of the sealing system during pressurization. Since the specimens all showed similar results (see appendix D), as a matter of clarity, only the curves obtained for the specimen WRdbI are presented in this section.

The data were pre-processed in the same way as explained for the *unjacked tests* (see page 141) as to eliminate the load offset due to the sensitivity of the submersible load cell to the environmental pressure p.

Contribution of the membrane

Figure 4.22 shows the responses (stress versus stretch ratio) at the 1000nd *normal* profile cycles of a specimen tested both without (solid) and with (dashed line) the tubular membrane wrapped on it. The response of the membrane alone is also superposed (open circles).
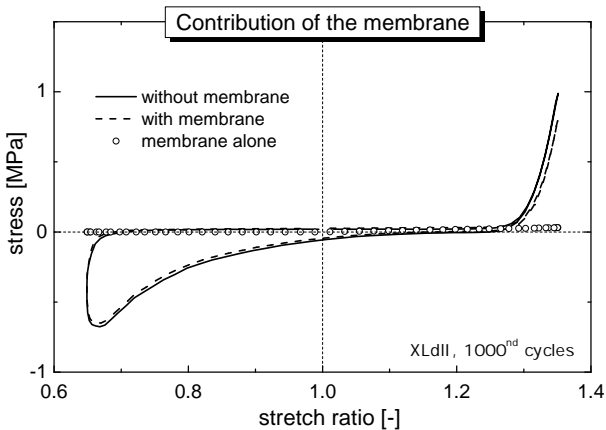

Figure 4.22: Contribution of the membrane to the mechanical response.

The differences in the parameters reported in table 4.17 between the tests without and with membrane (means and standard deviations over 4 specimens) showed that the contribution of the membrane was negligible for all the parameters except for the maximal tensile stress T_t, which slightly decreased. This observation was in opposition with what one could expect; as shown by the open circles, the addition of the thin layer of rubber should have slightly increased the stiffness of the specimen, increasing thus the maximal stress reached for a given maximal stretch ratio.

Table 4.17: Differences in mechanical parameters between tests with and without membrane.

Parameter	with - without membrane [%±SD]
T_t	**-36.4±0.8**
E_t	13.0±17.1
T_c	1.8±6.1
E_c	4.8±11.5
α_{tl}	-1.2±15.8
α_{tu}	-1.5±12.8
α_{cl}	7.4±13.6

The recorded opposite tendency was attributed to the manipulations to which the specimen was subjected in order to modify its level of saturation and complete the *jacked* tests; to allow for the membrane to be rolled and unrolled over the specimen indeed, the proximity bearing (part number 8 in figure 3.8 on page 79) could not be used during this type of test. Thus, when the chamber was first opened after the *Prec.* test (see table 3.4 on page 94) to unroll the membrane over it, the specimen could have been slightly sheared, tearing the fibrous matrix and resulting in the slight loss of maximal stress T_t.

***Over saturated* test**

Figure 4.23 shows the responses to the *over saturated* conditions at the cycles defined on page 94 and pressures levels 0.0, 0.1, 0.5 and 1.0MPa for specimen WRdbI.
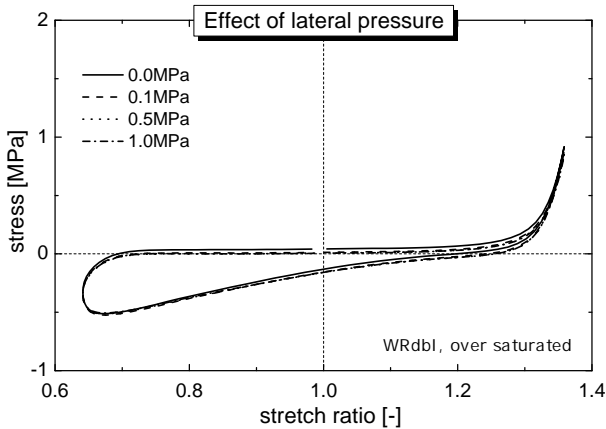

Figure 4.23: *Over saturated* test: the volume of pore fluid contained in the ligament was maximized prior sealing of the specimen and subsequent pressure increase. No apparent influence of pressure level on the mechanical response was observed.

As observed for the *unjacked* tests (see section 4.4.9), the variation of pressure seemed to have very little influence on the mechanical behavior of the ligament in these specific conditions. In fact, the comparison of the parameters reported in table 4.18 (average and standard deviation values over the 4 specimens) for the four pressure levels confirmed that the variations were negligible. The few differences recorded for the tensile parameters slightly exceeding the 20% (**boldfaced**), were in line with the results reported for the *saturated* and *partially saturated* tests (see further in this section).

Table 4.18: Differences in mechanical parameters (means and standard deviation over 4 specimens) between the 100th cycles of the four testing pressures for the *over saturated* conditions.

Param.	0.0-0.1MPa 100th cycles [%]	0.1-0.5MPa 100th cycles [%]	0.5-1.0MPa 100th cycles [%]	0.0-1.0MPa 100th cycles [%]
T_t	-0.3±6.9	15.5±15.1	5.3±5.6	**21.6±20.8**
T_c	2.1±4.2	-3.9±2.2	-2.1±1.5	-3.9±3.6
E_t	5.3±11.8	13.5±5.9	1.0±4.3	**21.3±21.4**
E_c	-3.5±3.2	-2.7±2.2	-1.7±1.0	-7.7±2.0
α_{tl}	-4.0±5.8	**-24.8±19.3**	0.6±15.5	**-28.0±20.8**
α_{tu}	-2.1±2.2	-1.8±4.5	-2.2±3.3	-6.0±6.2
α_{cl}	-4.3±8.4	-0.3±0.7	-1.8±4.8	-6.3±8.8

Since the PDL was saturated with saline when in its maximal stretched configuration ($\lambda = 1.35$), the quantity of fluid confined within the membrane during testing, was sufficient to fill the totality of the pore volume throughout the entire cyclic test. At $\lambda = 1.35$ all the fluid was filling the pore volume of the ligament. During the tensile unloading and the compressive loading phases of the cycles (i.e., for $\dot{\lambda} < 0$) the pore volume of the PDL decreased and the exceeding fluid, squeezed out of it, could take place between the specimen and the sealing membrane. This generated a sort of fluid *reservoir* which could be drawn back in the tissue during the compressive unloading and the tensile loading ($\dot{\lambda} > 0$) phases of the cycles. The changes of the environmental pressure were thus transmitted via the membrane to the incompressible trapped fluid, which completely filled the pore space at every instant of the cycling.

These conditions actually corresponded to the ones created for the *unjacked* tests (see section 4.4.9), but with the presence of the membrane. The obtained results were thus very similar.

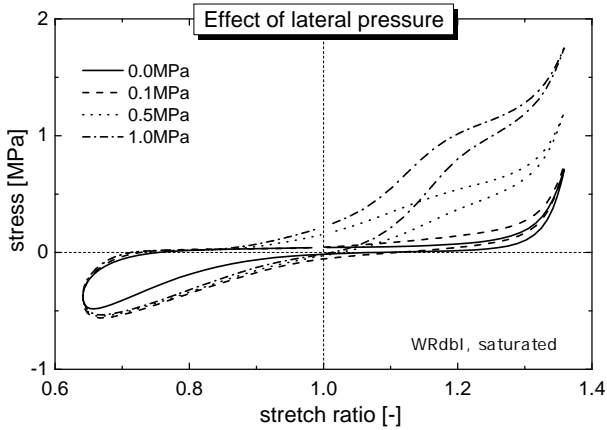**Saturated** and **partially saturated** tests

A fraction of the fluid contained in the over saturated PDL was then extracted following the procedure described on page 94. For the *saturated* test, the volume of fluid contained in the specimen was the quantity allowed to fill its pore volume when in its *zero* state.

Figure 4.24a shows the results obtained for such conditions, applied to the same specimen WRdbI. It was evident that the changes in the level of lateral pressure altered the (mainly tensile) mechanical response of the ligament.

In fact, in this case, the volume of fluid available within the membrane was not sufficient to completely fill the pore volume throughout the cycles. Only during the compressive phase the fluid volume was enough to fill all the pore space, and even create the fluid *reservoir*, as it was in the case of the *over saturated* test; the response did not vary much depending on the external pressure. This *reservoir*, however, was not enough to fill all the pore volume during the tensile phase. Thus, to guarantee equilibrium between external and internal water pressure, the compressible fibrous matrix underwent lateral deformation. The change in the geometry induced therefore modification of the axial stiffness of the specimen; the resulting effective stress T' only carried by the solid matrix clearly increased from the instant when lack of fluid forced a lateral neck-in (see also the video-recordings in the Jacked folder in the CD-ROM).

These phenomena were more pronounced in the case of *partially saturated* conditions (figure 4.24b), where the available fluid volume within the ligament was minimized. In these conditions the 0.0MPa test approached the behavior recorded for the blotted conditions (see figure 4.17); if the tensile phase did not show significant changes, the compressive one lost its clear hysteretic behavior.

In the case of higher pressure levels, the same processes exposed above were observed, showing up for this cases at lower stretch ratios. The *reservoir* was practically absent and the compressive phase was

(a)
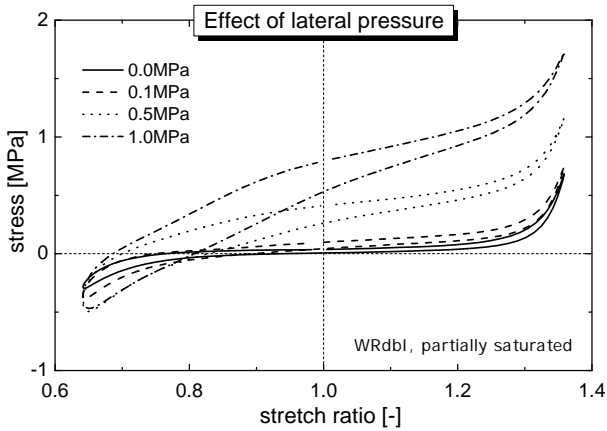
(b)

Figure 4.24: (a) *Saturated* test: volume of pore fluid at the PDL *zero* state ($\lambda = 1$). (b) *Partially saturated* test: volume of pore fluid at $\lambda = 0.65$. The pressure level had an evident influence on the mechanical response.

also affected by the changes of external lateral pressure.

Summary

It has been shown that the level of pore pressure did not affect by itself the mechanical response of the solid matrix of the ligament. Indeed, it is the combination of both level of saturation and fluid pressure that had a strong influence on the mechanical response to sinusoidal loadings.

On the one hand, when the pore fluid available during the mechanical loading of the PDL was enough to fill its pore volume for all deformed states, the stresses sensed by solid matrix did not vary much. On the other hand, a lack of pore fluid caused, depending on the applied lateral pressure, more or less marked changes on both tensile and compressive responses.

Since a direct quantification of these changes is out of the scope of this work, a more qualitative description was given. To this end, to complete the series of plots reported above, the corresponding curves obtained for the specimen WRdbI were grouped by pressure level an plotted in the graphs reported in figure 4.25 (refer to Appendix D for the curves obtained from the other specimens).

In plot 4.25a (0.0MPa) the results showed similar trends to those observed in the investigation on the fluid contribution to the mechanical response of the PDL: the smaller the quantity of fluid in the ligament, the lower was the lost of energy during compression. The tensile part of the cycle was unaffected.

From plot 4.25b (0.1MPa) it was observed that an increase of lateral pressure induced a slight increase of the stiffness of the specimen in the *zero region* in the case of *saturated* and *partially saturated* conditions.

This was evident at higher lateral pressures (0.5MPa, plot 4.25c and 1.0MPa, plot 4.25d), where the stiffness of the PDL showed clearly an increase around the *zero* state for the *saturated* (dashed line) and for even lower stretch ratio values in the case of *partially saturated* (dotted line) conditions.
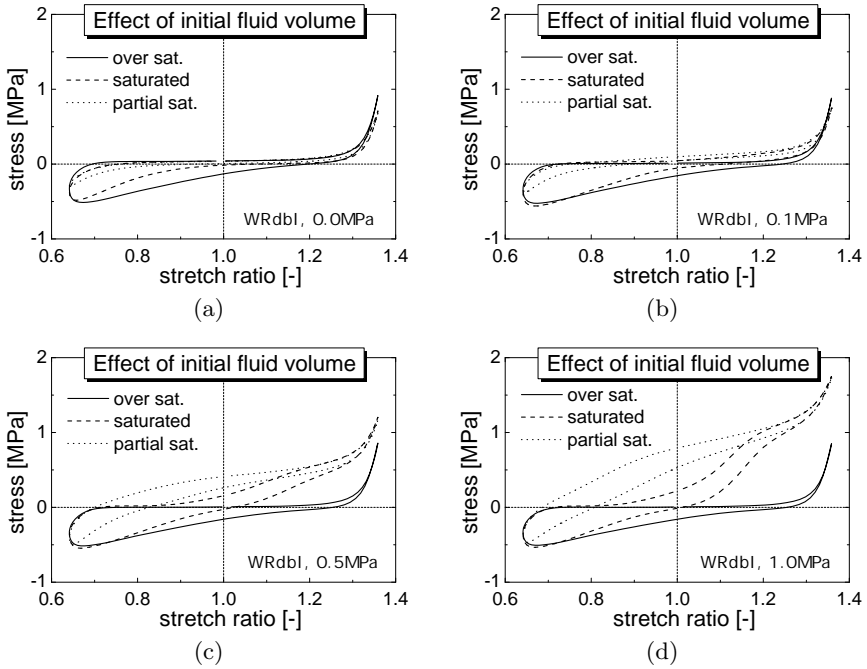
Figure 4.25: Effect of saturation: each plot show the curves recorded at a pressure level but for three different level of saturation.

Moreover, plots 4.25c and 4.25d show that, above a certain value of λ (in this case for $\lambda \gtrsim 1.2$) the responses to *saturated* and *partially saturated* conditions were superposed. Thus, it was suggested that the stress state of the PDL was comprised between two limiting cases:

- the *over saturated* case, for which the response was independent on the level of pore pressure;

- the fully *dried* case, for which the stress state depended on the level of fluid pressure.

The states in between are obtained by modification of the saturation

of the PDL.

The hypothesis that the increase in solid matrix effective stress and stiffness, when in *partial saturated* conditions, could be among the responsible processes of dental mobility was put forward. In fact, during orthodontic loadings a region of the PDL is in general subjected to high compression, such that only few space is left for the fluid phase (e.g., blood and interstitial ECM water). Any additional loading applied in these conditions (e.g., due to mastication or speaking) can thus introduce abnormally high variation of stress in this region of the PDL, which, by inflaming (i.e., swelling) tries to reestablish a physiological situation. Perhaps, activity of cells responsible for bone resorption (i.e., *osteoclasts*) is promoted by the combined effect of lack of fluid and loading perturbations.

In PDL regions subjected to tensile stress, instead, growth of alveolar bone, regulated by *osteoblast* activity, is probably mainly caused by the stress state induced in the alveolar bone by the stretched collagen fibers.

Chapter 5

Numerical Simulations

Clever people needn't be good; they can simulate

Anonymous

A finite element (FE) model of the periodontium was developed within the theoretical framework reported in chapter 2. The results of the simulations were then compared to the experimental observations described in chapter 4. Firstly, the material parameters describing the behavior of the solid matrix of the periodontium, emptied of its fluid content, were identified (section 5.1). Secondly, the fluid contribution to the mechanical response was accounted for by adding porosity and permeability properties to the solid matrix model (section 5.2).

All the modeling was developed using the software package ABA-QUS® 6.7 (Simulia, Rhode Island, USA) [55]. As pointed out in chapter 2, the modeling was based on already build-in constitutive behaviors, as the development of original laws was beyond the scope of this work.

For the FE model developed herein, the phenomena observed due to lateral confinement and partial saturation of the ligament (see section 4.4.10) were not considered.

5.1   The solid matrix

As established in section 4.4.8 (136), the mechanical response of the periodontium could be attributed to the interaction between a porous solid skeleton and the fluid flowing through its pores (see figure 4.17). Experimental results further showed that the solid matrix of the PDL, emptied of its fluid content, behaved as a

- porous (section 4.4.6)

- compressible (section 4.4.5)

- hyperelastic (section 4.4.8) material.

As opposed to the response including the fluid contribution, hyperelasticity could be assumed for both tensile and compressive loadings. In fact, the highly dissipative process observed in the case of fully *saturated* specimens, nearly completely vanished when the PDL was tested in *blotted* conditions (refer to section 3.7.3 for definition). Furthermore, still in the case of *blotted* conditions, the strong dependence of the response on the loading rate was much less pronounced. Based on these considerations, the assumption that the solid matrix of the PDL do not posses viscous behavior was made.

5.1.1   Model of the solid matrix

In general terms, the construction of a FE model requires the definition of (i) the geometry of the specimens, (ii) the mechanical behaviors of all of the materials involved, (iii) the spatial discretization (mesh) of the specimens' volume and (iv) appropriate boundary conditions.

(i) Geometry

The geometry for the numerical model was based on the dimensions of the specimens that were used to test the contribution of the solid matrix alone (i.e., in *blotted* conditions) to the total mechanical response of

Table 5.1: Geometry of the specimens used for the numerical models. d: diameter; w_0: PDL width; l_{bone}: length of bone part; l_{cem}: length of cemento-dentin part (see figure 5.1 for details).

Specimen	d [mm]	w_0 [μm]	l_{bone} [mm]	l_{cem} [mm]
VLdbI	5.78	805	1.5	1.5
VldbII	5.85	678	3.0	1.5
VLdlI	5.81	579	2.0	2.5
VRdlI	5.75	628	1.5	2.0
WLddI	5.81	638	2.0	2.5
Avrg	5.80	666	2.0	2.0

the periodontium (section 4.4.8, page 136). The values measured for these specimens are reported in table 5.1, where a geometry obtained by averaging the dimensions of the 5 specimens (Avrg) is assessed. Simulations were performed for all of these specimen geometries.

(ii) Mechanical behaviors

The two mineralized tissues were modeled as linear elastic materials, since no damage nor remodeling phenomena were involved in the experimental testing. Parameters for alveolar bone and cementum were retrieved form the literature [39, 57, 86, 94, 103, 120, 148] (see also table 1.1, page 28) and the retained values are reported in table 5.2.

Table 5.2: Material constants (Young's modulus E and Poisson's ratio ν) for bone and cementum.

material	E [MPa]	ν
alveolar bone	345	0.31
cementum	15000	0.31

Note: as discussed in chapter 2, the hypotheses of material *homogeneity* (identical mechanical properties in all material points) and *isotropy* (identical mechanical properties for all testing directions) were assumed for all the periodontal tissues.

In a recent study on the hyperelastic behavior of the PDL [130], it has been shown that, among several strain energy potentials, Ogden's potential (with $N = 3$) provided the best fit of the tissue's response to both tensile and compressive loadings. Based on this potential, the hyperfoam (hyperelastic behavior for elastomeric foams) strain energy potential (see chapter 2, equations 2.35 and 2.36), proposed among the ABAQUS [55] material behaviors library, was thus chosen as, in addition, it allowed for compressibility. This potential is defined as

$$W = \sum_{k=1}^{N} 2\frac{\mu_k}{\alpha_k^2} \left[\lambda_1^{\alpha_k} + \lambda_2^{\alpha_k} + \lambda_3^{\alpha_k} - 3 + \frac{1}{\beta_k}(J^{-\alpha_k\beta_k} - 1) \right]$$

where λ_i, $i = 1, 2, 3$, are the principal stretch ratios, μ_k, α_k and β_k are material constants (to be identified) and N is a positive integer defining the order of the strain energy potential. As pointed out in section 2.2.4, the material constants are related to the initial shear modulus μ_0 and to the Poisson's ratios ν_i via

$$\mu_0 = \sum_{i=1}^{N} \mu_i \qquad \text{and} \qquad \nu_i = \frac{\beta_i}{1 + 2\beta_i} \tag{5.1}$$

In this approach, the case $N = 1$ was considered. In such a situation, the constants (omitting the indices) μ, α and β have a direct physical meaning: μ represents the initial shear modulus and is identified as the slope of the stress-stretch ratio curve at the origin (i.e., for $\lambda = 1.0$); α describes the degree of non linearity of the curve; ν (related to β via equation 5.1) corresponds to the material's Poisson's ratio.

The material behaviors chosen for the periodontal tissues, with the corresponding material constants, are shown in table 5.3.

Table 5.3: Mechanical behaviors and corresponding material constants for bone, PDL and cementum.

material	behavior	constants
bone	linear elastic	E_{bone}, ν_{bone}
PDL	hyperfoam	μ, α, ν
cementum	linear elastic	E_{cem}, ν_{cem}

(iii) Mesh

The geometry of the specimens, the assumed homogeneity and isotropy, and the considered loading case, allowed for an *axisymmetric* formulation of the problem, which was based on 4-node bilinear axisymmetric quadrilateral elements (type CAX4).

A total, 3760 elements (1200 for both bone and cementum parts and 1360 for the PDL), corresponding to 3889 nodes, were used. The design of the mesh (see figure 5.1) was fine and uniform for the PDL and gradually coarse towards the extremities of the specimen.

(iv) Boundary conditions

The boundary conditions to which the specimens were subjected during the experimental tests, were integrated into the numerical model. The base of the cementum portion was held fix, while the displacement (1 cycle of a sinusoidal wave of frequency $f = 1.0$Hz and amplitude $A = 0.35w_0$) was imposed to the base of the bone part (see figure 5.1).

5.1.2 Identification of μ, α and ν

Table 5.3 shows all the material constants that need to be known for the modeling of the solid matrix behavior. Among these, the three parameters defining the behavior of the PDL remained to be identified.

To obtain the optimal set of parameters $s_{opt} = (\mu, \alpha, \nu)$ which best fitted the experimental curves, the non-linear least squares method was
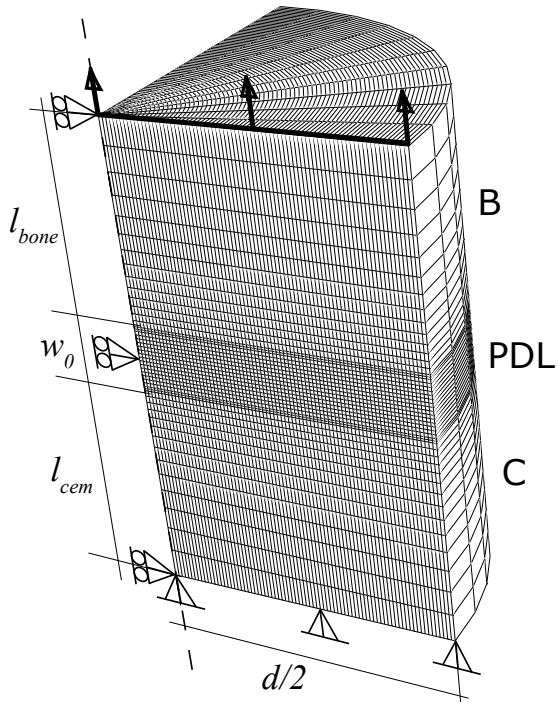
Figure 5.1: Geometry, mesh and boundary conditions for the numerical models. This 1/4 of cylindrical specimen was obtained from the revolution of the transversal section (defined by the dimensions l_{bone}, w_0, l_{cem} and $d/2$) around the axis of symmetry (dashed line). The base of the cementum (C) was held fix and the axis of symmetry not allowed for radial displacements. The displacement was uniformly applied (arrows) to the bone extremity (B).

used. Given an initial set of parameters $s_0 = (\mu_0, \alpha_0, \nu_0)$, its successive refinement was obtained iteratively by minimizing the value of

$$S_i = \sum_t (ERR_i(t))^2 \qquad (5.2)$$

representing the sum of the norms of the errors between experimental and simulated data for the ith iteration of the identification procedure. ERR_i was defined as the difference between the simulated load $F_{FE_i}(t)$, obtained with the parameter set $s_i = (\mu_i, \alpha_i, \nu_i)$, and the recorded load $F_{EXP}(t)$, normalized by the maximal recorded load F_t (see figure 5.2)

$$ERR_i = \frac{F_{FE_i}(t) - F_{EXP}(t)}{F_t} \qquad (5.3)$$

Successive sets s_{i+1} were assessed as $s_{i+1} = s_i + \Delta s_i$, where the shift vector Δs_i was calculated via the Levenberg-Marquardt algorithm (based on the steepest descent criterion). The optimal set s_{opt} was obtained when $\|\Delta s_i\| < 10^{-3}$.

The responses obtained from the five specimens, and their average curve, were used as objective data for the identification procedure.

Note: This iterative procedure was carried out with the non-linear least squares problem solver (lsqnonlin) of the software package Matlab® (The MathWorks, Natick, Massachusetts, USA).

5.1.3 Results

The experimental and simulated responses in the case of the specimen VLdbI are shown in figure 5.2 (the plots for the other specimens can be found in the appendix E).

The compressible hyperelastic model proposed herein proved thus to be adequate for the description of the mechanical behavior of the solid matrix of the PDL, when emptied of its fluid phase.
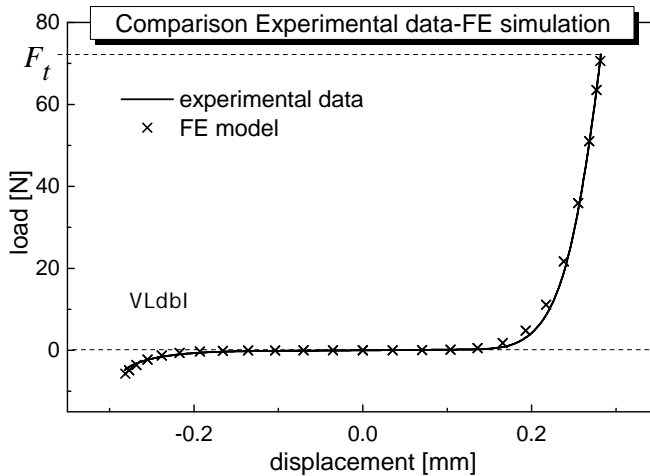
Figure 5.2: Comparison between the experimental data and the numerical simulation for the solid matrix response.

Solving strategy

The resolution of non-linear equilibrium equations was based on the *Newton's method*, allowing for a fast convergence to the solution [55]. Moreover, to obtain sufficient accuracy, a maximal time increment of $\Delta t = 0.01$s (resulting in a minimum of 100 steps per cycle) was chosen.

Since the hyperfoam model is not intrinsically stable for all combination of parameters, the limiting loading configurations for which the model became unstable were checked via the Drucker stability criterion. Among all the checked loading conditions tested numerically, restrictions were only found in the case of biaxial and volumetric compressions, for which the nominal strain and the volume ratio had not to be less than -0.44 and 0.57, respectively. The maximal axial com-

pression imposed to the model being of $35\% w_0$, these limits were not exceeded.

Values of μ, α and ν

The values obtained from the identification procedure on the five specimens, plus the average specimen Avrg, are reported in table 5.4. Mean

Table 5.4: Material constants of the PDL for the five and for the average specimens.

Specimen	μ [MPa]	α	ν
VLdbI	0.001348	50.17	0.29
VldbII	0.001205	49.01	0.31
VLdlI	0.001476	32.07	0.28
VRdlI	0.001832	48.12	0.31
WLddI	0.001074	32.85	0.31
Avrg	0.001502	35.21	0.29
mean	0.014±18.8%	41.24±21.1%	0.30±4.5%

values and standard deviations (in percent) are also shown.

Sensitivity

The sensitivity to the initial parameter set s_0 was also tested to verify the existence of a unique set of parameters for which the error was minimized. To this end, three different sets of initial values were tested. The values of μ, α and ν obtained for the specimen WLddI were varied as reported in table 5.5 (variation in % of the original values) to obtain the three sets of initial parameter (–□–, –◯– and –△–).

The evolution of these values with the number of subsequent iterations is shown in figure 5.3. All of the parameters converged after a few iterations towards the original set of values. The confidence intervals, calculated as percent deviation from the original parameter values shown in table 5.4 for WLddI, were of ±13.6%, ±1.5% and ±0.4% for μ, α and ν, respectively.

Table 5.5: Initial set of material parameters for the sensitivity test. Values are percent of the values reported in table 5.4 for WLddI. See also figure 5.3

WLddI	μ [%]	α [%]	ν [%]
–□–	93	61	97
–○–	140	122	101
–△–	47	31	83

It can be noticed how ν converged only once the parameters μ and α reached their final values.

5.2 The solid matrix - pore fluid coupling

The numerical model described for the identification of the material parameters of the PDL's solid matrix was modified to account for the fluid phase. To this end, the Transient consolidation parameter of the *Soils option of ABAQUS was used. Such an analysis required the definition of the parameters describing a porous matrix filled with a fluid phase: porosity, permeability and fluid mechanical properties had to be included in the model for all of the involved tissues.

In this study, the *saturated* conditions (refer to page 91) were imposed as environmental conditions for the numerical model.
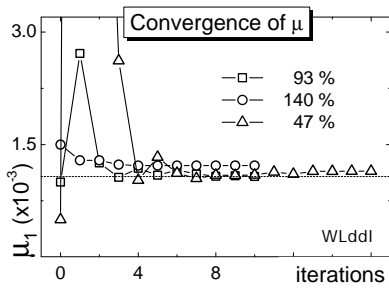
5.2.1 Model of the saturated periodontium

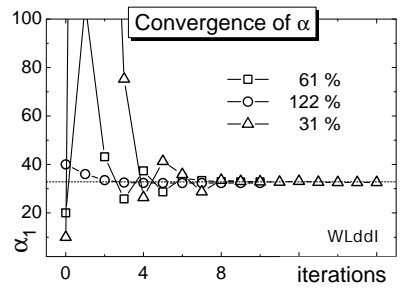The same scheme presented in section 5.1.1 is followed for the description of the porous model.

(i) Geometry

The geometry for the porous model was obtained as the average over the dimensions of 17 specimens which were all tested with the same
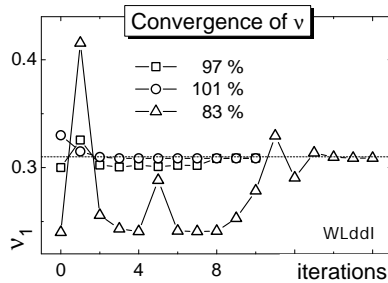
Figure 5.3: Convergence towards the unique solution (dotted line) of μ (a), α (b) and ν (c) for three sets of initial values (specimen WLddI). Legends indicate the the difference of the initial values with respect to the values shown in table 5.4 for specimen WLddI.

normal loading profile and *saturated* conditions. The values obtained are reported in table 5.6.

Table 5.6: Geometry of the specimens used for the porous model. d: diameter; w_0: PDL width; l_{bone}: length of bone part; l_{cem}: length of cemento-dentin part.

Specimen	d [mm]	w_0 [μm]	l_{bone} [mm]	l_{cem} [mm]
Average	5.80	585	2.0	2.0

(ii) Mechanical behaviors

The same mechanical behaviors, i.e. elastic for bone and cementum and hyperfoam for the PDL, used for the solid matrix, were kept for the porous model. In addition, porosity and permeability properties were defined for the three materials.

In ABAQUS, the porosity n is expressed via the void ratio $\bar{e}$ defined as

$$\bar{e} = \frac{n}{1-n} \tag{5.4}$$

The values of n (see table 5.7) were obtained from the literature for bone and cementum [9, 31, 115, 149, 153] , and measured for the PDL (section 4.4.6).

Table 5.7: Porosity n and corresponding (see equation 5.4) void ratio $\bar{e}$ for bone, PDL and cementum.

material	n	$\bar{e}$
bone	0.2	0.25
PDL	0.69	2.33
cementum	0.04	0.04

Permeability defines the ease with which a fluid can percolate through a solid matrix. As shown by Darcy's law (equation 2.41), the flow **q** depends on the permeability tensor **k**, which, assuming isotropy, is completely defined via a permeability constant k. Furthermore, permeability can depend on porosity n via the Kozeny-Carman equation 2.42. Thus, when porosity changes occur during mechanical deformation, permeability is affected.

Compared to the PDL, bone and cementum both undergo very small strains. Their porosity was then assumed to be constant during loading. The permeability values, measured as *hydraulic conductivity* k_s in section 4.4.7 (remind that $k_s = k \cdot \gamma_w$, where γ_w is the specific weight of the wetting fluid), were retained as constant for bone and cementum (see table 5.8).

Table 5.8: Permeability values for bone, PDL and cementum.

material	k_s [mm/s]
bone	5.27×10^{-4}
PDL	$k_s(\bar{e})$
cementum	3.87×10^{-7}

For what concerns the PDL, however, due to its high compressibility and large deformation capabilities, porosity, thus void ratio, was assumed to vary during mechanical loading. It has been experimentally proved that, for soft tissues, permeability is highly strain-dependent when finite deformations are involved [59]. Exponential constitutive laws relating k_s to $\bar{e}$, of the form

$$k_s(\bar{e}) = k_0 \left[\frac{\bar{e}(1 + \bar{e}_0)}{\bar{e}_0(1 + \bar{e})} \right] \exp \left[M \left(\frac{1 + \bar{e}}{1 + \bar{e}_0} - 1 \right) \right] \qquad (5.5)$$

where k_0 and $\bar{e}_0$ are the permeability and the void ratio at zero strain, respectively, and M a material constant, have been proposed [4, 131]. Since the difficulties encountered in the experimental determination of

the permeability of the PDL, the constant k_0 and M had to be identified with the numerical model, with $\bar{e}_0$ corresponding to the value reported in table 5.7 for the PDL.

Eventually, the model required the definition of the specific weight of wetting fluid, which, for simplicity, was that of water at room temperature

$$\gamma_w = 9.965 \times 10^{-6} \quad \text{N/mm}^3 \tag{5.6}$$

(iii) Mesh

The backward difference operator, used in ABAQUS for the integration procedure in consolidation analyses, introduces a relationship between the minimum usable time increment Δt and the element size Δl [55]

$$\Delta t > \frac{\gamma_w}{6Ek}\Delta l^2 \tag{5.7}$$

where γ_w is the specific weight of wetting fluid, E is the Young's modulus of the porous material and k is its permeability. The backward difference operator provides unconditional stability, so the only concern with respect to time integration is the accuracy, unless non-linearities cause convergence problems [55]. Provided the time increment is sufficiently large, a unique solution is obtained. If smaller time increments are needed, as it was for the present case, *spurious oscillations* (non-physical artifacts) may appear in the solution, leading to convergence problems. In this case, a finer mesh is required. This restriction resulted in the mesh shown in figure 5.4 (also used for the solid matrix model of section 5.1.1).

Concerning the type of element, a 4-node axisymmetric quadrilateral, bilinear displacement, bilinear pore pressure element (CAX4P) was chosen.

(iv) Boundary conditions

In addition to the boundary conditions used for the solid matrix model, a fluid pressure of $p = 0.0$MPa was imposed on the external surface of the specimen (see figure 5.4). Moreover, the imposed displacement corresponded to a 2 cycles of *normal* loading profile. Only the response curve obtained from the second cycle was used for the comparison with the experimental data. The reason for this, was that, during the beginning of the tensile loading of the first cycle, the porous model showed a transient response which vanished for the subsequent loading cycles.

5.2.2   Identification

It soon became evident that the strong (material and geometrical) non-linearities of the problem were important drawbacks for the convergence of the calculation. Indeed, by keeping the parameters identified for the hyperfoam solid matrix (section 5.1.3), and by imposing to the model a *normal* loading profile, the calculation could not converge. Difficulties in the resolution of the coupled hydro-mechanical equilibrium equations (refer to equations 2.58 – 2.61) were mostly encountered during the transition from the compressive to the tensile phase (i.e., around the end of the 1st or the beginning of the 2nd cycle).

The shear modulus μ, which defined the initial slope of the curve (were convergence problems were encountered), was thus increased until convergence of the calculation was obtained. The two other parameters of the hyperfoam model (i.e., α and ν) were adjusted to still obtain a good match between experimental and simulated data.

Moreover, only an averaged response (see figure 5.5), calculated over 17 specimens (all subjected to the same *normal* loading profile in *saturated* conditions) was used as experimental curve to be identified. Indeed, such a mean curve presented less severe conditions, in terms of maximal and minimal loads reached during the tensile-compressive cycles, so that an initial set of parameters, for which stability was ob-
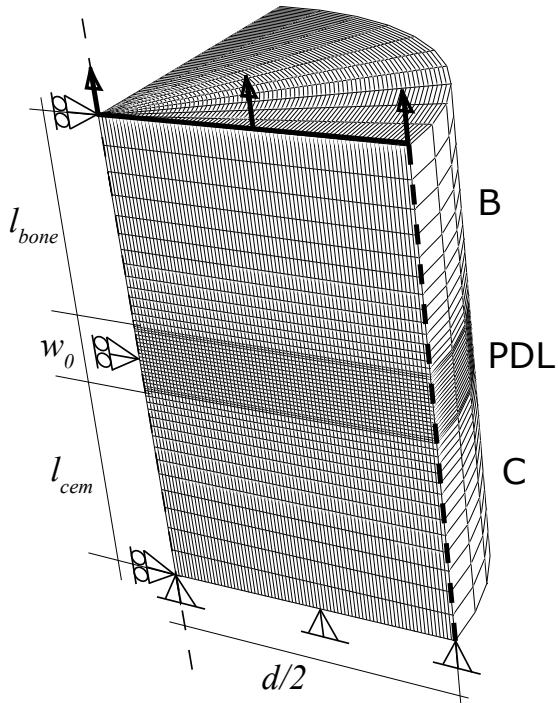
Figure 5.4: The geometry, mesh and boundary conditions were the same of the ones used for the solid matrix model. In addition, a fluid pressure $p = 0$ was imposed on the external surface of the specimen (bold dashed line).
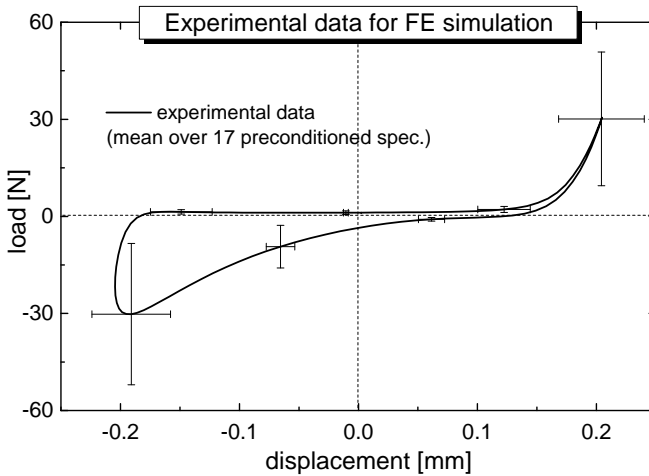
Figure 5.5: Experimental mean curve and standard deviation (bars) for identification of solid-fluid model parameters.

tained, was more easily identified.

The same procedure described in section 5.1.2 was then used for the identification of the parameters defining the porous model. 5 parameters (the 3 defining the hyperfoam behavior and k_0 and M defining the permeability function 5.5) were identified. During the iterative process, however, occasional instability, generally at some time increment around the compressive-tensile transition, occurred for some combination of parameters, causing the iterative optimization process to fail. Although Drucker stability criterion was still globally satisfied, local instabilities were probably the cause of such a behavior. Sensitivity to the initial set of parameters could thus not be achieved.

5.2.3 Results

The experimental (average of the response of 17 specimens) and the simulated curves are shown in figure 5.6. The calculated curve was obtained from an identification procedure for which the optimization process was completed.
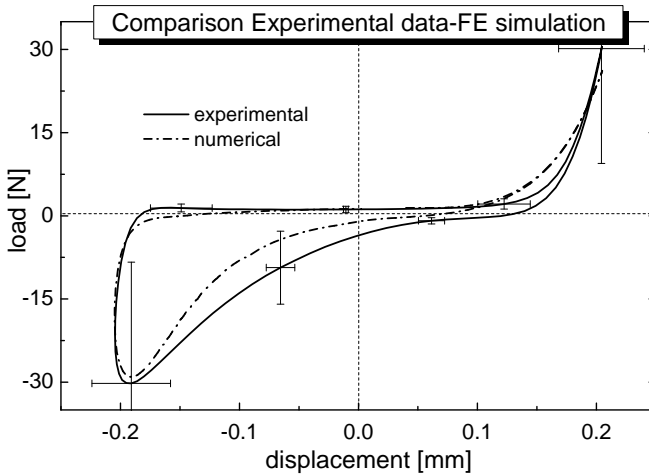

Figure 5.6: Experimental mean curve – Numerical solution comparison for the solid-fluid model.

It was noticed that the calculated response, well within the experimental standard deviation limits, fitted reasonably well the experimental curve. The tensile-compressive dissimilarities were well captured by this model based on hydro-mechanical coupling.

As a consequence of the forced increase of the initial shear modulus μ, needed for stability reasons, the tensile phase of the response was in general overestimated by the model. For the early compressive loading phase, instead, the response was underestimated. In this case, the

172

difference could be attributed to both the lack of viscoelastic properties and to the shape of the permeability function (see below).

Solving strategy

In non-linear problems, the objective is to obtain convergence of the solution with a minimal computational cost. As default, ABAQUS uses the *Newton's method* [55] to solve non-linear equilibrium equations. The main advantage in using this method reside in its quadratic convergence rate. Nevertheless, for models with large number of degrees of freedom, the computational effort that this method requires is important. In fact, the Jacobian matrix of the system needs to be formed and solved at each iteration.

An alternative to this method is the *quasi-Newton method*. In this solving strategy, the jacobian matrix is only occasionally completely calculated, but rather updated along iterations, such that it approaches its exact value as the iterations proceed. The method proposed in ABAQUS (the BFGS method, see [55]) is computationally inexpensive for the jacobian matrix updates as it results in simple inner products of vectors.

Furthermore, the robustness of the *quasi-Newton's method* can be improved by the use of the *line search* algorithm. When large residuals are obtained during the equilibrium iterations, this algorithm applies a scale factor to the computed solution correction, helping thus to prevent divergence.

Thus, *quasi-Newton's method* and *line search* algorithm were used for the resolution of the equilibrium equations.

Values of the material parameters

The material parameters used to obtain the curve shown in figure 5.6 are reported in table 5.9. The permeability curve, resulting from the relation 5.5, is illustrated in figure 5.7.

In a comparison of numerical simulations and experimental results,

Table 5.9: Material parameters identified for the porous model. The fluid specific weight was $\gamma_w = 9.965$ N/mm for all of the defined materials.

	E [MPa]	μ [MPa]	α [—]	ν [—]	$\bar{e}_0$ [—]	k_0 [mm/s]	M [—]
bone	345	—	—	0.31	0.25	5.27×10^{-4}	—
PDL	—	0.030	20.9	0.257	2.33	8.78×10^{-5}	14.2
cem.	15000	—	—	0.31	0.04	3.87×10^{-7}	—

Natali et al. [94] evaluated k_s^{PDL} in the order of 10^{-4} to 10^{-3} mm/s. This study was however limited to small strains only and k_s^{PDL} was considered as constant with stretch ratio, thus with porosity. Other works [4, 131, 156] on similar tissues (e.g., inter-vertebral disk) reported permeability values ranging from 10^{-9} to 10^{-5} mm/s. The work by van Driel et al. [148] also proposed PDL permeability values from numerical identification. The best results were obtained by assigning a permeability of 10^{-7} mm/s to 21% of the ligament volume, and a permeability of 10^{-10} mm/s to the remaining volume.

As noted, the values of the permeability function obtained herein were in line with the values proposed in other study.

Evolution of void ratio and fluid velocity

The evolution in time, over the second loading cycle, of the imposed displacement and of the calculated load response are plotted in figure 5.8a. Figure 5.8b shows the corresponding evolutions of the maximal, mean (average over all the PDL elements) and minimal void ratio values of the PDL.

In average, the void ratio of the PDL was proportional to the displacement and varied in a sinusoidal manner around a mean value of $\bar{e}_0 = 2.33$ and with an amplitude of $A = 1.10$. By looking to the extrema values, however, rapid fluctuations of $\bar{e}$ could be observed for $1.06 < t < 1.10$ and $1.55 < t < 1.65$. The flux exchanged between the PDL and the surroundings, also showed rapid variations at these same
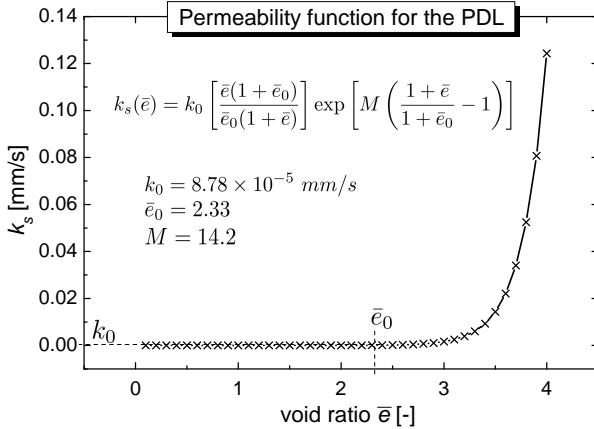
Figure 5.7: Permeability function for the PDL.

time ranges (see in the Fluid_Flow folder in the CD-ROM), and the calculation required further reduction of the time increment to obtain convergence.

Fluid velocity profiles are reported in figure 5.9 at 5 different times along the second loading cycle. In these schemes, only the boundaries of the PDL with alveolar bone (upper), cementum (lower) and environmental water (right boundary) are presented. It can be noticed how the fluid exchange between PDL and alveolar bone was remarkable, whereas exchanges with cementum were practically negligible.

In the early steps of the tensile loading phase (figure 5.9a), in fact, the increasing PDL pore volume was filled with fluid coming from the bone portion. Subsequently, at about the maximal extension (5.9b), the main fluid flow came directly from the external environment (through the right boundary), from where it was equally expelled during the
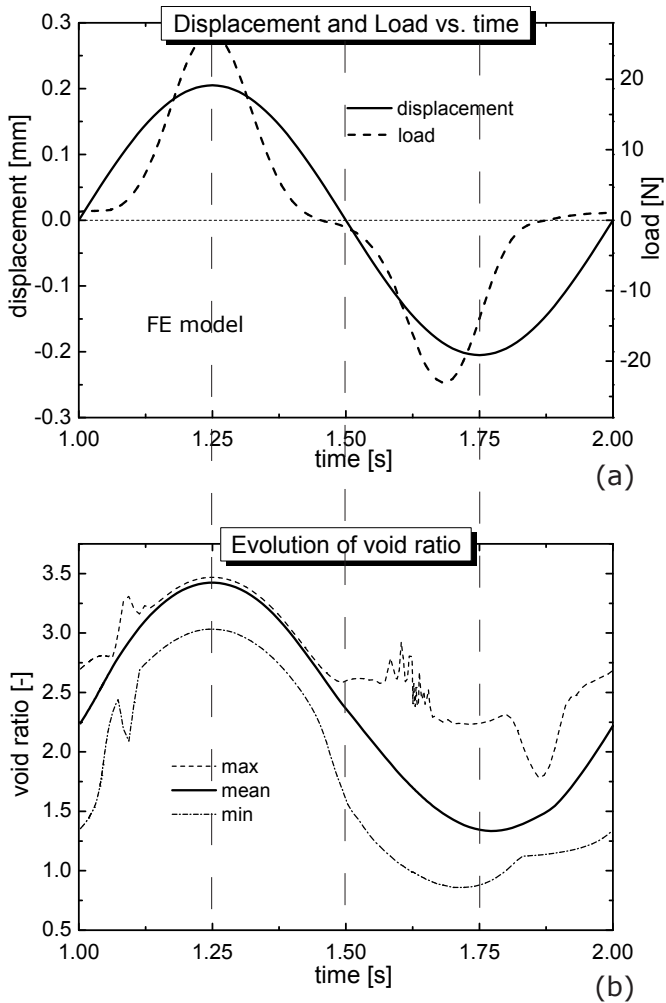
Figure 5.8: Evolution of displacement, load (a) and void ratio (max,mean and min) (b) during the second cycle of the FE model.
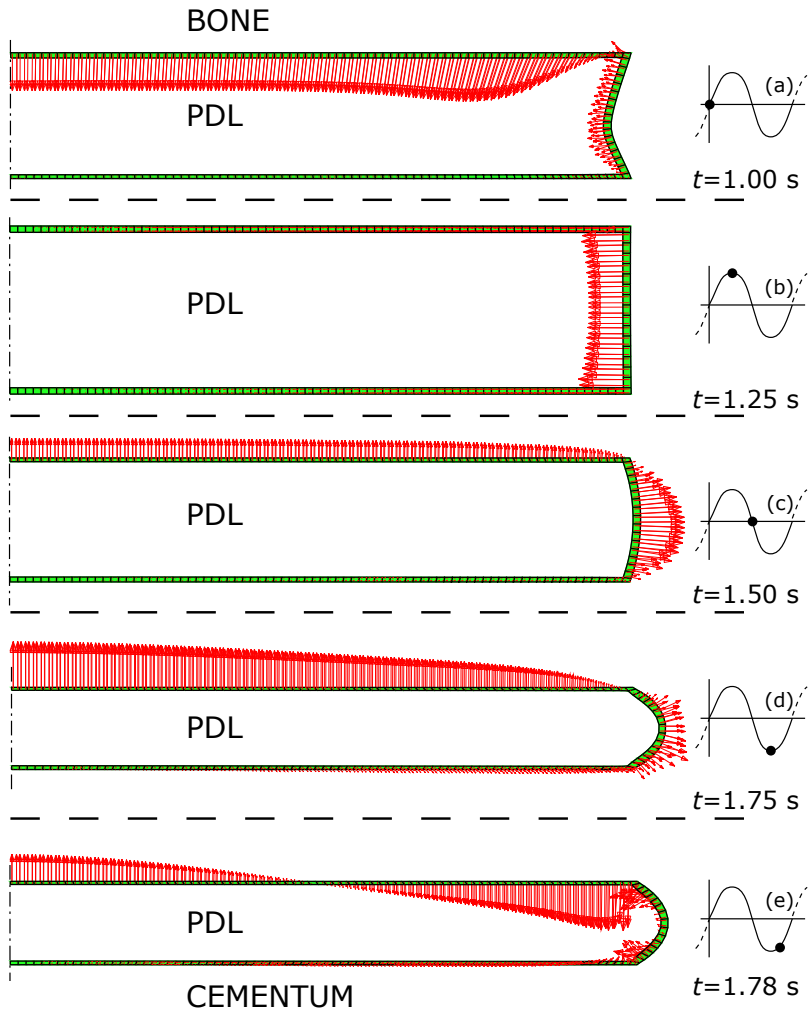
Figure 5.9: Fluid velocity at different times during the second cycle of the FE model.

tensile unloading phase. Approaching the tensile-compressive transition (5.9c) the external surface of the PDL progressively diminished and its fluid expelling capacity reduced. The excessive fluid was thus forced back into the bone until maximal compression (5.9d). During the unloading process of the compressive phase (5.9e), the fluid flow between PDL and bone gradually inverted and eventually the situation of figure 5.9a was recovered.
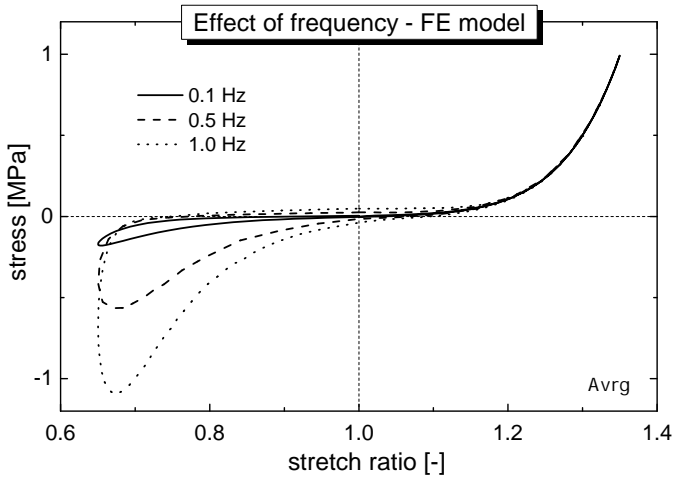
Effect of loading frequency

The response of the model was also evaluated for the different loading frequencies used in the experiments (i.e., 0.1Hz, 0.5Hz, 1.0Hz and 1.5Hz). The experimental curves and the calculated responses are compared in figure 5.10 (figure 5.10a recall the experimental curves of specimen URdbI —from figure 4.14— for comparison). With the set of material parameters given in table 5.9, the calculation could easily converge for the frequencies 0.1 to 1.0Hz, but instability occurred for 1.5Hz loading frequency. It was nevertheless noticed that the behavior observed during the experiments was well captured by the model. Indeed, while the tensile response was practically unaffected by the loading rate, the compressive part highly depended on it.

By evaluating, for the different numerical responses, the differences in the compressive parameters T_c and E_c (the maximal compressive stress and dissipated energy), and comparing them (table 5.10) with the ones obtained for the experimental curves (also in table 4.8), it can be observed that the model underestimated the compressive response. In fact, the differences between the calculated responses were at least twice as big as the measured ones. This difference can be attributed to the complete lack of time-dependent properties (viscoelasticity) in the proposed model of the solid matrix.
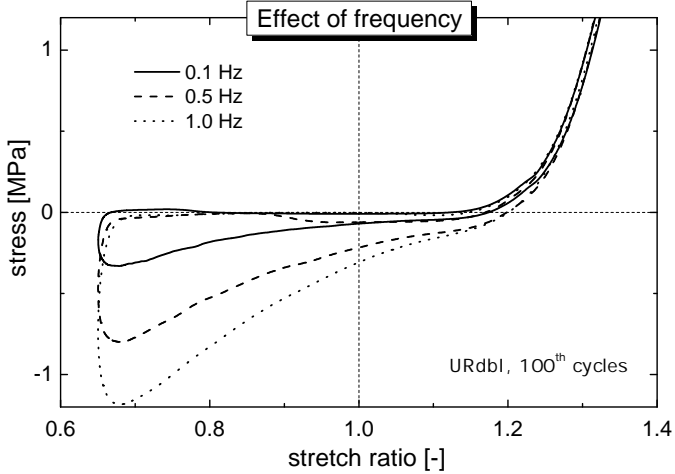
(a)

(b)

Figure 5.10: Experimental curves (from figure 4.14, without frequency 1.5Hz) (a) and numerical simulation of the effect of the loading frequency (b) on the axial stress.

Table 5.10: Comparison of the differences in the mechanical parameters obtained at different testing frequencies for experimental and simulated curves. Note: the calculation at 1.5Hz did not converge.

Param.	0.1-0.5Hz [%]	0.5-1.0Hz [%]	1.0-1.5Hz [%]
Experimental			
T_c	**106.8**	**44.9**	**27.1**
E_c	**125.4**	**48.8**	**27.6**
Numerical			
T_c	**215**	**92**	—
E_c	**532**	**90**	—

5.2.4 Summary

The two numerical models presented herein allowed for a good representation of the mechanical behavior of the periodontium when tested in two different environmental conditions:

- The mechanical response of the solid matrix emptied of its fluid phase (i.e., *blotted* conditions) was successfully modeled by considering the bone and cementum parts of the specimen as linear elastic materials and the PDL layer as a compressible hyperelastic medium. All of the tissues were considered as homogeneous and isotropic.

- The fluid contribution to the response was then integrated by extending the solid matrix model to a coupled hydro-mechanical problem. Equilibrium equations and constitutive relations for the fluid phase were included in the model and parameters such porosity and permeability were added for all of the periodontal tissues.

  In spite of some instability problems, this model furnished a good qualitative description of the mechanical response of saturated

specimens. In fact, characteristics like large tensile-compressive asymmetries and important compressive strain rate dependency were well captured within this theoretical framework.

As clearly shown in figure 5.9, important fluid exchanges at (i) the PDL-bone and (ii) the PDL-environment boundaries were observed. On the one hand, the first exchanging interface well described the possible *in-vivo* fluid flow occurring between PDL and alveolar bone in reason of the so called *perforating arteries*, allowing for the PDL blood supply. On the other hand, the fluid exchanged through the external surface of the specimen was not representative of *in-vivo* conditions, where no *free* boundaries are found. Thus, geometric and hydraulic resistances should be integrated in the model to confine the specimen and to approach more realistic conditions.

Chapter 6

Conclusions and Perspectives

Begin thus from the first act, and proceed; and, in conclusion, at the ill which thou hast done, be troubled, and rejoice for the good.

Pythagoras, 582 BC–497 BC

The main results obtained in this work on the mechanical behavior of the periodontium are resumed hereafter (section 6.1). Conclusions and guidelines for possible future works are given in sections 6.2 and 6.3, respectively.

6.1 Summary

Refer to figure 6.1 (on page 187) for an overview at a glance of the main results obtained in this work.

6.1.1 Histo-morphology

Histo-morphological studies were performed on *undecalcified ground* sections and on *decalcified semi-thin* sections.

By means of computed *image analysis*, site specific blood vessels (BV) *densities* (area and numerical fractions) and *dimensions* (diameters) were assessed. The PDL *width* w_0 was also extracted from such an analysis. Eventually, *roughness* of the PDL boundaries with alveolar bone and cementum were quantified via a *fractal analysis*.

183

Qualitative investigation on the distribution pattern of the *collagen fibers* (CFs) was performed using *polarized light* microscopy.

Results: The bovine PDL was characterized by a high degree of heterogeneity (due to the presence of large BV) and anisotropy (due to the presence of CFs). Its structural pattern resulted to be unpredictable among position along the roots in aspects such ligament width, BV density, CFs density and orientation, roughness of boundaries with bone and cementum.

6.1.2 Mechanical testing

Classical *flat* specimens were used to assess the dependance of the mechanical response of the periodontium on *site* of extraction. Sinusoidal 1.0Hz displacement profiles were applied to the specimens to simulate the *physiological masticatory stimulus*. Material parameters like extremal stresses and stretch ratios, phase lags, hystereses and degrees of non-linearity (Fung's type) were used for the analysis of the response.

New protocols were established for the extraction and for the testing of periodontal *cylindrical* specimens. The pertinence in using of such new specimens for a mechanical characterization of the PDL was checked via a direct comparison with mechanical parameters obtained from classical *flat* specimens.
A new testing system, the *pressure chamber*, was designed and build to allow for *multiaxial testing* of the new cylindrical specimens.
Experimental investigation performed on cylindrical specimens enhanced phenomena related to: (i) long lasting cycling; (ii) non-mechanical tissue's degradation; (iii) effect of loading frequency; (iv) pore fluid flow through the tissues; (v) tissue's compressibility; (vi) porosity and permeability; (vii) fluid phase contribution to the mechanical response; (viii) effects of multiaxial loading.

Results: Despite the high degree of bio-variability, no significant dif-

ferences were recorded in the mechanical parameters assessed for flat specimens coming from different locations around the tooth.

The new cylindrical specimens geometry and the new testing system proved to be adequate for the mechanical investigation on the bovine PDL. The various tests performed showed that: (i) steady response to cyclic tensile-compressive loadings was reached only after long pre-conditioning; (ii) effects of non-mechanical degradation were negligible during testing; (iii) distinct mechanical behavior were observed for tensile and compressive loadings; in tension the PDL behaved as a pseudo-elastic material, whereas in compression it rather behaved as a pseudo-plastic viscous media; (iv) during cyclic loading, important fluid exchanges between the specimens and the environment were observed; (v) the PDL behaved as a highly compressible material; (vi) a fluid phase could flow, with more or less ease, through the open pores of the solid matrix of the tissues involved (i.e., alveolar bone, PDL and cementum); (vii) the overall response of the periodontium was the superposition of the mechanical contribution of a porous solid matrix (carrying loads mostly for tensile loading) and of a fluid phase flowing through its pores (mostly reacting to compressive loading); (viii) multiaxial loading (axial loading and lateral hydrostatic confinement) introduced discernible changes in the response of the solid skeleton only when the tissues were in partially saturated conditions.

6.1.3 Numerical simulations

FE models were constructed to analyze the mechanical response of periodontal specimens when in (i) *blotted* (i.e., with no fluid phase within the porous matrix) and (ii) fully *saturated* (i.e., when the pore volume is entirely filled with fluid) conditions. The PDL's material parameters that could not be experimentally assessed were identified such as the numerical response approached at best the experimental one.

Results: A compressible hyperelastic material model well described the response of the PDL in the (i) *blotted* conditions. The contribution

of the fluid phase was accounted for by (ii) extending this model to a coupled hydro-mechanical problem. Although a quantitative analysis could not be performed, this model furnished a pertinent qualitative description of part of the observed phenomena.

6.2 Concluding

Alveolar bone, periodontal ligament (PDL) and cementum, makes up a unique functional system called *periodontium*. From both biological and mechanical standpoints, these three tissues are strictly connected the ones to the others. In fact, remodeling processes of bone and cementum, allowing for dental growth and mobility, are promoted by cellular activity, which is thought to be initiated by changes in the mechanical stress distribution and/or fluid movements within these tissues. Because of these strong connections, it has been suggested that the bone-PDL-cementum system be regarded as an elementary unit when the description of its mechanical behavior is investigated.

At a microscopic scale, the structure of the periodontium is heterogeneous and anisotropic.

At a macroscopic scale, the mechanical properties of the periodontium are rather independent on the position along the roots.

The mechanical response of the periodontium to cyclic tensile-compressive loadings results form the coupling of the mechanics of its porous solid matrix and the fluid phase flowing through it, since important fluid exchanges can take place between and within its tissues.

6.3 Continuation

Further effort in the investigation of the mechanical behavior of the periodontium should be addressed to both experimental and theoretical
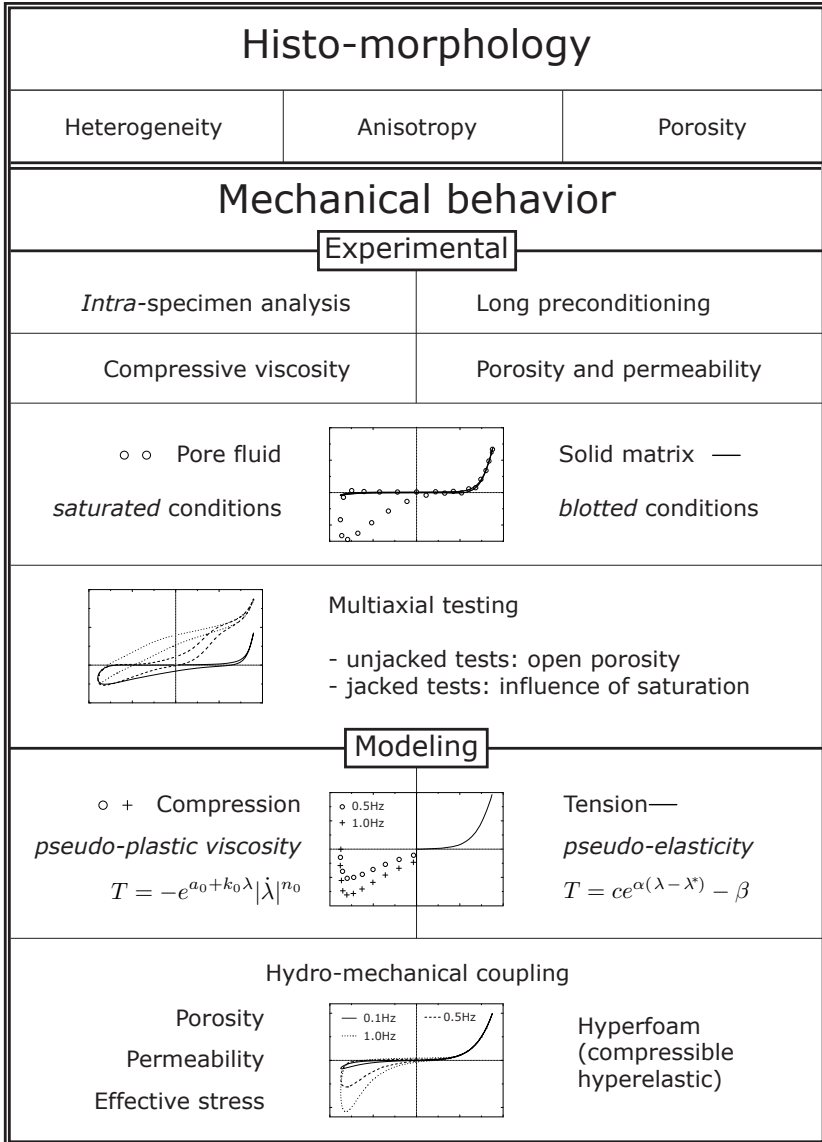
Figure 6.1: Summary of the main results obtained in this work.

approaches.

Experimental (histo-morphological and mechanical)

Still nowadays bone remodeling process remains not well understood. Effort should be addressed to describe in more details this phenomenon, which, among all possible sites in living beings, is highly prolific for dental mobility. This should be done by coupling *in-vivo* and *in-vitro* mechanical testing with biochemical and histo-morphological research.

The periodontal fluid phase pressure generated during physiological occlusion of living subjects should be assessed for a better approach of *in-vivo* conditions in *in-vitro* testing. This could be achieved by lodging a tiny pressure sensor in the (perhaps human) periodontal space via a hole drilled through the dentin wall. Measurements will be then performed only after complete healing of the damaged tissues. In the *in-vitro* testing the fluid pressure could then be monitored using the same technique.

Furthermore, the testing device could be improved by integrating a system allowing for temperature and pH level control. These two parameters, in fact, are known to have an influence on the mechanical behavior of biological tissues.

Numerical modeling

Improvements could be obtained by integrating (i) the material heterogeneity, due to the presence of oriented collagen fibers and (ii) the (non-linear) viscoelastic characteristic presented by the solid matrix of the PDL.

Simulation of the multiaxial loading should then be completed by imposing pertinent boundary constraints to the model.

Appendix A

Microtensile machine

Technical specifications for the MicroTester 5848 from Instron, Massachusets, USA.

Parameter	Specification
Maximum Speed	1500 mm/min
Minimum Speed	0.000024 mm/min
Return Speed	100 mm in 10 seconds
Position Resolution	Position Resolution
	1 micron between 200 and 1500 mm/min
Position Measurement	±0.5 microns over 250 microns travel
Accuracy Under No Load	±2.5 microns over 10 mm travel
	±6.0 microns over 100 mm travel
Actuator Speed Accuracy	±0.1% of set speed
(Zero or Constant Load)	
System Stiffness	8.32 kN/mm
Total Actuator Travel	110 mm
Total Vertical Space	680 mm
Height	Height
Width	452 mm
Depth	440 mm
Width of Base Tray	378 mm
Space Between Columns	190 mm
Weight - Load Frame	89 kg
Drive system	Timing belts & pulleys
Motor	High performance brushless DC servo motor.
	High torque to size and inertia ratios
Rotary Encoder	1000 lines optical incremental rotary
	encoder attached to motor

Appendix B

Pressure pump

Technical specifications for the 200cc/2MPa Advanced Pressure/Volume Controller (ADVDPC) from GDS Instruments Ltd., UK.

Parameter	Specification
Pressure Capacity	2 MPa
Volumetric Capacity	$200cm^3$
Resolution of Measurement and Control	Pressure: <0.1% full range
	Volume: <$0.5mm^3$% full range
Accuracy of measurement	Pressure: <0.1% full range
	Volume: <0.1% full range
Maximal Volume Compensation	$500mm^3$/s
Size	860mm × 230mm × 220mm
Weight	20 kg
Computer Interface	IEEE-488 Standard or
	optional RS232

Appendix C

Submersible load cell

Technical specifications for the Force Transducer Series K 1.0kN from GTM Gassmann Testing and Metrology GmbH, Germany.

Parameter	Specification
Nominal Capacity F	±1 kN
Linearity Error	±0.02%
Hysteresis	±0.02%
Weight	0.6 kg
Nominal Displacement	0.05 mm
Natural Frequency	8 kHz
Bridge impedance	700 Ω
Total Error	1% to 100% of F: ±0.4%
	0.4% to 1% of F: ±0.8%
Influence of Lateral Forces	±0.02% per 0.1F

Appendix D

Jacked tests

Specimens tested with the protocol described on page 93 for the *jacked* test. All the curves showed similar results to what reported in section 4.4.10 for specimen WRdbI.

The only exception was specimen WLdlI (figure D.4), for which the sealing system failed during the testing in *partially saturated* conditions at 0.5MPa.
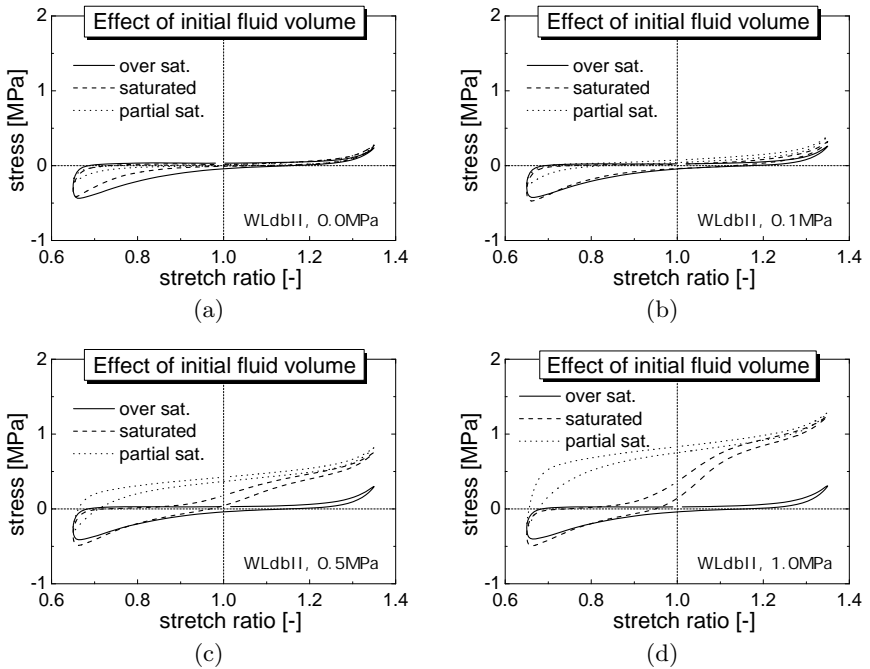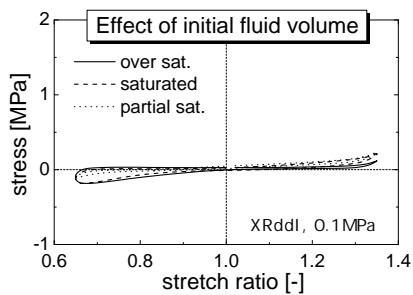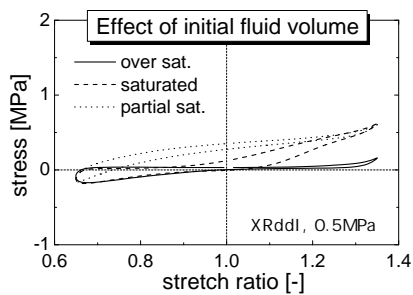
Figure D.1: Effect of saturation on specimen WLdbII: each plot show the curves recorded at a pressure level but for three different level of saturation.
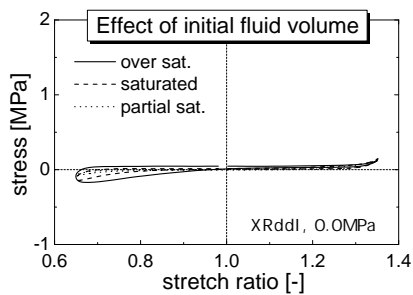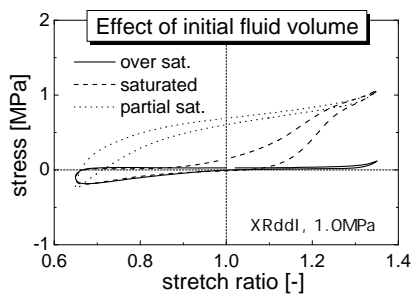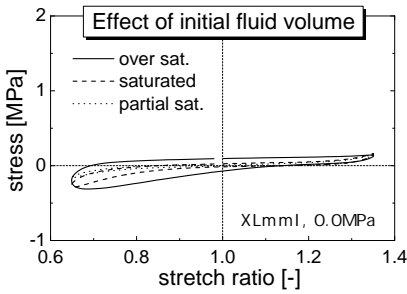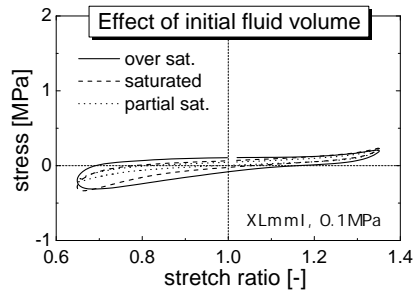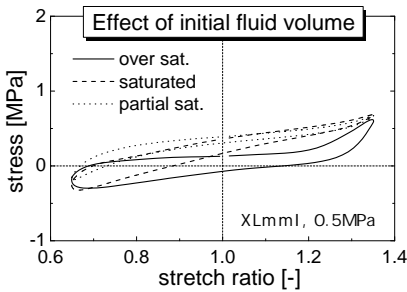
Figure D.2: Effect of saturation on specimen XRddI: each plot show the curves recorded at a pressure level but for three different level of saturation.

Figure D.3: Effect of saturation on specimen XLmmI: each plot show the curves recorded at a pressure level but for three different level of saturation.
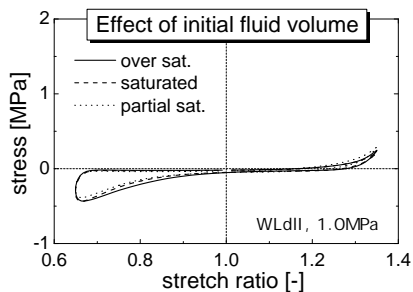
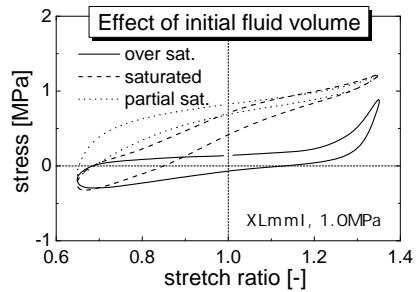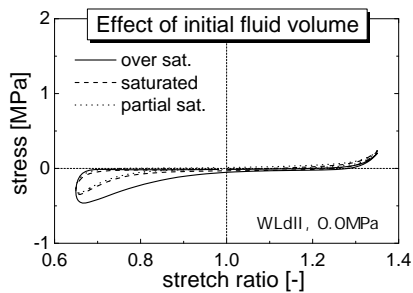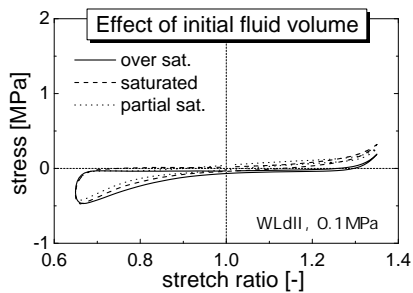Figure D.4: Effect of saturation on specimen WLdlI: each plot show the curves recorded at a pressure level but for three different level of saturation. Notice that the sealing system failed for $p = 0.5$MPa during the testing of the *partial sat.* conditions and for $p = 0.5$MPa (d).
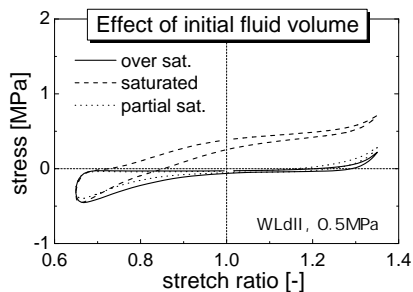
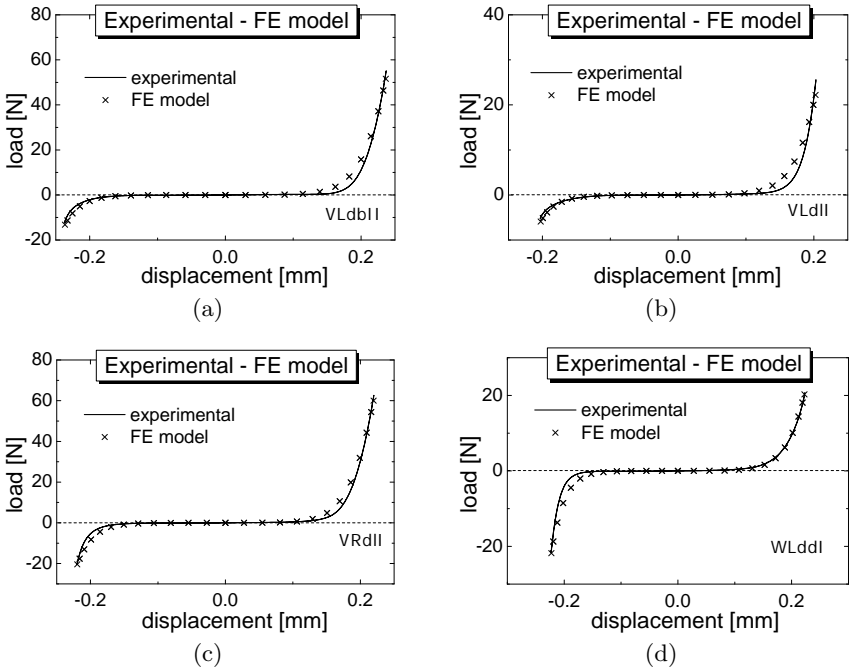# Appendix E
Fitting of the solid matrix responses

Figure E.1: Experimental and numerical curves for the solid matrix response for the specimens of table 5.1.

Bibliography

[1] J. Ainamo. Morphogenetic and functional characteristics of coronal cementum in bovine molars. *Scandinavian Journal of Dental Research*, 78:378–386, 1970.

[2] K. L. Andersen, H. T. Mortensen, E. H. Pedersen, and B. Melsen. Determination of stress levels and profiles in the periodontal ligament by means of an improved three-dimensional finite element model for various types of orthodontic and natural force systems. *Journal of Biomedical Engineering*, 13(4):293–303, 1991.

[3] K. L. Andersen, E. H. Pedersen, and B. Melsen. Material parameters and stress profiles within the periodontal ligament. *American Journal of Orthodontics and Dentofacial Orthopedics*, 99(5):427–440, 1991.

[4] M. Argoubi and A. Shirazi-Adl. Poroelastic creep response analysis of a lumbar motion segment in compression. *Journal of Biomechanics*, 29(10):1331–1339, Oct 1996.

[5] M. M. Ash and S. J. Nelson. *Wheeler's Dental Anatomy, Physiology and Occlusion.* Saunders, 8 edition, 2003.

[6] H. F. Atkinson and W. J. Ralph. In vitro strength of the human periodontal ligament. *Journal of Dental Research*, 56(1):48–52, 1977.

[7] A. Bedford and D.S. Drumheller. Theories of immiscible and structurated mixtures. *International Journal of Engineering Science*, 28(8):863–960, 1983.

[8] W. Beertsen, C. A. G. McCulloch, and J. Sodek. The periodontal ligament: A unique, multifunctional connective tissue. *Periodontology 2000*, 13:20–40, 1997.

203

[9] K. L. Bell, N. Loveridge, J. Power, N. Garrahan, B. F. Meggitt, and J. Reeve. Regional differences in cortical porosity in the fractured femoral neck. *Bone*, 24(1):57–64, 1999.

[10] M. Bergomi, A. Mellal, J. Botsis, T. Shibata, H. W. A. Wiskott, and U. C. Belser. On the mechanical testing of the bovine periodontal ligament. *Computer Methods in Biomechanics and Biomedical Engineering*, 8(4 supp 1):33–34, 2005.

[11] B. K. B. Berkovitz and Shore R. C. Cells of the periodontal ligament. In B.K.B. Berkovitz, B. Moxham, and H. Newman, editors, *The periodontal ligament in health and disease*, chapter 1, pages 9–33. Geoff Greenwood, second edition, 1995.

[12] B. K. B. Berkovitz, R. Whatling, A. W. Barrett, and S. S. Omar. The structure of bovine periodontal ligament with special reference to the epithelial cell rests. *Journal of Periodontology*, 68(9):905–913, Sep 1997.

[13] S. M. Bien. Hydrodynamic damping of tooth movement. *Journal of Dental Research*, 45(3P2):907–914, 1966.

[14] M. A. Biot. Theory of finite deformations of porous solids. *Indiana University Mathematics Journal*, 21(7):597–620, 1972.

[15] R. R. Bird, W. E. Sewart, and E. N. Lightfoot. *Transport phenomena*. John Wiley & Son, 1960.

[16] J. E. Bischoff, E. M. Arruda, and K. Grosh. A rheological network model for the continuum anisotropic and viscoelastic behavior of soft tissue. *Biomechanics and Modeling in Mechanobiology*, 3(1):56–65, Sep 2004.

[17] N. Blaushild, Y. Michaeli, and S. Steigman. Histomorphometric study of the periodontal vasculature of the rat incisor. *Journal of Dental Research*, 71(12):1908–1912, Dec 1992.

[18] F. M. Borodich. Some fractal models of fracture. *Journal of the Mechanics and Physics of Solids*, 45(2):239–259, 1997.

[19] D. D. Bosshardt, M. Bergomi, Vaglio G., and H. W. A. Wiskott. Regional structural characteristics of bovine periodontal ligament samples and their suitability for biomechanical tests. *Journal of Anatomy*, In press.

[20] J. Botsis and M. Deville. *Méchanique des milieux continus: une introduction*. Presses polytechniques et universitaires romandes, 2006.

[21] R. Bowen. Compressible porous media models by use of the theory of mixtures. *International Journal of Engineering Science*, 20(6):697–753, 1982.

[22] S. L. Butler, S. S. Kohles, R. J. Thielke, C. Chen, and R. Vanderby. Interstitial fluid flow in tendons or ligaments: a porous medium finite element simulation. *Medical and Biological Engineering and Computing*, 35(6):742–746, Nov 1997.

204

[23] W. D. Carrier. Goodbye, Hazen; hello, Kozeny-Carmanazen. Technical report, ASCE, 2003.

[24] M. Chiba and K. Komatsu. In vitro estimation of the resisting force of tooth eruption and the zone of shear in the rat incisor periodontal ligament. In Z. Davidovitch, editor, *The biological mechanisms of tooth eruption and root resorption*, pages 193–205. EBSCO Media, Birmingham, 1988.

[25] M. Chiba and K. Komatsu. Mechanical responses of the periodontal ligament in the transverse section of the rat mandibular incisor at various velocities of loading in vitro. *Journal of Biomechanics*, 26(4-5):561–570, 1993.

[26] M. Chiba and S. Ohkawa. Measurement of the tensile strength of the periodontium in the rat mandibular first molar. *Archives of Oral Biology*, 25(8-9):569–572, 1980.

[27] M. Chiba, A. Yamane, S. Ohshima, and K. Komatsu. In vitro measurement of regional differences in the mechanical properties of the periodontal ligament in the rat mandibular incisor. *Archives of Oral Biology*, 35(2):153–161, 1990.

[28] M. Cho and P.R. Garant. Radioautographic study of [^{3}h]mannose utilization during cementoblast differentiation, formation of acellular cementuum, and development of periodontal ligament principal fibers. *The Anatomical Record*, 223(2):209–222, 1989.

[29] S. D. Cook, A. M. Weinstein, and J. J. Klawitter. A 3-dimensional finite-element analysis of a porous rooted co-cr-mo alloy dental implant. *Journal of Dental Research*, 61(1):25–29, 1982.

[30] S. D. Coolidge. The thickness of the human periodontal ligament. *Journal of American Dental Association*, 24:1260–1265, 1937.

[31] S. C. Cowin. Bone poroelasticity. *Journal of Biomechanics*, 32(3):217–238, 1999.

[32] S. C. Cowing and S. B. Doty. *Tissue Mechanics*. Springer-Verlag, 2007.

[33] C. H. Daly, J. I. Nicholls, W. L. Kydd, and P. D. Nansen. The response of the human periodontal ligament to torsional loading–i. experimental methods. *Journal of Biomechanics*, 7(6):517–522, 1974.

[34] H. Dan and K. Kohyama. Interactive relationship between the mechanical properties of food and the human response during the first bite. *Archives of Oral Biology*, 52(5):455–464, 2007.

[35] Z. Davidovitch. Tooth movement. *Critical Reviews in Oral Biology & Medicine*, 2(4):411–450, 1991.

[36] R. de Boer. *Theory of Porous Media*. Springer, 2000.

[37] W. F. Decraemer, M. A. Maes, V. J. Vanhuyse, and P. Vanpeperstraete. A non-linear viscoelastic constitutive equation for soft biological tissues, based upon a structural model. *Journal of Biomechanics*, 13(7):559–564, 1980.

[38] C. Dorow, N. Krstin, and F. G. Sander. In vivo experimental investigation of tooth mobility in humans. *Biomedizinische Technik*, 47(1-2):20–25, Jan-Feb 2002.

[39] C. Dorow and F. Sander. Development of a model for the simulation of orthodontic load on lower first premolars using the finite element method. *Journal of Orofacial Orthopedics*, 66(3):208–218, 2005.

[40] M. Durkee. Periodontal ligament stress patterns in a nonlinear finite element model. *Journal of Dental Research*, 76:1473–1473, 1997.

[41] M. Durkee, E. D. Rekow, and V. P. Thompson. Pdl stress patterns in a 3d nonlinear finite element model. *Journal of Dental Research*, 77:277–277, 1998.

[42] M. C. Durkee. *The non-linear stress-strain behavior of the human periodontal ligament and its effect on finite element models of dental structures.* PhD thesis, University of Maryland, 1996.

[43] M. L. Dyment and J. L. Synge. The elasticity of the periodontal membrane. *Oral Health*, 25:105–109, 1935.

[44] L. G. A. Edwall and H. Aars. The physiology of the vasculature of the periodontal ligament. In B. K. B. Berkovitz, B. Moxham, and H. Newman, editors, *The periodontal ligament in health and disease*, chapter 6, pages 121–131. Geoff Greenwood, second edition, 1995.

[45] W. Ehlers and B. Markert. A linear viscoelastic biphasic model for soft tissues based on the theory of porous media. *Journal of Biomechanical Engineering - Transactions of the ASME*, 123(5):418–424, Oct 2001.

[46] V. F. Ferrario, C. Sforza, G. Zanotti, and G. M. Tartaglia. Maximal bite forces in healthy young adults as predicted by surface electromyography. *Journal of Dentistry*, 32(6):451–457, 2004.

[47] P. Fillunger. Der auftrieb von talsperren, teil i-iii. *Österr. Wochenschrift für den öffentlichen Baudienst*, pages 532–570, 1913.

[48] S. R. Freezer and M. R. Sims. A transmission electron-microscope stereological study of the blood vessels, oxytalan fibres and nerves of mouse-molar periodontal ligament. *Archives of Oral Biology*, 32(6):407–412, 1987.

[49] Y. C. Fung. Elasticity of soft tissues in simple elongation. *American Journal of Physiology*, 213(6):1532–1544, 1967.

[50] Y. C. Fung. *Biomechanics: Mechanical Properties of Living Tissue.* Springer, 1993.

[51] L. Gartner. *Oral hystology and embrioogy*. Jen House, 1989.

[52] I. Glickmam and J. B. Smulow. Buttressing bone formation in the periodontium. *Journal of Periodontology*, 36:365–370, 1965.

[53] V. K. Goel, S. C. Khera, S. Gurusami, and R. C. S. Chen. Eeefct of cavity depth on stresses in a restored tooth. *Journal of Prosthetic Dentistry*, 67(2):174–183, Feb 1992.

[54] J. N. Grima, R. Gatt, N. Ravirala, A. Alderson, and K. E. Evans. Negative poisson's ratios in cellular foam materials. *Materials Science and Engineering A*, 423(1-2):214–218, 2006.

[55] Habbit, Karlson, and Sorensen. *ABAQUS version 6.7 – Documentation*.

[56] R. Hill. Aspects of invariance in solid mechanics. *Advances in Applied Mechanics*, 18:1–75, 1978.

[57] S. P. Ho, S. J. Marshall, M. I. Ryder, and G. W. Marshall. The tooth attachment mechanism defined by structure, chemical composition and mechanical properties of collagen fibers in the periodontium. *Biomaterials*, 28(35):5238–5245, 2007.

[58] V. V. E. Hohlt and W. E. Roberts. Rigid implants for orthodontic anchorage. In Z. Davidovitch, editor, *Biological mechanisms of tooth eruption, resorption and replacement by implants*, pages 661–666. Birmingham: EBSCO Media, 1994.

[59] M. H. Holmes. Finite deformation of soft tissue: analysis of a mixture model in uniaxial compression. *Journal of Biomechanical Engineering - Transactions of the ASME*, 108(4):372–381, Nov 1986.

[60] G. A. Holzapfel and T. C. Gasser. A viscoelastic model for fiber-reinforced composites at finite strains: Continuum basis, computational aspects and applications. *Computer Methods in Applied Mechanics and Engineering*, 190(34):4379–4403, 2001.

[61] G. A. Holzapfel, T. C. Gasser, and R. W. Ogden. A new constitutive framework for arterial wall mechanics and a comparative study of material models. *Journal of Elasticity*, 61(1-3):1–48, 2000.

[62] J. D. Humphrey and S. Delange. *An introduction to biomechanics: solid and fluids, analysis and design*. Springer-Verlag, 2004.

[63] M. L. Jones, J. Hickman, J. Middleton, J. Knox, and C. Volp. A validated finite element method study of orthodontic tooth movement in the human subject. *Journal of Orthodontics*, 28:29–38, 2001.

[64] N. D. Jones and L. E. StClair. The cheek teeth of cattle. *American Journal of Veterinary Research*, 18(68):536–542, 1957.

[65] J. Justiz. *With application to the periodontal ligament: a nonlinear large strain viscoelastic law.* PhD thesis, Ecole Polytechnique de Lausanne - EPFL, 2004.

[66] J. Kappraff. The geometry of coastlines - a study in fractals. *Computers and Mathematics with Applications-Part B*, 12(3-4):655–671, May-Aug 1986.

[67] A. Kawarizadeh, C. Bourauel, and A. Jager. Experimental and numerical determination of initial tooth mobility and material properties of the periodontal ligament in rat molar specimens. *European Journal of Orthodontics*, 25(6):569–578, Dec 2003.

[68] R. G. Keanini, R. D. Roer, and R. M. Dillaman. A theoretical model of circulatory interstitial fluid flow and species transport within porous cortical bone. *Journal of Biomechanics*, 28(8):901–914, 1995.

[69] D. E. Kenyon. A mathematical model of water flux through aortic tissue. *Bulletin of Mathematical Biology*, 41(1):79–90, 1979.

[70] A. Kishen. Periapical biomechanics and the role of cyclic biting force in apical retrograde fluid movement. *International Endodontic Journal*, 38(9):597–603, Sep 2005.

[71] K. Komatsu. In vitro mechanics of the periodontal ligament in impeded and unimpeded rat mandibular incisors. *Archives of Oral Biology*, 33(11):783–791, 1988.

[72] K. Komatsu and M. Chiba. The effect of velocity of loading on the biomechanical responses of the periodontal ligament in transverse sections of the rat molar in vitro. *Archives of Oral Biology*, 38(5):369–375, 1993.

[73] K. Komatsu, M. Kanazashi, A. Shimada, T. Shibata, A. Viidik, and M. Chiba. Effects of age on the stress-strain and stress-relaxation properties of the rat molar periodontal ligament. *Archives of Oral Biology*, 49(10):817–824, Oct 2004.

[74] K. Komatsu, T. Shibata, and A. Shimada. Analysis of contribution of collagen fibre component in viscoelastic behaviour of periodontal ligament using enzyme probe. *Journal of Biomechanics*, 40(12):2700–2706, 2007.

[75] K. Komatsu and A. Viidik. Changes in the fibre arrangement of the rat incisor periodontal ligament in relation to various loading levels in vitro. *Archives of Oral Biology*, 41(2):147–159, 1996.

[76] N. Krstin, C. Dorow, R. P. Franke, and F. G. Sander. Experiments to determine time-dependent material properties of the periodontal ligament. *Biomedizinische Technik*, 47(7-8):202–208, Jul-Aug 2002.

[77] M. Kuroiwa, T. Kodaka, and S. Higashi. Scanning electron microscopic observations of the periodontal ligament fibers and cells in rat molar teeth. *Kaibogaku zasshi. Journal of anatomy*, 67(3):200–206, 1992.

[78] L. Laloui. Mechanics of porous media. Presses polytechniques et universitaires romandes, 2006.

[79] C. Li, R. I. Borja, and R. A. Regueiro. Dynamics of porous media at finite strain. *Computer Methods in Applied Mechanics and Engineering*, 193(36-38):3837–3870, 2004.

[80] M. A. K. Liebschner and T. S. Keller. Hydraulic strengthening affects the stiffness and strength of cortical bone. *Annals of Biomedical Engineering*, 33(1):26–38, 2005.

[81] G. Macchiarelli, O. Ohtani, S. A. Nottola, T. Stallone, A. Camboni, I. M. Prado, and P. M. Motta. A micro-anatomical model of the distribution of myocardial endomysial collagen. *Histology and Histopathology*, 17(3):699–706, 2002.

[82] U. Mandel, P. Dalgaard, and A. Viidik. A biomechanical study of the human periodontal ligament. *Journal of Biomechanics*, 19(8):637–639, 1986.

[83] J. M. Mansour and V. C. Mow. Permeability of articular cartilage under compressive strain and at high pressures. *Journal of Bone and Joint Surgery - American Volume*, 58(4):509–516, 1976.

[84] J. E. Marsden and T. J. R. Hughes. *Mathematical foundations of elasticity*. Prentice-Hall, 1893.

[85] M. Matsuo and K. Takahashi. Scanning electron microscopic observation of microvasculature in periodontium. *Microscopy Research and Technique*, 56(1):3–14, Jan 2002.

[86] J. Middleton, M. Jones, and A. Wilson. The role of the periodontal ligament in bone modeling: The initial development of a time-dependent finite element model. *American Journal of Orthodontics and Dentofacial Orthopedics*, 109(2):155–162, 1996.

[87] N. J. Mills and A. Gilchrist. Properties of bonded-polypropylene-bead foams: Data and modelling. *Journal of Materials Science*, 42(9):3177–3189, 2007.

[88] V. C. Mow, S. C. Kuei, W. M. Lai, and C. G. Armstrong. Biphasic creep and stress-relaxation of articular-cartilage in compression - theory and experiments. *Journal of Biomechanical Engineering - Transactions of the ASME*, 102(1):73–84, 1980.

[89] H. R. Muhlemann. Tooth mobiliy - a review of clinical aspects and research findings. *Journal of Periodontology*, 38(6P2):686–713, 1967.

[90] P. Muir, S. J. Sample, J. G. Barrett, J. McCarthy, R. Vanderby, Jr., M. D. Markel, L. J. Prokuski, and V. L. Kalscheur. Effect of fatigue loading and associated matrix microdamage on bone blood flow and interstitial fluid flow. *Bone*, 40(4):948–956, 2007.

[91] A. N. Natali, E. L. Carniel, P. G. Pavan, C. Bourauel, A. Ziegler, and L. Keilig. Experimental-numerical analysis of minipig's multi-rooted teeth. *Journal of Biomechanics*, 40(8):1701–1708, 2007.

[92] A. N. Natali, P. G. Pavan, E. L. Carniel, and C. Dorow. Viscoelastic response of the periodontal ligament: An experimental-numerical analysis. *Connective Tissue Research*, 45(4-5):222–230, 2004.

[93] A. N. Natali, P. G. Pavan, and C. Scarpa. Numerical analysis of tooth mobility: formulation of a non-linear constitutive law for the periodontal ligament. *Dental Materials*, 20(7):623–629, Sep 2004.

[94] A. N. Natali, P. G. Pavan, B. A. Schrefler, and S. Secchi. A multi-phase media formulation for biomechanical analysis of periodontal ligament. *Meccanica*, 37(4-5):407–418, 2002.

[95] C. Negus and T. Impelluso. Continuum remodeling revisited. *Biomechanics and Modeling in Mechanobiology*, 6(4):211–226, 2007.

[96] R. W. Ogden. Large deformations isotropic elasticity - on the correlation of theory and experiment for incompressible rubberlike solids. *Proceedings of the Royal Society of London, Series A*, 326:565–584, 1972.

[97] R. W. Ogden. Nonlinear elasticity with application to material modelling. Centre of Excellence for Advanced Materials and Structures, Warsaw, 2003.

[98] K. G. Palcanis. Effect of occlusal trauma on interstitial pressure in periodontal ligament. *Journal of Dental Research*, 52(5):903–910, 1973.

[99] G. Parfitt. Measurement of the physiological mobility of individual teeth in an axial direction. *Journal of Dental Research*, 39(3):608–618, 1960.

[100] D. H. Pashley and R. M. Carvalho. Dentine permeability and dentine adhesion. *Journal of Dentistry*, 25(5):355–372, Sep 1997.

[101] D. C. A. Picton. The effect on vertical tooth mobility of extraction and immediate replacement of incisors (macaca fascicularis). *Archives of Oral Biology*, 36(1):85–87, 1991.

[102] D. C. A. Picton and D. J. Wills. Viscoelastic properties of the periodontal ligament and mucous membrane. *The Journal of Prosthetic Dentistry*, 40(3):263–272, 1978.

[103] G. Pietrzak, A. Currnier, J. Botsis, S. Scherrer, A. Wiskott, and U. Belser. A nonlinear elastic model of the periodontal ligament and its numerical calibration for the study of tooth mobility. *Computer Methods in Biomechanics and Biomedical Engineering*, 5(2):91–100, 2002.

[104] M. Pini. *Mechanical characterization and modeling of the periodontal ligament.* PhD thesis, Università degli studi di Trento, Italy, 1999.

[105] M. Pini, H. W. A. Wiskott, S. S. Scherrer, J. Botsis, and U. C. Belser. Mechanical characterization of bovine periodontal ligament. *Journal of Periodontal Research*, 37(4):237–244, Aug 2002.

[106] M. Pini, P. Zysset, J. Botsis, and R. Contro. Tensile and compressive behaviour of the bovine periodontal ligament. *Journal of Biomechanics*, 37(1):111–119, Jan 2004.

[107] J. G. Pinto and Y. C. Fung. Mechanical properties of the heart muscle in the passive state. *Journal of Biomechanics*, 6(6):597–616, 1973.

[108] D. P. Pioletti. *Viscoelastic properties of soft tissues: application to knee ligaments and tendons.* PhD thesis, Ecole Polytechnique de Lausanne - EPFL, 1997.

[109] D. P. Pioletti and L. R. Rakotomanana. Non-linear viscoelastic laws for soft biological tissues. *European Journal of Mechanics - A/Solids*, 19(5):749–759, 2000.

[110] D. P. Pioletti, L. R. Rakotomanana, J. F. Benvenuti, and P. F. Leyvraz. Viscoelastic constitutive law in large deformations: application to human knee ligaments and tendons. *Journal of Biomechanics*, 31(8):753–757, 1998.

[111] G. Polya. *How to solve it.* Princeton UP, Princeton, 1945.

[112] M. Poppe, C. Bourauel, and A. Jäger. Determination of the elasticity parameters of the human periodontal ligament and the location of the center of resistance of single-rooted teeth. *Journal of Orofacial Orthopedics*, 63:358–370, 2002.

[113] C. G. Provatidis. A comparative fem-study of tooth mobility using isotropic and anisotropic models of the periodontal ligament. *Medical Engineering and Physics*, 22(5):359–370, Jun 2000.

[114] H. Qian, J. Chen, and T. R. Katona. The influence of pdl principal fibers in a 3-dimensional analysis of orthodontic tooth movement. *American Journal of Orthodontics and Dentofacial Orthopedics*, 120(3):272–279, 2001.

[115] Q.-H. Qin and M. V. Swain. A micro-mechanics model of dentin mechanical properties. *Biomaterials*, 25(20):5081–5090, 2004.

[116] A. Quirinia and A. Viidik. Freezing for postmortal storage influences the biomechanical properties of linear skin wounds. *Journal of Biomechanics*, 24(9):819–823, 1991.

[117] W. J. Ralph. The in vitro rupture of human periodontal ligament. *Journal of Biomechanics*, 13(4):369–373, 1980.

[118] W. J. Ralph. Tensile behaviour of the periodontal ligament. *Journal of Periodontal Research*, 17(4):423–426, 1982.

[119] S. P. Ramfjord and M. M. Ash. *Periodontology and Periodontics*. W.B. Saunders Company, 1979.

[120] J. S. Rees and P. H. Jacobsen. Elastic modulus of the periodontal ligament. *Biomaterials*, 18(14):995–999, Jul 1997.

[121] J. M. Reina, J. M. Garcia-Aznar, J. Dominguez, and M. Doblare. Numerical estimation of bone density and elastic constants distribution in a human mandible. *Journal of Biomechanics*, 40(4):828–836, 2007.

[122] M. H. Ross, G. I. Kaye, and W. Pawlina. *Histology: a text and atlas*. Lippincott Williams & Wilkins, Philadelphia, Pa., 2007.

[123] C. S. Sanctuary. *Experimental investigation of the bovine periodontal ligament*. PhD thesis, Ecole Polytechnique de Lausanne - EPFL, 2003.

[124] C. S. Sanctuary, H. W. A. Wiskott, J. Botsis, S. S. Scherrer, and U. C. Belser. Oscillatory shear loading of bovine periodontal ligament - a methodological study. *Journal of Biomechanical Engineering - Transactions of the ASME*, 128(3):443–448, Jun 2006.

[125] C. S. Sanctuary, H. W. A. Wiskott, J. Justiz, J. Botsis, and U. C. Belser. In vitro time-dependent response of periodontal ligament to mechanical loading. *Journal of Applied Physiology*, 99(6):2369–2378, Dec 2005.

[126] Y. Sato, M. Nishihira, H. Ishikawa, E. Honmura, J. Irie, S. Nakamura, K. Yamamoto, M. Wakita, and H. Morikawa. The relationships between tissue response and stress distribution in the periodontal ligament during orthodontic tooth movement. In *11th conference of the ESB*, July 1998.

[127] R. Schilke. Comparison of the number and diameter of dentinal tubules in human and bovine dentine by scanning electron microscopic investigation. *Archives of Oral Biology*, 45:355–361, 2000.

[128] H. E. Schroeder. *The periodontium*. Springer-Verlag, 1986.

[129] N. J. Selliseth and K. A. Selvig. The vasculature of the periodontal ligament - a scanning electron-microscopic study using corrosion casts in the rat. *Journal of Periodontology*, 65(11):1079–1087, Nov 1994.

[130] T. Shibata, J. Botsis, M. Bergomi, A. Mellal, and K. Komatsu. Mechanical behavior of bovine periodontal ligament under tension-compression cyclic displacements. *European Journal of Oral Sciences*, 114(1):74–82, 2006.

[131] P. Silva, S. Crozier, M. Veidt, and M. J. Pearcy. An experimental and finite element poroelastic creep response analysis of an intervertebral hydrogel disc model in axial compression. *Journal of Materials Science-Materials in Medicine*, 16(7):663–669, Jul 2005.

[132] M. R. Sims, P. I. Leppard, W. J. Sampson, and C. W. Dreyer. Microvascular luminal volume changes in aged mouse periodontal ligament. *Journal of Dental Research*, 75(7):1503–1511, Jul 1996.

[133] A. W. Skempton. Terzaghi's discovery of effective stress. In *From Theory to Practice in Soil Mechanics*, pages 42–53. Terzaghi, K., 1960.

[134] P. Sloan and Carter D. H. Structural organization of the fibers of the periodontal ligament. In B.K.B. Berkovitz, B. Moxham, and H. Newman, editors, *The periodontal ligament in health and disease*, chapter 2, pages 35–53. Geoff Greenwood, second edition, 1995.

[135] B. Storakers. On material representation and constitutive branching in finite compressive elasticity. *Journal of Mechanicsand Physics of Solids*, 34(2):125–145, 1986.

[136] D. D. Stromberg and C. A. Wiederhi. Viscoelastic description of a collagenous tissue in simple elongation. *Journal of Applied Physiology*, 26(6):857–862, 1969.

[137] J. L. Synge. The equilibrium of a tooth with a g neral conical root. *Philosophical Magazine*, 15(101):969–996, May 1933.

[138] J. L. Synge. The tightness of the teeth, considered as a problem concerning the equilibrium of a thin incompressible elastic membrane. *Philosophical Transactions of the Royal Society of London Series A - Containing papers of a mathematical or physical character*, 231:435–477, Mar 1933.

[139] A. E. Tami, P. Nasser, O. Verborgt, M. B. Schaffler, and M. L. Knothe Tate. The role of interstitial fluid flow in the remodeling response to fatigue loading. *Journal of Bone and Mineral Research*, 17(11):2030–2037, 2002.

[140] E. Tanaka, T. Inubushi, K. Takahashi, M. Shirakura, R. Sano, D. A. Dalla-Bona, A. Nakajima, T. M. G. J. van Eijden, and K. Tanne. Dynamic shear properties of the porcine molar periodontal ligament. *Journal of Biomechanics*, 40(7):1477–1483, 2007.

[141] T. T. Tanaka and Y. C. Fung. Elastic and inelastic properties of the canine aorta and their variation along the aortic tree. *Journal of Biomechanics*, 7(4):357–370, 1974.

[142] K. Tanne, T. Nagataki, Y. Inoue, M. Sakuda, and C. J. Burstone. Patterns of initial tooth displacements associated with vorious root lengths and alveolar bone heights. *American Journal of Orthodontics and Dentofacial Orthopedics*, 100(1):66–71, Jul 1991.

[143] K. Tanne, S. Yoshida, T. Kawata, A. Sasaki, J. Knox, and M. L. Jones. An evaluation of the biomechanical response of the tooth and periodontium to orthodontic forces in adolescent and adult subjects. *Journal of Orthodontics*, 25(2):109–115, 1998.

[144] S. R. Toms, G. J. Dakin, J. E. Lemons, and A. W. Eberhardt. Quasi-linear viscoelastic behavior of the human periodontal ligament. *Journal of Biomechanics*, 35(10):1411–1415, Oct 2002.

[145] S. R. Toms and A. W. Eberhardt. A nonlinear finite element analysis of the periodontal ligament under orthodontic tooth loading. *American Journal of Orthodontics and Dentofacial Orthopedics*, 123(6):657–665, Jun 2003.

[146] S. R. Toms, J. E. Lemons, A. A. Bartolucci, and A. W. Eberhardt. Nonlinear stress-strain behavior of periodontal ligament under orthodontic loading. *American Journal of Orthodontics and Dentofacial Orthopedics*, 122(2):174–179, Aug 2002.

[147] G. Vaglio. *Analyse histo-morphométrique des vaisseaux sanguins du ligament paradontal bovin*. PhD thesis, Université de Genève, 2008.

[148] W. D. van Driel, E. J. van Leeuwen, J. W. Von den Hoff, J. C. Maltha, and A. M. Kuijpers-Jagtman. Time-dependent mechanical behaviour of the periodontal ligament. *Proceedings of the Institution of Mechanical Engineers Part H-Journal of Engineering in Medicine*, 214(H5):497–504, 2000.

[149] C. Verna, B. Melsen, and F. Melsen. Differences in static cortical bone remodeling parameters in human mandible and iliac crest. *Bone*, 25(5):577–583, 1999.

[150] D. R. Veronda and R. A. Westmann. Mechanical characterization of skin-finite deformations. *Journal of Biomechanics*, 3(1):111–124, 1970.

[151] D. Vollmer, C. Bourauel, K. Maier, and A. Jager. Determination of the centre of resistance in an upper human canine and idealized tooth model. *European Journal of Orthodontics*, 21(6):633–648, Dec 1999.

[152] K. von Terzaghi. Die berechnung der durchassigkeitsziffer des tones aus dem verlauf der hydrodynamishen spannungerscheinungen. *Sitzungbericht Akademie Wissenschaft Wien, Mathematik Naturwissenschafts*, 132:125–138, 1923.

[153] N. J. Wachter, P. Augat, G. D. Krischak, M. Mentzel, L. Kinzl, and L. Claes. Prediction of cortical bone porosity in vitro by microcomputed tomography. *Calcified Tissue International*, 68:38–42, 2001.

[154] N. Wagle, N. N. Do, J. Yu, and J. L. Borke. Fractal analysis of the pdl-bone interface and implications for orthodontic tooth movement. *American Journal of Orthodontics and Dentofacial Orthopedics*, 127(6):655–661, 2005.

[155] B. W. Weinberger. *Orthodontics, an historcal review of its origin and evolution*, page 138. C. V. Mosby, St. Louis, 1926.

[156] J. R. Williams, R. N. Natarajan, and G. B. J. Andersson. Inclusion of regional poroelastic material properties better predicts biomechanical behavior of lumbar discs subjected to dynamic loading. *Journal of Biomechanics*, 40(9):1981–1987, 2007.

[157] K. R. Williams and J. T. Edmundson. Orthodontic tooth movement analysed by the finite element method. *Biomaterials*, 5(6):347–351, 1984.

[158] W. N. Williams, A. C. Levin, L. L. LaPointe, and C. E. Cornell. Bite force discrimination by individuals with complete dentures. *The Journal of Prosthetic Dentistry*, 54(1):146–150, 1985.

[159] D. J. Wills, D. C. A. Picton, and W. I. R. Davies. Investigation of viscoelastic properties of periodontium in monkeys. *Journal of Periodontal Research*, 7(1):42–51, 1972.

[160] D. J. Wills, D. C. A. Picton, and W. I. R. Davies. A study of the fluid systems of the periodontium in macaque monkeys. *Archives of Oral Biology*, 21(3):175–185, 1976.

[161] D. J. Wills, D. C. A. Picton, and W. I. R. Davies. The intrusion of the tooth for different loading rates. *Journal of Biomechanics*, 11(10-12):429–434, 1978.

[162] J. Wolff. *Das Gesetz der Transformation der Knochen*. August Hirschwald, Berlin, 1892.

[163] D. G. Wright and D. C. Rennels. A study of the elastic properties of plantar fascia. *Journal of Bone and Joint Surgery*, 46(A):482–492, 1964.

[164] A. Yamane, S. Ohshima, K. Komatsu, and M. Chiba. Mechanical properties of the periodontal ligament in the incisor teeth of rats from 6 to 24 months of age. *Gerodontology*, 9(1):17–23, 1990.

[165] M. Yang and L. A. Taber. The possible role of poroelasticity in the apparent viscoelastic behavior of passive cardiac-muscle. *Journal of Biomechanics*, 24(7):587–597, 1991.

[166] B. G. Yew, E. C. Drumm, and G. Guiochon. Mechanics of column beds: I. acquisition of the relevant parameters. *AICHE Journal*, 49(3):626–641, Mar 2003.

[167] F. C. P. Yin and Y. C. Fung. Mechanical properties of isolated mammalian ureteral segments. *American Journal of Physiology*, 221(5):1484–1493, 1971.

[168] N. Yoshida, Y. Koga, C. L. Peng, E. Tanaka, and K. Kobayashi. In vivo measurement of the elastic modulus of the human periodontal ligament. *Medical Engineering and Physics*, 23(8):567–572, Oct 2001.

[169] Y. Zhang, D. H. Pashley, and E. L. Pashley. The effects of pain-free desensitizer on dentine permeability and tubule occlusion overtime, in vitro. *Journal of Clinical Periodontology*, 25:884–891, 1998.

[170] A. I. Zhurov, G. Limbert, D. P. Aeschlimann, and J. Middleton. A constitutive model for the periodontal ligament as a compressible transversely isotropic visco-hyperelastic tissue. *Computer Methods in Biomechanics and Biomedical Engineering*, 10(3):223–235, 2007.

[171] A. Ziegler, L. Keilig, A. Kawarizadeh, A. Jager, and C. Bourauel. Numerical simulation of the biomechanical behaviour of multi-rooted teeth. *European Journal of Orthodontics*, 27(4):333–339, Aug 2005.

216

Curriculum Vitæ

Marzio Bergomi

Personal Information:

Date of birth:	21st November 1977.
Place of birth:	Mendrisio, Switzerland.

Education:

2003-2007:	PhD student at LMAF (Laboratoire de mécanique appliquée et d'analyse de fiabilité) at EPFL.
2002:	MS in micro-engineering with a specialization in applied optics.
1996-2002:	Student in micro-engineering at Ecole Polytechnique Fédérale de Lausanne.

Teaching Experience:

2005-2007:	Assistant for the course "Mechanics of Structures", Prof. I. Botsis, LMAF/EPFL.
2006-2007:	Assistant for the course "Continuum Mechanics", Prof. I. Botsis, LMAF/EPFL.

Publications: see [10, 19, 130]